A density-functional-theory investigation of Cu_5 atomic quantum clusters deposited on TiO_2 and Cu substrates as catalysts for green energy

Fatimah Alhawiti (Postgraduate Researcher)

This dissertation is submitted for the degree of Doctor of Philosophy

2024

Department of Physics, Lancaster University, UK

Declaration

This thesis has not been submitted in support of an application for another degree at this or any other university. It is the result of my work and includes nothing that is the outcome of work done in collaboration except where specifically indicated. Many of the ideas in this thesis were the product of discussion with my supervisor Prof. Colin Lambert and my co-supervisor, Dr. Qingqing Wu.

Fatimah Alhawiti

2024

Abstract

Environmental concerns are exacerbated by the fact that conventional fossil fuel combustion is still a significant source of atmospheric CO_2. Several strategies are being investigated to counter this. The first promising avenue is an environmentally friendly way to produce hydrogen by splitting water with solar energy. Hydrogen (H_2) has emerged as a clean, renewable, and energy-efficient energy vector. However, the majority of hydrogen gas comes from fossil fuels through processes like steam reforming or coal gasification. There is a pressing need for environmentally friendly methods, particularly novel inorganic photocatalysts, to produce green hydrogen through renewable means by splitting water using sunlight. Another important way to reduce emissions and produce useful materials is to reduce CO_2 levels in order to produce valuable carbon-based chemicals. Based on density-functional theory (DFT), using the Vienna ab initio simulation package (VASP), I employed the generalized gradient approximation (GGA) and a hybrid functional combined with Hartree Fock (HF) theory to systematically study their geometric and electronic structures. The first focus of this thesis is to enhance the photocatalytic properties of perfect and defective rutile TiO_2 by doping with Cu_5 atomic quantum clusters (AQCs). Furthermore, the influence of silicate (SiO_3^{2-}), which is added experimentally during the purification of the AQCs, on the electronic structures of titania is examined. I found that the creation of a single polaron at either a five-fold coordinated (Ti5c) or a six-fold coordinated (Ti6c) atoms, indicating increased surface activity, is caused by the Cu AQCs donating electrons to both perfect and decreased TiO_2 surfaces. I also discovered that the gap states of Cu_5/TiO_2 are unaffected by the presence of SiO_3^{2-}.

In the second part, I investigate the CO_2 reduction reaction (CO_2RR) using electrocatalysts based on (Cu) electrodes. According to a suggested energy diagram, adding Cu_5 dramatically reduces the energy barriers needed to form important intermediates, improving the selectivity of the process for producing carbon monoxide (CO) and formic acid (HCOOH). For this reason, Cu_5 is recommended as a surface modification that can be used to optimize catalytic performance in CO_2 reduction on Cu surfaces. This provides a workable approach to defect engineering, which can optimize catalyst efficiency.

Acknowledgments

I want to thank my supervisor, Professor Colin J. Lambert, for continuously prioritizing his students' well-being and interests. The unparalleled generosity, patience, and steadfast support he has shown me are beyond words. Working with such an excellent physicist and kind individual has been an enormous honor, and I am grateful for the opportunity. I want to convey my sincere appreciation to Dr. Qingqing Wu, whose insightful comments, dedicated time, and valuable suggestions have played an indispensable role in the successful completion of this work. Without her guidance and support, these achievements would not have been possible. Furthermore, I extend my gratitude to all the co-supervisors in our group, including Dr. Ali, Dr. Iain, and Dr. Songjun. Each of them has contributed significantly to my learning experience, leaving a positive impact throughout my studies. I would also like to express my appreciation to my friends and colleagues within Colin's group. Additionally, I extend my thanks to the Ministry of Higher Education in Saudi Arabia and Taif University for the support I received during my PhD journey.

I extend my heartfelt thanks to my late father, whose support and wisdom continue to inspire me. My gratitude also goes to my dear mother for her love and encouragement. A special acknowledgment to my husband Mahmoud, whose belief in me has been the cornerstone of my academic journey. To my children (Hour, Abdulrahman, Mohammed, and Noor), I appreciate your understanding and patience during this process. A warm thank you to my sister Zainab, whose unwavering support and camaraderie have added a unique and cherished dimension to this journey. I also want to express my gratitude to my brother Ahmed for his constant support. Your collective presence has been a driving force, and I am truly thankful for the impact you've had on my academic endeavors.

List of Publications

Theoretical investigation of Cu_5/silicates deposited on rutile TiO_2 as a photocatalyst, Fatimah Alhawiti, Qingqing Wu, David Buceta, M. Arturo López-Quintela, Songjun Hou, Colin Lambert. Under review with PCCP.

Contents

Contents

1 Introduction

There is an urgent need to develop sustainable pathways for producing fuels and chemicals in the light of the rising demand for energy and the imminent effects of climate change, which is one of the most important issues facing humanity today [1]. On the one hand, clean hydrogen can be produced as a green energy through water splitting involving the hydrogen evolution reaction (HER)[2], and oxygen evolution reaction (OER)[3] by the use of various catalysts. On the other hand, the greenhouse impact is lessened by reducing carbon dioxide, which also produces fuels and chemical feedstocks such as carbon monoxide, formate, formaldehyde, methane, methanol, and C_{2+} hydrocarbons and oxygenates[4].

Catalysis are a fundamental element in driving chemical changes, serving as the cornerstone across a myriad of chemical procedures, spanning from laboratory-scale academic research to industrial applications [5]. The utilization of catalytic agents facilitates a reduction in transformation temperatures, minimizes waste derived from reagents, and elevates reaction selectivity, thereby fostering the potential for environmentally friendly practices. In 1998, Anastas and Warner introduced a foundational set of twelve principles in Green Chemistry, aiming to curtail or eliminate chemicals and chemical processes that pose adverse environmental impacts [6].

Presently, research efforts are concentrated on redefining processes for material and energy provision, aiming to minimize waste generation, hazardous by-products, and resource consumption. In this context, the creation, enhancement, and synthesis of novel catalysts play a pivotal role in advancing the field of fine chemistry [7]. Numerous methodologies have been extensively investigated to attain an optimal catalyst possessing stability, selectivity, and high activity concurrently, yet this remains a persisting challenge [8].

1.1 Solar-driven hydrogen generation

Hydrogen (H_2), considered to be a versatile energy carrier, stands out as a highly promising solution to address various energy challenges, attracting remarkable global attention. Its extraordinary appeal is attributed to its remarkably high gravimetric energy density, of approximately 120 MJ kg−1. Additionally, hydrogen has a near-zero greenhouse gas emissions profile and possesses the versatility to integrate into industrial infrastructure or power plants currently reliant on fossil fuels. This combination of attributes positions hydrogen as a compelling contender in the pursuit of clean energy alternatives [1, 9].

Presently, the production of H_2 relies heavily on fossil fuels, with over 90% of the global supply derived through processes such as steam methane reforming, methane partial oxidation, and coal gasification, but this conventional production approach is associated with significant environmental consequences, contributing to the release of approximately 830 million tons of carbon dioxide (CO_2) annually. This emission volume represents a noteworthy share, surpassing 2% of the total global annual CO_2 emissions [10, 11]. The solution to this emerging concern is to produce H_2 through water splitting

driven by renewable energies. Solar energy stands out as the most common and sustainable energy resource, distinguished by its abundance and renewability [12-18]. Owing to its vast availability and considerable potential for energy generation, solar energy emerges as the most auspicious energy source for producing sustainable H_2 through the splitting of water molecules. Solar-driven hydrogen (H_2) production technologies through water splitting today fall into various categories i.e photocatalytic (PC), photovoltaic−electrochemical (PV-EC), photoelectrochemical (PEC) and solar thermochemical (STC) water splitting [14, 16, 19, 20].

Over the last few decades, significant progress has been achieved in generating efficient, cost-effective, and stable photocatalytic materials. These materials, including metal oxides, metal sulfides, and metal (oxy)nitrides, exhibit the capability to generate hydrogen, oxygen, or both simultaneously.[17, 21-25] Despite these advancements, their application in industry is hindered by the relatively low conversion efficiency of solar energy. This limitation arises from the inefficiency of the three individual steps involved in the photocatalytic water decomposition process. Notably, charge separation and migration emerge as the most critical and intricate factors restricting the overall photocatalytic performance.[26]

To address this challenge, various strategies have been devised by experimental researchers. These include manipulating crystal morphologies,[27] creating junction structures,[28] incorporating optimal cocatalysts,[29] and synthesizing low-dimensional materials.[30] These efforts aim to enhance the efficiency of the charge separation and migration step, thereby advancing the overall performance of photocatalytic materials.

In the pursuit of achieving overall water splitting and understanding the structural intricacies influencing the performance of photocatalysts, a lot of research work has been

conducted on the two fundamental half-reactions involved in water splitting. These reactions are the hydrogen evolution reaction (HER) and oxygen evolution reactions (OER).

The technologies to achieve water splitting are broadly classified as Photocatalytic (PC), Photoelectrochemical (PEC), Photovoltaic-electrochemical (PV-EC), and Solar Thermochemical (STC) water splitting [31].

Numerous research papers and review articles have proposed diverse mechanisms explaining the process of photocatalytic water splitting [12, 22, 32]. The reaction starts with the absorption of photons, triggering the generation of numerous electron-hole pairs possessing sufficient potential. Subsequently, these charge carriers migrate towards the catalysts' surface and engage with active sites present there. Ultimately, the photo-induced electrons participate in the reduction of water to generate hydrogen, while the holes catalyze the oxidation of water molecules, leading to the production of oxygen. The mechanism discussed above is as follows [33]

$$H_2O + 2h^+ \longrightarrow 2H^+ + 1/2O_2 \quad E\ (\text{oxidation}) = -1.23\ V$$
$$2H^+ + 2e^- \longrightarrow H_2 \quad E\ (\text{reduction}) = 0V \qquad (1\text{-}1)$$
$$H_2O \longrightarrow H_2 + 1/2O_2$$

Oxide semiconductor photocatalysts have garnered a lot of research interest over the past few decades due to their promised uses in the effective conversion of sunlight into environmentally friendly and renewable energy as well as the remediation of environmental contaminants.[34, 35]. Photocatalytic water splitting is of two types i.e., single component water splitting and Z-scheme water splitting.

In single-component water spitting, when a semiconductor absorbs photons exceeding the bandgap energy, it initiates the generation of electrons and holes, which then diffuse

to the semiconductor surface, facilitating reduction and oxidation reactions, specifically HER and OER. Due to thermodynamic constraints, the Conduction Band Minimum (CBM) of photocatalyst must have lower potential than HER (0V vs NHE) while Valence Band Maximum (VBM) should be higher in potential than OER (+1.23V vs NHE). Furthermore, for sustained durability in the reaction, the photocatalyst's reductive and oxidative decomposition should be respectively lower and higher than the $H+/H_2$ and O_2/H_2O potentials which makes it hard to select the suitable semiconductors active for PC water splitting [31].

To surmount these challenges, the Z-scheme system was devised. This system combines two types of semiconductor photocatalysts, ensuring the separate production of H_2 and O_2 on their respective semiconductors [36]. Although semiconductors in this scheme cannot generate H_2 and O_2 simultaneously, their utility lies in their ability to produce either H_2 or O_2 from water. This is especially feasible with the support of redox mediators.

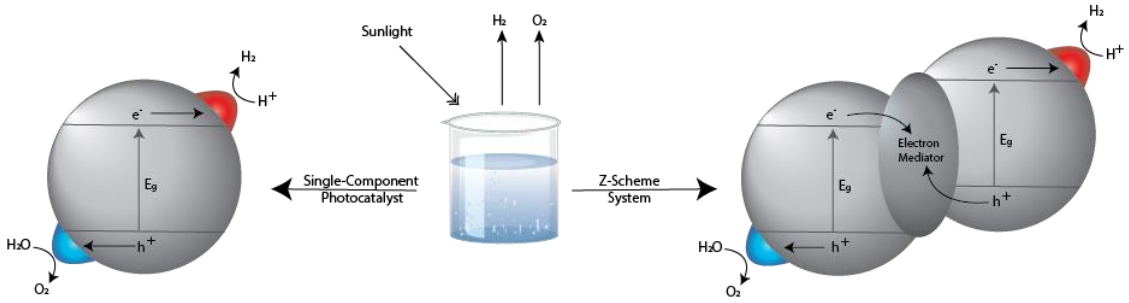

Figure 1 Single Component and Z-Scheme PC Water Splitting [36]

Different photocalysts have been developed, for instance, oxides ($NaTaO_3$:La), oxysulfides ($Y_2Ti_2O_5S_2$), oxynitrides (TaON), and carbon nitrides such as C_3N_4 for effective PC water splitting [16, 37]. To enhance the absorption of visible light separation of photogenerated charge, and to boost H_2 and O_2 evolution rates, different strategies have

been developed such as solid solutions, doping, and co-catalyst loading have been developed[16, 38].

A Photoelectrochemical Cell (PEC) typically comprises either a photoanode based on an n-type semiconductor for OER or a photocathode based on a p-type semiconductor for HER, along with the counter electrode for the complementary half-reaction [39-41]. Similar to the Z-scheme, it is not mandatory for the CBM and VBM of the photoanode and photocathode to simultaneously span the O_2/H_2O and $H+ /H_2$ potentials, provided that the CBM of the photocathode is lower than the water reduction potential, and the VBM of the photoanode is higher than oxidation potential, because an external bias is applied to facilitate the redox reactions [31]. When exposed to light, the photoanode produces electrons and holes. The electrons move through the external circuit to the counter electrode, initiating the HER, while the holes travel to the surface of the photoanode, where they catalyze the OER [31].

As a result of its high photocatalytic activity, resistance to photocorrosion, low cost, and nontoxicity, titanium dioxide (TiO_2) is a well-known and promising photocatalyst for producing hydrogen and splitting water[22, 42, 43], since the water was electrochemically photolyzed on a TiO_2 electrode by Fujishima and Honda in 1972[42]. The PEC reaction initiates when electrons and holes are produced in the conduction band and valence band, respectively, of a TiO_2 anode, an n-type semiconductor, when light has an energy higher than the band gap of TiO_2. These electrons travel through the bulk to reach the Pt counter electrode when an anodic potential is given via an external circuit, which turns H+ into H_2. In the meantime, water is oxidized by the holes left on the TiO_2 surface, producing O_2. In **Figure 2**, the overall reaction process is shown.

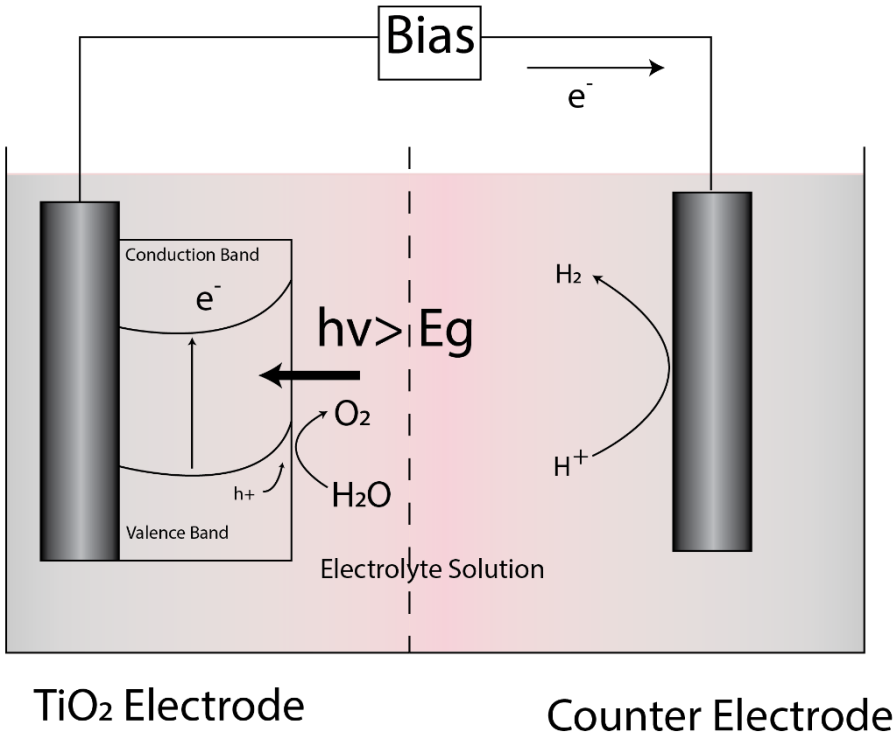

Figure 2 Photoelectrochemical water splitting on TiO_2 anode [44]

Many PEC cells have been invented recently, with many of them created especially to maximize the use of solar energy. However, the systems that have been presented up to this point have been rather complex, such as integrated multi-layer and tandem systems, because there is a dearth of adequate photoelectrode materials with proper band-gap topologies and stability.[45-47].

The Photovoltaic-electrochemical (PV-EC) system consists of two distinct components: the PV cell and the electrolyzer. The PV cell captures solar energy to generate electricity, which is then directly supplied to the EC cell. This enables the EC cell to split water into H_2 and O_2 at the cathode and anode, respectively. The PV cell is typically connected to both the cathode and anode, but is positioned outside the water electrolyte, preventing corrosion caused by water exposure [31]. Both PV cells and water electrolysis are

technologically advanced and commercially available, providing a key advantage for PV-EC water splitting over PC and PEC water splitting. Commercial PV cells boast efficiencies exceeding 18% and for the electrolyzers, within the range of 60−83%. Consequently, achieving a high solar-to-H2 efficiency exceeding 10% is readily attainable [14, 48, 49].

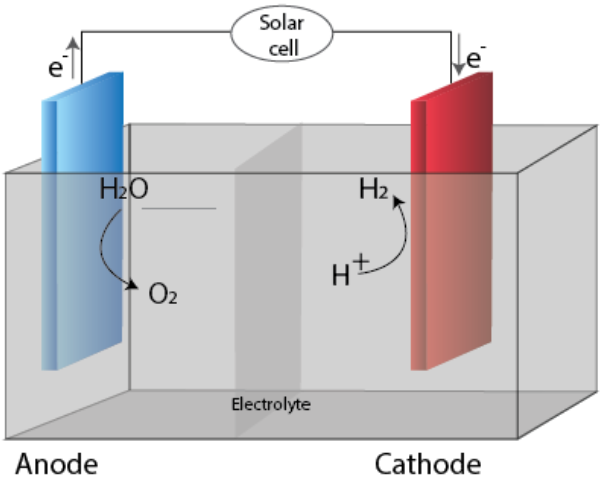

Figure 3 A general Photovoltaic-electrochemical (PV-EC) setup [31]

Solar Thermochemical (STC) water splitting cycles technology converts intense solar energy into thermal energy to facilitate the separation of water into H_2 and O_2 at elevated temperatures through a sequence of consecutive chemical reactions [50]. STC cycles encompass two primary classifications: two-step processes and multi-step processes[50-52]. In the initial stage, the exothermic reduction of the metal oxide enables the creation of the activated (reduced) metal oxide formed by the reduction of metal oxide in an exothermic reaction along with O_2 formation at high temperatures. This activated metal oxide efficiently extracts oxygen atoms from water during the subsequent water-splitting stage at a lower temperature, leading to H_2 generation. This comprehensive cycling procedure exclusively produces H_2 and O_2, through solar energy and water utilization.

The metal oxide can be recurrently reused within the cycling system. Additionally, due to the distinct steps in which H_2 and O_2 are produced, the generated H_2 is easily gathered with high purity, thereby eliminating the necessity for gas separation at high temperature [53].

$$Step\ 1: \quad M_xO_y \rightarrow M_xO_{y-\sigma} + \frac{\sigma}{2}O_2$$

$$Step\ 2: \quad M_xO_{y-\sigma} + \sigma H_2O \rightarrow M_xO_y + \sigma H_2$$

$$Net\ Reaction: \quad \sigma H_2O \rightarrow H_2 + \frac{\sigma}{2}O_2$$

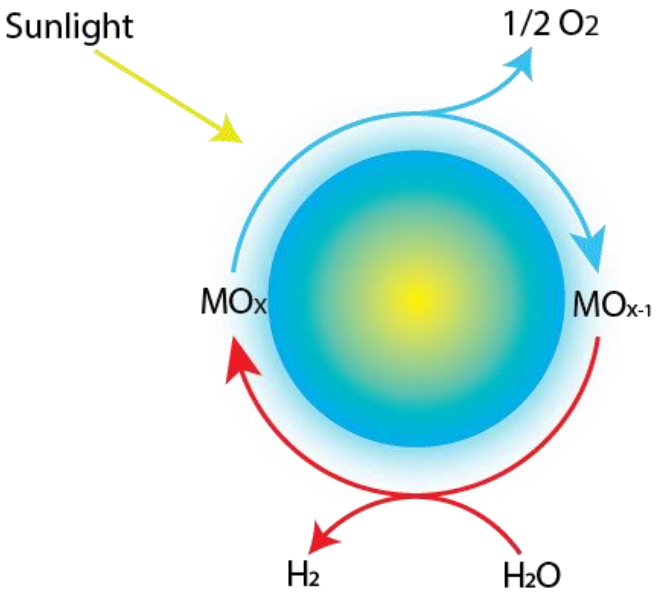

Figure 4 Schematic illustration of Solar Thermochemical (STC) water splitting cycle [31]

1.2 Electrochemical CO_2 reduction

The electrochemical carbon dioxide (CO_2) reduction reaction (CO_2RR) could contribute to a circular economy that will reduce unsustainable fossil fuel burning and thus reduce future net greenhouse gas emissions by using extra renewable electricity to manufacture useful fuels. [54-57].

CO_2 exhibits versatility in its conversion potential through various pathways, spanning biochemical [58], electrochemical [59], photochemical [60], radiochemical [61], and thermochemical reactions [62, 63]. Among these avenues, the direct electroreduction of CO_2 into hydrocarbons, hydrocarbon oxygenates, or CO stands out for several compelling reasons. Firstly, it aligns with environmental goals by coupling with carbon-free renewable energy sources like solar, tidal, and wind power. Secondly, this method operates effectively at ambient temperature and pressure, enhancing its practicality. Thirdly, the reactions can be finely controlled by adjusting external parameters such as electrolytes and applied voltages. Lastly, from an engineering and economic perspective, this approach demonstrates feasibility, contributing to its attractiveness in CO_2 conversion.

Electrochemical systems for carbon dioxide reduction reactions (CO_2RR) consist of essential components: an anode, a cathode, an aqueous electrolyte, and a membrane. At the anode, the OER occurs, while the cathode facilitates the CO_2RR process. The membrane plays a crucial role by segregating the products formed during oxidation and reduction products, ensuring charge balance, and establishing a closed loop system that facilitates protons transfer to the cathode [64].

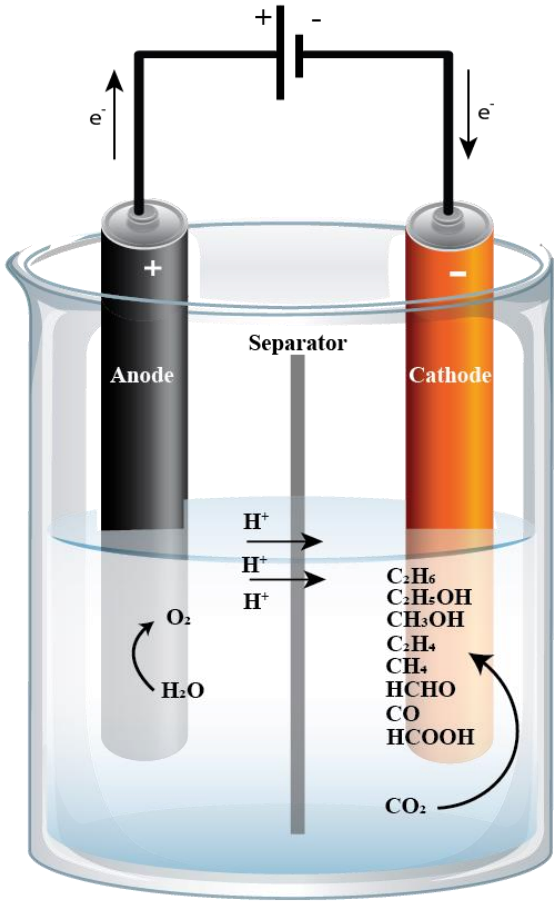

Figure 5 CO_2 reduction into different products [64].

Depending on number of electrons taken up by CO_2 during the reduction process, different products are formed as illustrated in the table below

Table 1 Products formed during CO_2 reduction reaction along with their electrochemical potential in aqueous solutions[64].

Chemical Reaction	Potential E (V vs RHE)
$2H^+ + 2e^- \rightarrow H_2$	0
$CO_2+2H^+ + 2e^- \rightarrow CO_{(g)} + H_2O$	-0.1
$CO_2 + 2H^+ + 2e^- \rightarrow HCOOH_{(aq)}$	-0.12
$CO_2 + 6H^+ + 6e^- \rightarrow CH_3OH_{(aq)} + H_2O$	0.03

$CO_2 + 8H^+ + 8e^- \rightarrow CH_{4(g)} + 2H_2O$	0.17
$2CO_2 + 12H^+ + 12e^- \rightarrow C_2H_{4(g)} + 4H_2O$	0.08
$2CO_2 + 12H^+ + 12e^- \rightarrow C_2H_5OH_{(aq)} + 3H2O$	0.09
$2CO_2 + 14H^+ + 14e^- \rightarrow C_2H_{6(g)} + 4H_2O$	0.14

The rate determining step of CO_2RR typically involves the initial electron transfer, leading to the formation of the $*CO_2^-$ *intermediate (** denoting the adsorption site). The reactivity exhibited by $*CO_2^-$ decides the distribution of products [65]. Subsequent to this critical step, the O atom of $*CO_2^-$ becomes affixed to the surface of metal electrocatalyst. In this scenario, the carbon atom undergoes protonation, giving rise to *OCHO, from which either formic acid or formate emerges as the product. Conversely, when the carbon atom of $*CO_2^-$ binds to the surface of metal electrocatalyst, protonation of the O atom occurs, resulting in the formation of *COOH(see **Figure *44***). Following an electron transfer event, *CO is subsequently generated, giving off CO from the surface of catalyst [66]. In essence, the selectivity characterizing the CO_2RR is linked to the binding capabilities exhibited by *OCHO, *COOH, *CO, and *H on the surface of the catalyst.

The mechanism for electrochemical oxidation and reduction mechanism taking place at anode and cathode respectively are illustrated in **Figure 6**. When external positive bias is applied at the electrode (anode), the chemical potential of the metal electrode decreases. Consequently, the highest occupied molecular orbital (HOMO) of the molecule (i.e. H_2O in our case), becomes higher in energy and loses its electron to the anode, resulting in the oxidation of the molecule and thus the formation of O_2 as a product.

On the other hand, when negative external bias is applied, the chemical potential of the metal electrode (cathode) becomes higher in energy than the lowest unoccupied molecular orbital (LUMO) of the nearby molecule (i.e CO_2). The LUMO of CO_2 accepts the electrons from the cathode, resulting in reduction and the formation of different products.

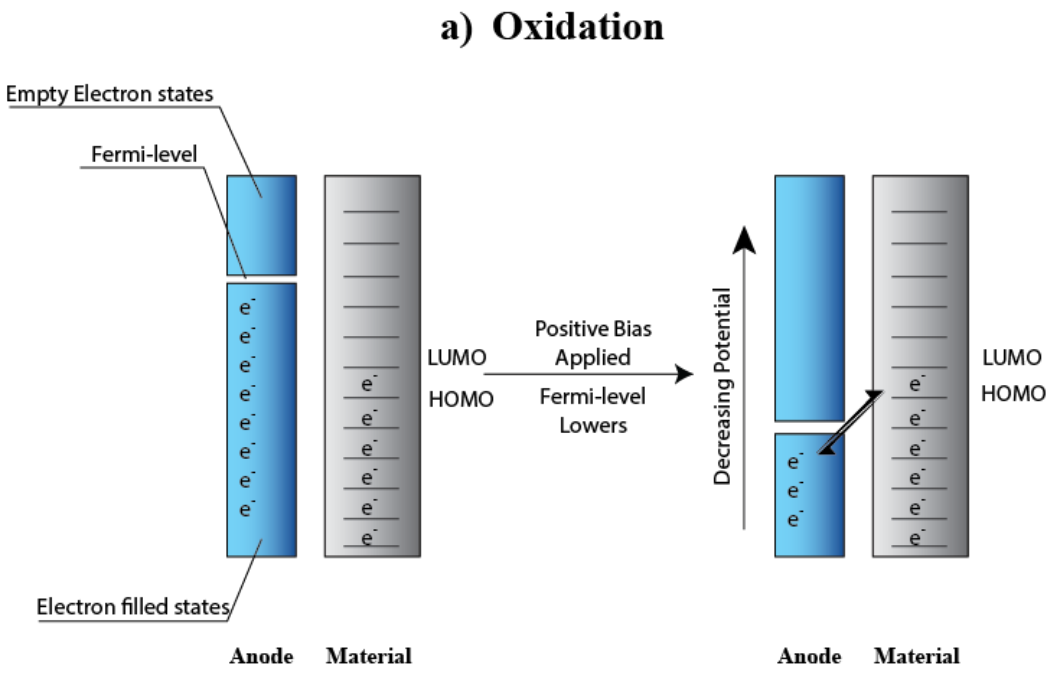

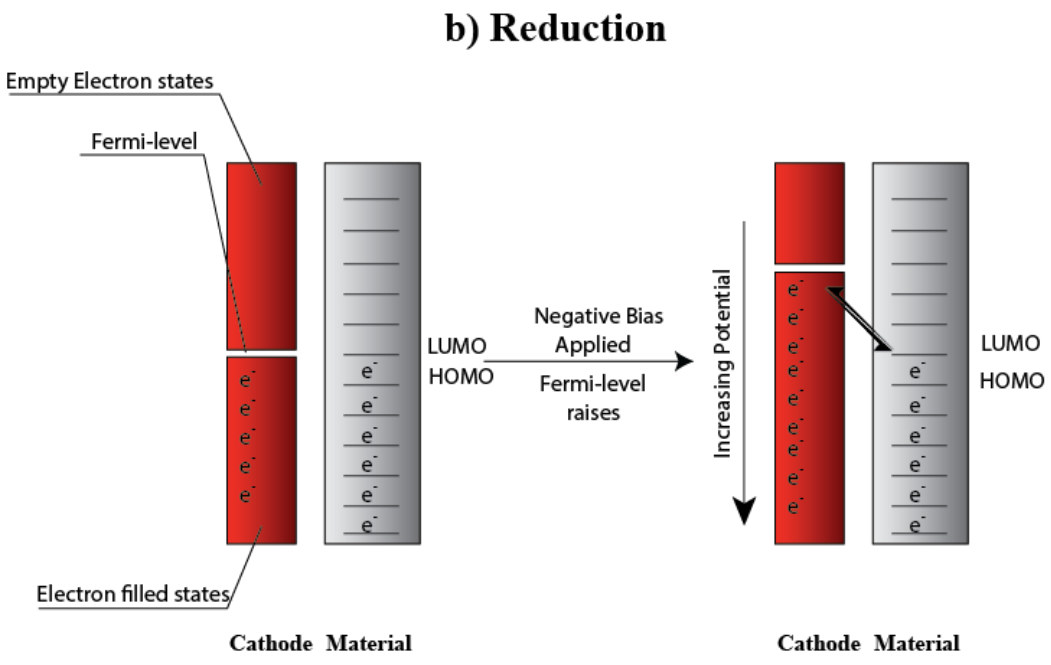

Figure 6 Mechanisims of electrochemical oxidation and reduction taking place at anode and cathode respectively

One of the important products that may be produced from CO_2 is formic acid (HCOOH), which is used for chemical raw materials such as hydrogen carriers for petrochemical and fuel cell applications. [67, 68]. Various transition metal catalysts such as Pd, Pt, and Cu have been introduced for the production of HCOOH from CO_2 [68, 69]. Previous research showed that copper has a special ability to create hydrocarbons and other multi-carbon compounds[70].

A bifunctional nickel-nitrogen-doped carbon-supported copper electrocatalyst for CO_2 reduction was created [71], showcasing the material's potential for enhanced catalytic qualities. A copper atom-pair catalyst that was anchored on alloy nanowires was described, as having excellent selectivity, activity, and stability in the electrochemical reduction of CO_2[72]. Together, these investigations demonstrate the promise of copper-based electrocatalysts for the effective and selective conversion of CO_2 to higher-value compounds, especially those with particular surface structures and compositions. A single unit cell of Cu is illustrated in **Figure 34**. The Cu (111) surface is chosen and studied in this thesis.

1.3 Catalytic Properties of AQCs.

In recent years, sub-nanometer atomic quantum clusters (AQCs), composed of a few metal atoms, have garnered significant attention due to their unique properties compared to larger nanoparticles. These clusters, distinct from nanoparticles, do not require organic ligands for stabilization in solution, lack plasmonic support, and possess electron-volt-scale HOMO-LUMO gaps [73-75]. The investigation into these tiny atomic clusters and

nanoalloys remains an area of ongoing interest, with numerous characterizations conducted.

Gas-phase cluster studies have provided crucial thermodynamic data for testing theoretical models and establishing the structural, energetic, and reactive properties of size-selected clusters. AQCs, synthesized electrochemically with kinetic control, have spurred recent explorations into their catalytic [76-78], photocatalytic [79, 80], and potential chemotherapy applications [81].

These sub-nanometer-sized metal clusters exhibit molecule-like electronic structures, distinguishing them from visible region metal nanoparticles [82]. Their lack of sustained metallicity and plasmonic behavior is compensated by their unique HOMO-LUMO gap, influencing their chemical and physical characteristics. This makes them promising materials for various applications such as luminescence [83], sensing [84], therapeutics [81], energy conversion [85], catalysis [78], and electrochemical applications [86, 87].

The emergence of catalytic properties in clusters is the result of interactions among the dimensions and configuration of the clusters, how they engage with the support material, their oxidation levels, and the effects of quantum size [88]. These catalysts serve as potent agents for a range of chemical processes, such as oxidation, reduction, and hydrogenation. This distinctive performance is attributed to multiple factors including the elevated ratio of surface-to-bulk atoms [89], the electronic shell closures explained by the Jellium model [90, 91], closures in geometric shells [92], superatomic features where electron distribution among atoms deviates from that in bulk materials [93], and quantum confinement effects [74].

Through the selection of diverse metals, modification of the metal-metal (M-M) dimensions, and the choice of suitable supports, one can tailor their characteristics for

optimal performance [94]. Advantages provided by these catalysts include lower activation energies, enhanced conversion rates and specificity, along with the capability to function under milder temperatures and pressures. Moreover, they demonstrate remarkable durability and a heightened tolerance to typical catalyst inhibitors, such as sulfur and carbon monoxide, in comparison to traditional catalysts [94].

As metal clusters shrink to dimensions on par with the Fermi wavelength ($\lambda_f < 1$ nm), transitioning into the sub-nanometer domain, quantum confinement influences lead to the discretization of electronic states, manifesting as a distinct HOMO–LUMO gap. In this context, electrons do not exhibit the complete delocalization characteristic of bulk metals, causing these clusters to exhibit properties of non-metals [95, 96]. Therefore, their geometric, electronic, and size-dependent features are closely interconnected and should be analyzed in unison.

In particular, Cu_5 clusters have shown promise as catalysts due to their higher resistance to oxidation compared to larger systems like Cu_8 or Cu_{20} [76, 77]. These clusters, synthesized under kinetic control through electrochemical methods, exhibit exceptional thermodynamic and chemical stability in solution across a wide pH range and are also resistant to oxidation even at 423 K [77, 97]. This method of synthesis ensures high monodispersity, making Cu_5 clusters highly size-selective. The outer unpaired electrons of open-shell clusters like Cu_5 are anticipated to be more actively involved in chemical reactivity, potentially through sharing or transferring them, in contrast to closed-shell cases.

1.4 Thesis Outline

The thesis is divided into six chapters.

The present chapter provides a concise introduction to catalysis in the realm of green energy, focusing on key catalysts such as titania and copper. Delving into various types and applications, this chapter explores the pivotal role these catalysts play in advancing environmentally sustainable energy solutions. Chapter 2 gives information about the development of DFT in particular, as well as the history of the theories that support the computational calculations utilized in this thesis.

Chapter 3 describes the theoretical underpinnings of the approach employed in the work given here. The application of VASP software with a plane wave basis set is described in general terms. Finally, the geometries optimization procedure is briefly described, and some calculated quantities are explained to understand better the work presented in the following chapters.

Chapter 4 focuses on the impact of the deposition of small trapezoidal and bipyramidal copper AQCs on the photocatalytic activity of perfect and defective rutile (110) TiO_2 surfaces in the absence and presence of silicate. It is found that these copper AQCs are oxidized, donating their electrons to the substrates resulting in the formation of a surface polaron within the band gap of the bulk. Furthermore, there are hybrid states located on copper atoms in case of the presence of Cu_5/ SiO_3^{2-}along with an oxygen vacancy. These gap states are essential for enhancing the metal oxides' photocatalytic activity.

Chapter 5 explores the reduction of CO_2 on Cu (111) interfaces that are either pristine or defective. To understand the CO_2 reduction mechanisms on both surfaces, we investigate two reaction pathways using density functional theory (DFT) calculations: the formate (formic acid) and CO pathways. In addition, we study the impact of the defective Cu (111) interface on Cu_5 atomic quantum clusters (AQCs). Carbon monoxide (CO) and formic acid (HCOOH) are synthesized from COOH and HCOO intermediates using spin-

polarized DFT. This energy diagram is the result of the electroreduction of CO_2. The outcomes demonstrate Cu_5/Cu (111) as a promising catalyst with great potential for CO_2 hydrogenation, an essential process for the synthesis of CO and formic acid. For the production of Formate and CO, both surfaces show lower Gibbs free energy barriers, highlighting the catalytic enhancement provided by Cu_5 clusters.

2 Density Functional Theory

2.1 Introduction

Density Functional Theory (DFT) has enormously revolutionized different fields of research since its first appearance in 1964 under the theorems put forward by Hohenberg and Kohn [98]. It is one of the most advanced computational techniques to study a molecular or atomic system's morphology, characteristics, properties, and energetics. The evolution of quantum chemistry, specifically focused on the study of small objects, has expanded to a much larger scope that now also includes different spectroscopic calculations, mainly based on DFT [99].

The key focus of this chapter is to introduce Density Functional Theory, starting from the basics of the Schrodinger wave equation, going all the way through Born and Oppenheimer's approximations to the theorems of Hohenberg and Kohn, and finally concluding on the Khan-Sham formalism. The basic principle of DFT states that the electron density at each point can be used to determine the ground state properties of a molecular or an atomic system. DFT is used in physics and chemistry as a QM (Quantum Mechanical) method for calculating the electronic structure of different types of molecules, atoms, and solids [100]. DFT finds its application in diverse fields, including

prediction of geometries, energetics, reaction mechanisms, optical spectra, exchange couplings, and different spectroscopies such as X-Ray absorption, EPR, and Mossbauer spectroscopy [101].

During my Ph.D. studies, I performed my activities on a computer software named Vienna Ab initio Simulation Package (VASP), which is built on DFT to decipher the Kohn-sham equation for a system containing a bunch of particles. I have used this program to perform calculations for geometric and electronic structures, and energetics. This section focuses on a short rundown of DFT's establishments and mathematical applications. For a detailed approach, Martin et al. and Koch et al. demonstrate a significantly more comprehensive treatment of Density Functional Theory [102, 103].

2.2 Schrodinger equation

The fundamentals of DFT are based on the Schrodinger wave equation, which Erwin Schrodinger put forward in 1926 [104]. This wave equation illustrates the progression of wave function ψ over time, and solving this equation can reveal some essential properties about a system, such as the energy, trajectory and positioning. The time-independent Schrodinger wave equation in its simplest form is given by

$$\hat{H}\,\Psi = E\Psi \qquad (2\text{-}1)$$

where the Hamiltonian operator is represented by $\hat{H}$, the wave function is depicted by Ψ, and E is the eigenvalue of the state's energy. Hamiltonian operator in classical mechanics comprises an operator for kinetic energy ($\hat{T}$) as well as an operator for potential energy ($\hat{V}$) given by

$$\hat{H} = \hat{T} + \hat{V} \tag{2-2}$$

$$\hat{H} = -\frac{\hbar^2}{2m}\nabla^2 + \hat{V} \tag{2-3}$$

Here $\hbar$ is the Plank`s constant in its reduced form given by $\hbar = \frac{h}{2\pi}$, $\hat{V}$ is the potential energy and ∇ is the Laplacian operator in three-dimensional cartesian coordinate system as

$$\nabla^2 = \frac{\delta^2}{\delta x^2} + \frac{\delta^2}{\delta y^2} + \frac{\delta^2}{\delta z^2} \tag{2-4}$$

When considering a system with only a few electrons, the solution of the Schrodinger equation is feasible and practicable. However, when we carry out calculations for a many-body system, i.e., a system comprising a bunch of atoms and electrons, the solution of the Schrodinger equation becomes complicated and challenging. The deep-rooted objective of theoretical chemistry and physics is to identify ways for resolving the problems related to quantum many-body systems [105]. Some approximations are introduced for the solution of such a complex system, which are discussed as follows.

2.3 Born-Oppenheimer Approximation

It is usually impossible to compute accurate values for many-body problems in quantum chemistry by solving Schrödinger's equation as it involves complex interactions between several nuclei and electrons. Generally, the Hamiltonian operator for a many-body system is composed of five different parts.

$$\hat{\mathrm{H}} = \hat{\mathrm{T}}_{\mathrm{e}} + \hat{\mathrm{T}}_{\mathrm{n}} + \hat{\mathrm{V}}_{\mathrm{nn}} + \hat{\mathrm{V}}_{\mathrm{ee}} + \hat{\mathrm{V}}_{\mathrm{ne}} \tag{2-5}$$

As depicted through the equation, this Hamiltonian consists of two operators $\hat{T}_e$ and $\hat{T}_n$ for the kinetic energy of electrons and nuclei respectively. Similarly, the remaining three operators $\hat{V}_{nn}$, $\hat{V}_{ee}$ and $\hat{V}_{ne}$ are the operators of potential energy for the repulsion between

the nuclei, for electronic repulsion, and for nuclear-electronic attraction respectively. Plugging the values of all these operators in equation *(2-5)*, we get,

$$H = -\sum_i \frac{\hbar^2}{2m}\nabla_i^2 - \sum_I \frac{\hbar^2}{2M}\nabla_I^2 + \frac{1}{4\pi\varepsilon_0}\frac{1}{2}\sum_{I\neq J}\frac{Z_I Z_J e^2}{|R_I - R_J|} + \frac{1}{4\pi\varepsilon_0}\frac{1}{2}\sum_{i\neq j}\frac{e^2}{|r_i - r_j|} - \frac{1}{4\pi\varepsilon_0}\sum_{i,I}\frac{Z_I e^2}{|r_i - R_I|} \quad (2\text{-}6)$$

For the simplification of the Schrodinger wave equation, while solving a problem pertaining to a system consisting of numerous interacting particles, we can introduce the Born-Oppenheimer approximation, which states that the molecular wave function can be separated into two parts, the nuclear part represented by $\Psi_n(R)$ and the electronic part is represented by $\Psi_e(r,R)$ [106].

$$\Psi(\mathrm{r},\mathrm{R}) = \Psi_\mathrm{e}(\mathrm{r},\mathrm{R})\Psi_\mathrm{n}(\mathrm{R}) \quad (2\text{-}7)$$

where R and r represent the nuclear and electronic coordinates respectively.

Furthermore, the nuclear part of the equation can be neglected since nuclei are much heavier than the electrons, so we can consider the nucleus to be fixed at a place with respect to moving electrons. As only the electronic part of the molecular wave function is considered in solving the Schrodinger equation to get the eigenvalue for electronic energy, the Hamiltonian is simplified as follows,

$$\hat{H}_e = \hat{T}_e + \hat{V}_{ee} + \hat{V}_{ne} \quad (2\text{-}8)$$

Plugging in this Hamiltonian operator in the Schrodinger equation, we get

$$\hat{H}_e\Psi_\mathrm{e}\,(r,R) = E_e\Psi_e(r,R) \quad (2\text{-}9)$$

Even with the Born-Oppenheimer approximation reducing much of the system's complexity, solving the Schrodinger equation for a multi-electronic system is still much more challenging. Therefore, Density Functional Theory comes in to solve this quantum many-body problem.

2.4 The Hohenberg-Kohn Theorems

The two theorems put forward by the scientists Hohenberg and Kohn in the year 1964 serve as basic elements behind the establishment of Density Functional Theory as a fundamental methodology for determining all the properties of a system under consideration at its lowest energy state i.e., the ground state [98].

According to the first Hohenberg-Kohn theorem, the ground state energy of a multi-particle system having a fixed inter-particle interaction is an exclusive function of its electronic density in the existence of external potential. To prove this, assume two different external potentials V_a and V_b having identical non-degenerate ground state density with Hamiltonian operators H_a and H_b respectively. Each of these Hamiltonian can be used in the Schrodinger equation to obtain ground-state wavefunction Ψ_a and Ψ_b associated with the eigenvalue of energy as E_a and E_b respectively. The Ground state energy corresponding to H_a must be lesser than the expected value of H_a over Ψ_b

$$E_a < \langle \Psi_b | H_a | \Psi_b \rangle \tag{2-10}$$

Adding and subtracting H_b equation (2-10), we get

$$E_a < \langle \Psi_b | H_a - H_b + H_b | \Psi_b \rangle$$

$$E_a < \langle \Psi_b | H_a - H_b | \Psi_b \rangle + \langle \Psi_b | H_b | \Psi_b \rangle \tag{2-11}$$

$$E_a < \langle \Psi_b | V_b - V_b | \Psi_b \rangle + E_b$$

Introducing the ground-state density into equation (2-11), we can rewrite the equation as

$$\mathrm{E_a} < \int [\mathrm{V_a(r)} - \mathrm{V_b(r)}]\, \rho_0(\mathrm{r}) \mathrm{dr} + \mathrm{E_b} \tag{2-12}$$

Since a and b can be used interchangeably, hence the equation *(2-12)* gives

$$E_a < \int [V_b(r) - V_a(r)]\, \rho_0(r) dr + E_a \tag{2-13}$$

In addition to equations 2.12 and 2.13, we are left with a clearly contradicting inequality as

$$E_a + E_b < E_b + E_a \tag{2-14}$$

Hence the first theorem proves that two different external potentials (in our case, V_a and V_b) cannot yield the identical lowest energy state of electronic density.

The second theorem gives one of the most significant interpretations about the energy functional E(n) i.e. the energy functional can be used to find all the ground state properties of a system. Applying the variational theorem can give us true ground state density by varying the value of the electronic density to find the one true value which reduces the energy functional to its lowest possible figures. So, the statement of the second theorem asserts that the value of electron density $\rho_0\ (r)$ which gives the minimum magnitude of overall energy functional E_0 is the true ground state electron density which can be used to calculate important properties of a system under consideration. The total energy of the system can be stated as:

$$E[\rho] = \int dr V_{ex}(r)\rho(r) + F_{HK}[\rho] + E_{nn} \tag{2-15}$$

where V_{ex} is the external potential, E_{nn} is the term for nuclear-nuclear repulsion and F_{HK} includes two terms, $T_e\,[\rho]$ and $V_{ee}[\rho]$ for electronic kinetic energy and potential energy of electronic repulsions respectively. So according to the second theorem, if we have any energy functional $E[\rho(r)]$ then it should be less than the ground state energy functional $E_0[\rho_0(r)]$

$$E[\rho(r)] > E_0[\rho_0(r)] \tag{2-16}$$

Hence, the ground state density is the electron density for which the energy functional has its lowest possible value. Therefore, by getting the minimum value for equation (2-15), we can calculate all the ground state properties of the system.

2.5 The Kohn-Sham Scheme:

The effective form of DFT as it is known today is based on the pioneering works of Kohn and Sham in 1965 [107]. To evaluate the Schrodinger equation for a multi-electronic system, they considered a fictitious system consisting of noninteracting particles. They formulated a form of the Schrodinger equation which produces the same value for the ground-state electronic density of the noninteracting system as that of the interacting one[108-110]. Kohn and Sham fixed the Hamiltonian in the Schrodinger wave equation to make it applicable to noninteracting systems. This fixed Hamiltonian is given by

$$H_{KS} = \frac{1}{2}\left(\frac{\delta}{\delta x} + \frac{\delta}{\delta y} + \frac{\delta}{\delta z}\right)^2 + V_{eff} \tag{2-17}$$

The Kohn-Sham energy has two components, a known and unknown factor. The unknown component i.e. the exchange of correlational energy can be evaluated through different approximation methods. The kinetic energy of the system is given by:

$$T[\rho] = T_s[\rho] + T_c[\rho] \tag{2-18}$$

where $T_s[\rho]$ is the kinetic energy of the noninteracting particle whereas $T_c[\rho]$ is a correlational term for the kinetic energy of the particle in the interacting system. Similarly, the potential energy is also divided into two components, of which one is simple and known whereas the other is complex and unknown.

$$V_{ee}[\rho] = V_H[\rho] + V_x[\rho] + V_c[\rho] \tag{2-19}$$

Here $V_H[\rho]$ is known as the Hartree term given by [111-113]:

$$V_H[\rho] = \frac{1}{2}\iint dr dr' \frac{\rho(r)\rho(r')}{|r - r'|} \tag{2-20}$$

The other two components of the equation i.e. $V_x[\rho]$ and $V_c[\rho]$ denotes exchange energy and electronic correlation term respectively. Both of these two terms along with $T_c[\rho]$

from equation (2-18) can be calculated through approximation methods. The final form of Kohn-Sham energy functional is given by:

$$E_{KS}[\rho] = T_s[\rho] + V_H[\rho] + E_{XC} + E_{nn} \quad (2\text{-}21)$$

where E_{XC} is the exchange correlational energy functional which is the sum of $V_x[\rho]$, $V_c[\rho]$ and $T_c[\rho]$. Using our proposition of a fictitious noninteracting single electron system, the wave function of a many-body system can be represented through a slater determinant of a single electronic wave function. Hence, the electron density is given by:

$$\rho(r) = \sum_{i=1}^{N} |\phi_i(r)|^2 \quad (2\text{-}22)$$

Therefore, the Schrodinger equation in terms of the Kohn-sham approach takes its final form as follows:

$$\left(-\frac{1}{2}\nabla_i^2 + V_{eff}(\rho(r))\right)\phi_i(r) = \epsilon_i\phi_i(r) \quad (2\text{-}23)$$

where V_{eff} represents the effective external potential that comes from a nucleus and any other external field. All of the energy terms i.e. $T_s[\rho]$, $V_H[\rho]$ and E_{nn} as depicted in equation 2.20 can be calculated in their true mathematical form except E_{XC} as there is no precise solution to finding the exchange correlational part, so we have to introduce some approximations.

2.6 Approximations for exchange-correlation functional

The Kohn-Sham approach solves the problem of a many-body system by reducing it to one electron system through the addition of an exchange-correlation part that takes care of all the interactions between electrons [114]. Unfortunately, there is no precise way of calculating or determining the true form of the exchange-correlation part, so approximations have to be introduced. Local Density Approximation (LDA) and

Generalized Gradient Approximation (GGA) are the two methods for approximating the exchange correlational function.

2.6.1 Local Density Approximation

Of the hundreds of approximation methods that have been used for finding exchange-correlation functions, LDA has been the simplest of all [115]. Scientists have used the LDA method for a long time by considering a uniform and slowly changing local electron density of the system to evaluate exchange-correlation functional [116]. Despite it being very simple, LDA has been in use to perform calculations of complex atomic structures, elastic and vibrational properties, and also in performing solid-state calculations.

In the LDA approach, the electron density of the system is considered to be smooth locally. The term local refers to the fact that the exchange of correlational energy at a place within a system is a function of its electronic density at that place only. The exchange correlational energy according to LDA is given by:

$$E_{XC}^{LDA}[\rho(r)] = \int dr\rho(r)E_{XC}^{HG}[\rho(r)] \qquad (2\text{-}24)$$

Here E_{XC}^{HG} is a term representing the exchange correlational energy of a homogenous gas system where electron density $\rho(r)$ has been considered as varying uniformly. E_{XC}^{HG} is further divided into two components, the exchange component E_X^{HG} and correlational component E_c^{HG}.

$$E_{XC}^{LDA}[\rho(\vec{r})] = \int dr\rho(\vec{r})(E_X^{HG} + E_c^{HG})[\rho(\vec{r})] \qquad (2\text{-}25)$$

The exchange energy component in the above equation is given by

$$E_x^{HG} = -\frac{3}{4\pi}\sqrt[3]{3\pi^2\rho} \qquad (2\text{-}26)$$

LDA is considered the best and most accurate approach for systems with uniformly varying electron density such as carbon nanotubes and graphene. Despite having many advantages, there are some drawbacks to this method, for instance, its inability to perform proper energetics calculations for some molecular and solid systems, makes room for the GGA method to take over LDA in DFT calculations [117].

2.6.2 Generalized Gradient Approximation:

When considering a molecular system, the electron density is not uniformly distributed, therefore, LDA becomes inapplicable to such systems. This leads us to Generalized Gradient Approximations (GGA). GGA is a many-fold improvement over LDA as GGA performs in the systems where LDA fails to. GGA introduces the concept of electronic density gradient to calculate the exchange-correlation term for the systems having non-homogenously distributed electron density which LDA fails to explain. The exchange-correlation term is given by:

$$E_{xc}^{GGA}[\rho(\vec{r})] = \int d(\vec{r})\rho(\vec{r})\epsilon_{XC}^{GGA}[\rho(\vec{r}), |\nabla\rho(\vec{r})|] \qquad (2\text{-}27)$$

GGA is a much better approximation method than LDA as it allows accurate calculations for a lot of properties that can`t be evaluated through the LDA approach.

The calculations within this thesis are performed through the VASP computer program with Generalized Gradient Approximation (GGA) for optimization of geometry and Heyd–Scuseria–Ernzerhof (HSE06)[118] hybrid exchange-correlation functional for the calculation of electronic properties, electronic structure, and band gap.

2.6.3 Hybrid Functionals

To address the limitations of both Density Functional Theory (DFT) and Hartree-Fock (HF), hybrid functionals were proposed by Becke in 1993 [119]. Hybrid functionals, within the framework of density functional theory (DFT), represent a category of

approximations to the exchange–correlation energy functional. These functionals integrate a segment of exact exchange derived from Hartree–Fock theory with the remaining exchange–correlation energy obtained from alternative sources, whether empirical or ab initio. They incorporate a fraction of exact exchange, which improves the description of certain properties such as electronic excitation energies and reaction barriers. This makes hybrid functional methods more accurate for certain types of calculations compared to standard density functional theory methods. [120]

In the study of semiconductor and insulator materials using DFT, two common approximations are the Local Density Approximation (LDA) and the Generalized Gradient Approximation (GGA). However, these techniques often tend to underestimate the band gap of such materials, leading to inaccuracies in predicting electronic states. On the other hand, the HF technique tends to overestimate the band gap, resulting in excessive localization of electronic states. To accurately determine the band gap value and achieve the appropriate localization of electronic states, a judicious combination of HF and LDA/GGA is necessary. This blending approach is referred to as the hybrid functional method because of the adiabatic connection approach. PBE0, a widely used hybrid functionals , proposed by Adamo and Barone, is a mixture of Perdew–Burke-Ernzerhof (PBE) and HF exchange energy in 3:1, plus the PBE correlation energy:[121]

$$E_{XC}^{P} = \frac{1}{4}E_{X}^{HF} + \frac{3}{4}E_{X}^{P} + E_{c}^{P} \qquad (2\text{-}28)$$

E_{x}^{HF} and E_{X}^{P} represents HF and PBE exchange functional respectively whereas E_{c}^{P} represents PBE correlational functional.

While hybrid functionals offer better accuracy in DFT calculations, they come with an increased computational cost compared to other DFT techniques where the exchange is

treated non-locally. Non-local treatment refers to considering the long-range interactions between electrons in a system. To address this challenge, a common strategy is to decompose the exact exchange into short-range (sr) and long-range (lr) parts. This decomposition helps in managing the computational complexity associated with long-distance interactions. The decomposition is achieved by splitting the Coulomb interaction as follows [122]:

$$\frac{1}{r} = \frac{erfc(\omega r)}{r} + \frac{\mathrm{erf}(\omega r)}{r} \qquad (2\text{-}29)$$

Here, r represents the distance between the charges while ω represents the screening factor. One of the popularly used hybrid functional involving this technique is HSE06.

To address the computational cost issue, Heyd, Scuseria, and Ernzerhof (HSE) developed a technique. In this technique, they introduced a screened Coulomb potential to expedite the computation of the exact exchange part. The term "screened" means that the long-range part of the Hartree-Fock (HF) exchange interaction is modified to reduce its impact, making the computation more efficient. In HSE06, often referred to as HSE simply, the exchange potential has two components, one is a long-ranged Perdew-Burke-Ernzerhof (PBE) part combined with Hartree-Fock exchange whereas the second part is a long-ranged PBE component.[118]

$$E_X^{HSE06} = \frac{1}{4}\left(E_x^{HF,sr,\mu}\right) + \frac{3}{4}\left(E_X^{PBE,sr,\mu}\right) + E_x^{PBE,lr,\mu} + E_c^{DFT} \qquad (2\text{-}30)$$

Here, the parameter μ is empirically defined. For the calculations of charge dispersions, the Bader analysis approach can be applied to the results of HSE06 calculations. Although HSE gives perfect results, it requires a lot of time and a lot of memory to work with.

2.6.4 B3LYP

The B3LYP method represents a hybrid approach to the exchange-correlation functional, distinguished by its precision and widespread acceptance. This method constructs its exchange-correlation potential through various elements. It primarily derives the exchange-correlation energy from the LSDA approach, incorporating 20% of the discrepancy between the exchange energy according to Hartree-Fock and that calculated by LSDA. It also integrates 72% of Becke's exchange functional from 1988 and 81% of the Lee-Yang-Parr correlation functional's non-local component. This strategic combination yields the B3LYP functional [123, 124].

$$E_{xc} = E_{xc}^{LSDA} + 0.20(E_x^{HF} - E_x^{LSDA}) + 0.72E_x^{B88} + 0.81E_c^{LYP} \qquad (2\text{-}31)$$

The nonlocal Hartree-Fock E_x^{HF} can be written as

$$E_x^{HF} = -\frac{e^2}{2}\sum_{nk,mq} f_{nk}f_{mq} \times \int\int d^3r d3r' \frac{\psi_{nk}^*(r)\psi_{mq}^*(r')\psi_{nk}(r')\psi_{mq}(r)}{|r-r'|} \qquad (2\text{-}32)$$

Featuring $\psi_{nk}(r)$ as the collection of single-electron Bloch states within the system, and f_{nk} as the associated set of (potentially fractional) occupation numbers. The summations across k and q involves all of the k points selected for sampling the Brillouin zone (BZ). Meanwhile, the summations over (m) and (n) extend across all bands at these k points. The corresponding nonlocal Hartree-Fock potential is described as follows.

$$V_x^{HF} = -\frac{e^2}{2}\sum_{mq} f_{mq} \frac{\psi_{mq}^*(r')\psi_{mq}(r)}{|r-r'|} \qquad (2\text{-}33)$$

$$V_x^{HF} = -\frac{e^2}{2}\sum_{mq} f_{mq} e^{-iqr'} \frac{u_{mq}^*(r')u_{mq}(r)}{|r-r'|} e^{-iqr'} \quad (2\text{-}34)$$

In this context, $u_{mq}(r)$ denotes the periodic component of the Bloch wave function, $\psi_{nq}(r)$, at a specific momentum point, q, associated with m (band index).

2.6.5 Meta-GGA

To formulate expressions that adhere to more exact constraints, it becomes necessary to understand electron density information deeply, beyond merely its local values and their gradients. This requirement leads to the development of meta-GGAs [125, 126]. Meta-GGAs go a step further than just utilizing the electron density and its gradient by also considering aspects such as the non-interacting kinetic energy density.

The concept of non-interacting kinetic energy density, denoted as $\tau(r)$, is introduced as follows:

$$\tau(r) = \left(\frac{\hbar^2}{2m_e}\right)\sum_i |\nabla\phi_i(r)|^2 \quad (2\text{-}35)$$

Here, the summation extends over all the occupied Kohn-Sham orbitals. Incorporating this kinetic energy density into the calculation of the exchange-correlation energy per particle results in a functional that relies locally on the Kohn-Sham orbitals, moving beyond a purely density-based functional.

General Concept of a Meta-GGA A meta-GGA is conceptually described as a function that depends on the local electron density $\rho(r)$, the square of its gradient (s^2), its Laplacian (q), and the kinetic energy density (τ). This conceptualization can be expressed as:

$$E_{xc}^{mGGA} = \int \rho(r)\epsilon_{\mathrm{xc}}^{mGGA}(\rho(r), S^2, q, \tau)dr \qquad (2\text{-}36)$$

This approach integrates a variety of semi-local parameters to derive an approximation for the exchange-correlation energy per particle, enhancing the functional's adherence to physical and mathematical constraints.

2.6.6 TPSS

The meta GGA TPSS (Tao, Perdew, Staroverov, and Scuseria), a non-empirical exchange-correlation functional, integrates several elements [126]. By merging TPSS with exact exchange, a global hybrid version is formulated:

$$E_{\{xc\}}^{\{TPSSh\}} = (1 - a_0)E_{\{xc\}}^{\{TPSS\}} + a_0 E_{\{x\}}^{\{HF\}} \qquad (2\text{-}37)$$

In this equation, the coefficient (a_0), fine-tuned to 0.10, is calibrated by minimizing the mean absolute deviation of the formation enthalpies for a set of 223 G3/99 molecules [127]. This hybrid, TPSSh, maintains the exact constraints found in the original TPSS functional.

Characteristics of these functionals include:

- The TPSS correlation part is designed to mitigate the issue of spurious self-interaction errors (SIE), although the exchange part doesn't fully resolve SIE. Nevertheless, TPSS marks an advancement over prior functionals [127].
- Compared to the B88 exchange and the OPTX GGA, the TPSS exchange functional is more closely aligned with the Lieb-Oxford limit (1.679), enhancing its accuracy in this aspect [128].
- The relatively low value of (a_0) in TPSSh (0.10), when contrasted with typical GGA hybrids, indicates that the TPSS meta-GGA offers a more refined exchange functional compared to other GGA functionals [129].

2.7 DFT + U:

In a system where many electrons are strongly correlated i.e. a system in which electrons are present in close proximity such as that in d or f orbital, LDA and GGA suffer a great below due to self-interaction error. This self-interaction error arises because of the fact that the electrons of a strongly correlated system interact with themselves to a much greater extent. Due to this, LDA and GGA fail to accurately predict the energy of such systems [130].

To overcome this error, DFT methods such as DFT+U or DFT+dynamical mean field theory (DMFT) can be used which explicitly take into account these correlation effects [131]. These methods allow for more accurate predictions of energies and other properties in strongly correlated systems by taking into account the electron-electron interactions.

DFT+U is a method of DFT that incorporates the effect of strong electron correlations by adding an additional Hubbard-type potential to the exchange-correlation function. This U

parameter can be added to local as well as semi local functionals giving LDA + U and GG + U. This potential is parametrized by two parameters, U and J, which can be adjusted to account for the effects of local Coulomb interactions. The advantage of this method is that it can accurately account for the effects of strong electron correlations without introducing any additional approximations. This makes this method particularly useful in systems where strong electron correlations are important, such as those with d or f orbitals [132]. If exchange interaction is represented by J and on-site Coulomb interaction by U, then the additional parameter to DFT is given by [133]:

$$\frac{U-J}{2}\sum_{\sigma,m}(n_{l,m,s}-n_{l,m,s}^{2}) \qquad (2\text{-}38)$$

The LDA+U technique is widely adopted to refine the estimations made by the DFT exchange correlation functional. While it operates on principles similar to the conventional LDA approach for valence electrons, it incorporates the Hubbard model to achieve a more accurate depiction of strongly correlated electron states, notably in d and f orbitals. As a result, the system's total energy (E_{LDA+U}) typically combines the standard LDA energy functional (E_{Hub}) for all states with the Hubbard functional energy, which addresses the correlated states. The integration of the Hubbard term introduces a double counting error for these correlated states [134-139]. Thus, to precisely reflect the electronic interactions within a mean field approximation, a correction for this "double-counting" error (E_{dc}) needs to be deducted from the LDA's total energy.

$$E_{LDA}+U[\rho(r)]=E_{LDA}[\rho(r)]+E_{Hub}[\{n_{mm}^{I\sigma}\}]-E_{dc}[n^{I\sigma}] \qquad 2\text{-}39)$$

The dc functional lacks a unique definition, which remains a contentious and unresolved aspect of LDA+U. Various formulations of this functional have been developed and

applied under different conditions. The two predominant variants of the dc term have resulted in what are known as the "around mean-field" (AMF) and "fully localized limit" (FLL) versions of the LDA+U method, each with its own set of implementations and studies supporting them. According to the FLL version of LDA+U, the equation (2-39) can be rewritten as follows

$$E_{LDA} + U[\rho(r)] \qquad \text{2-40)}$$
$$= E_{LDA}[\rho(r)] + \sum_{l}\left[\frac{U^l}{2}\sum_{m,\sigma\neq m',\sigma'} n_m^{l\sigma} n_{m'}^{l\sigma'} - \frac{U^l}{2}n^l(n^l-1)\right]$$

$n_m^{l\sigma}$ represents the localized orbital's occupation numbers, l is the atomic site index, and the spin is represented by σ.

2.8 Van der Waals Corrections

Van der Waals interactions, although considered the weakest among weak chemical forces (with a strength typically ranging between 0.4 and 4 kJ/mol), are crucial in various fields such as physisorption, structural biology, polymer science, and the study of crystal structures. However, these interactions cannot be accurately described by traditional GGA or LDA exchange-correlation functionals used in DFT as no factor for dispersion forces is included in the basic formula for both LDA and GGA. [140]. The GGA approaches often lead to repulsive potential curves lacking a minimum, while the LDA methods usually result in an overestimation of binding for rare-gas diatomic molecules [141, 142]. The van der Waals (vdW) interaction stems from quantum-mechanical effects due to the interactions between transient fluctuating dipoles, occurring even among two

neutral atoms without any overlap in electron density. The prevailing exchange and correlation functionals, which are built on the principles of local density, its gradient, and local kinetic-energy density, fall short in precisely capturing the vdW energy contributions [141, 142].

This limitation arises due to the long-range nature of van der Waals interactions, which exhibit a characteristic correlation on electron energies that diminishes rapidly with increasing distance between interacting molecules.[143] Van der Waals interactions become too weak to be observed when the distance between interacting molecules exceeds 0.6 nanometers. Additionally, it's important to note that van der Waals forces are anisotropic, meaning they vary in strength and direction depending on molecular orientations. This anisotropy is a significant feature, except in cases where the interacting molecules are both noble gas atoms. To address this, one of the main approaches involves correcting DFT energy by incorporating empirical two-body or multi-body corrections. Commonly used methods for this purpose include D2 and D3 corrections. [144] These corrections are empirical in nature, meaning they are based on experimental observations and are not derived from fundamental principles. The D2 and D3 corrections are designed to account for the missing van der Waals interactions in standard DFT calculations, thereby improving the accuracy of the results. These corrections take into consideration both two-body (pairwise) and multi-body interactions that contribute to van der Waals forces. The D2 correction is given as follows [145]

$$E_{vdW}^{D2} = -S_6 \sum_{i=1}^{N-1} \sum_{j>i}^{N} \frac{C_{6,ij}}{R_{ij}^6} f_d(R_{ij}) \qquad (2\text{-}41)$$

Here N represents the number of atoms, S_6 is the notation for scaling factor, the number of interacting atoms are represented by i and j, $C_{6,ij}$ is the dispersion coefficient, R_{ij} the

distance between the two interacting atoms i and j and $f_d(R_{ij})$ is the damping function which is represented as follows

$$f_d(R_{ij}) = \frac{1}{1 + e^{-d\left(\frac{R_{ij}}{R_r - 1}\right)}} \qquad (2\text{-}42)$$

Here, R_r is the sum of Van Der Waals Radii between the atoms.

DFT-D3, or Density Functional Theory Dispersion correction version 3, is an improved and refined version of DFT-D2. This method is designed for applications involving the first 94 elements of the periodic table. In contrast to DFT-D2, DFT-D3 treats main-group elements and transition metals equally. The significant advancement in DFT-D3 lies in the flexibility of its dispersion coefficients. In DFT-D3, the dispersion coefficients are fully flexible and system-dependent. This means that the method can adapt to the specific characteristics of a given molecular system, providing a more accurate and versatile description of dispersion forces.[146]

The general form of D3 function is given by

$$E_{vdW}^{D3} = \sum_{ij} \sum_{n=6,8} S_n \frac{C_n^{ij}}{r_{ij}^n} f_{d,n}(r_{ij}) \qquad (2\text{-}43)$$

The second approach to calculate vdW interactions in DFT involves correcting the exchange-correlation energy (Exc) with a non-local VDW density functional. In this method, the non-local dispersion energy (E_c^{nl}) is calculated using the DFT charge density iteratively until self-consistency is achieved.[147] The expression for the total exchange-correlation energy (Exc) in this approach is given as follows:

$$E_{\{xc\}} = E_x^{\{GGA\}} + E_c^{\{LDA\}} + E_c^{nl} \qquad (2\text{-}44)$$

Here, $E_x^{\{GGA\}}$ represents the GGA exchange energy term, $E_c^{\{LDA\}}$ represents the LDA correlation energy term, and E_c^{nl} represents the non-local dispersion energy term and can be expressed as follows

$$E_c^{nl} = \int \int \rho(r_1)\phi(\mathrm{r}_1, r_2)\rho(r_2)d^3r_1 d^3r_2 \qquad (2\text{-}45)$$

Here $\phi(r_1, r_2)$ represents electron density function for atoms that are far apart. But this method asks for heavy computational load compared to the method described earlier. Several types of DFT-D3 variations are there differing in type of damping function. Zero damping variation also known as the Grimme's formulation involves the use of following damping function:

$$E_{DFT-D3} = E_{KS-DFT} + E_{D3\ (2\ body\ system)} + E_{ATM(3\ body\ system)}$$

$$f_{d,n}^{D3(0)}(R_{ij}) = \left[1 + 6\left(\frac{R_{ij}}{S_{r,n}R_{0,ij}}\right)\right] \qquad 2\text{-}46)$$

In order to include van der Waals (vdW) corrections, the spin-polarised PBE combined with the Becke-Johnson (BJ) damping function in Grimme's technique is used in this thesis. The D3(BJ) damping function is given as [148]:

$$f_{d,n}^{D3(BJ)}(R_{ij}) = \frac{R_{ij}^n}{R_{ij}^n + \left(\alpha_1 R_{0,ij} + \alpha_2\right)^n} \qquad 2\text{-}47)$$

This DFT-D3(BJ) approach was further re-parameterized to form DFT-D3M(BJ) approach, with parameterizing relying on non-equilibrium geometries [149].

This is done because it can accurately predict the adsorption and binding energies of metal oxide materials. It is discovered that adding vdW interactions can change the sequence in which different isomers are stable and cause important changes to the adsorption energies.

Additionally, the adsorption characteristics will affect the adsorbates' diffusion and reaction characteristics on AQC/oxide surfaces. In order to accurately forecast the polaronic states and band gap values of TiO_2, the generalized-gradient approximation (GGA) + Hubbard term (U-term) is used because the self-interaction inaccuracy leading to false electron delocalization in the usual DFT techniques. Copper (4s) orbital U value is 5.2 eV, whereas titanium (3d) orbital U value is 4.2 eV.

The HSE06 functional is particularly suitable for systems where precise electronic structure details are crucial, such as the sub-nanometer atomic quantum clusters (AQCs) studied in this work. By employing HSE06, the calculations can better account for the electronic interactions and quantum effects that are significant in these small-scale systems. This leads to more reliable predictions of their catalytic, photocatalytic, and other functional properties.

3 Computational Method

3.1 VASP

This chapter is aimed at introducing the VASP software which is the key agent behind all the structural optimizations and calculations performed in this thesis. Encoded in FORTRAN language, Vienna Ab Initio Simulation Package (VASP) is a computer program that finds a solution to the Schrodinger wave equation for a many-body system by solving Kohn-Sham equations within the skeleton of Density Functional Theory or Hartree Fock Approximation [150-152]. Through VASP, molecular modeling e.g., geometric optimization, electronic structure calculations, etc., and Molecular Dynamics using an ab initio approach can be performed. There are a lot of input and output file types used in VASP which are as follows:

3.1.1 VASP input files

There are four different files that are required for VASP as input. They are as follows:

POSCAR file

All the information about the locations of ions, and lattice geometry is contained within the POSCAR file. Different lines as shown in this file are specified to represent certain specific data. The first line represents the comment line that may contain the topic name

for which calculations are performed. The next line represents all the data about lattice scaling and atomic coordinates. The unit cell is represented by the third, fourth, and fifth lines by three lattice vectors. The next line i.e., the sixth line contains symbols for all the chemical species of the system. The number of these chemical species is represented in the seventh line. The eighth line represents the data about coordinates. It may or may not contain "Selective Dynamics". In the presence of "selective Dynamics", the next lines contain the atomic coordinates with T and F flags, T representing a change in coordinates for optimization whereas f represents no change in coordinates. The absence of selective dynamics shows that all the atomic species will alter their coordinates during optimization. This eighth line also gives information about the type of coordinate system (whether Cartesian or direct).

POTCAR file

This file contains the data about the pseudopotential of all the chemical species for which the entire calculations are performed. If there is more than one species for which the calculations are performed, then the POTCAR file should be a combined POTCAR file containing pseudopotentials of all the chemical species. The "cat" command can be used to obtain a combined POTCAR file for fulfilling this demand. Moreover, The order in which all the chemical species appear in the POTCAR file should be analogous to the order of chemical species followed in the sixth line of the POSCAR file.

INCAR file

This is the main input file of VASP as it directs the program to perform required tasks. It consists of all the keywords for carrying out the calculations. For example,

GGA=PE refers to the calculations carried out by Generalized Gradient Approximation with the pseudopotentials of Perdew, Burke, and Ernzerhof.

ISPIN=2 refers to the calculations involving spin-polarization

KPOINT file

This file contains all the weights of k-points along with their coordinates. It consists of several lines, each representing a specific component. The first line refers to the comment line that may contain the title of the work. The second line contains all the k-points. The third line indicates the type of coordinates revealing whether reciprocal coordinates or cartesian coordinates are used. The next three lines represent the coordinates for all the k-points and their weights. The third line from the top represents the method adopted. If the method adopted is the tetrahedron method, then there is a seventh line known as the control line that may start with T or t, followed by 2 more lines. The number of tetrahedra along with their volume weight is shown in the seventh line whereas the last eighth line contains the weight with four corner points. In case of the absence of the tetrahedron method, the KPOINT file ends on the sixth line.

3.1.2 VASP Output files

There are three output files of VASP

OUTCAR file

This is the core output file containing all the data for calculations. It comprises information from several sources; analysis of symmetry, data from three input files i.e., POSCAR, POTCAR, and INCAR; keywords from the INCAR file; data on the basis set, the k-points, and the ionic positions; complete information about all the electronic steps taken in optimization; information about the charge, energy, and timing.

OSZICAR file

This file is a simpler version of the OUTCAR file containing the details about every electronic step. This file presents the information in a much-simplified form so that the calculations e.g., the total energy, energy change, etc. can easily be read.

CONTCAR file

This file`s format is analogous to the POSCAR file and contains the direct coordinates for locations of ions and lattice geometry. In the case of static calculations, CONTCAR is identical to POSCAR.

3.2 VASPKIT

VASP is a sophisticated program designed for simulating materials using the density functional theory (DFT) approach. To efficiently perform complex calculations and analyze the results of the VASP code, scientists use a tool kit called VASPKit. This open-source software package provides a potent and user-friendly interface for performing pre- and post-processing calculations and analysis on the data obtained through VASP. VASPKit allows users to calculate optical, electronic, elastic, and catalytic properties. Moreover, it can also be used to obtain carrier effective masses, elastic constants, equation of state, fermi surface, band structure, joint density of states, linear optical coefficients, etc. VASPKit can be divided into two modules, the pre- and post-processing module.

The preprocessing capabilities of VASPKit include all activities performed before carrying out Density Functional Theory calculations through VASP. This program accesses the POSCAR document and then prepares POTCAR, INCAR, and KPOINTS as input files for performing VASP calculations. The structure data from the POSCAR file can be edited to build heterojunction and supercell, generate k-paths of bulk and 2D materials to calculate their band structure, determine molecular and crystal symmetry, or find the primitive/conventional cell by the application of spglib, a symmetry analysis

library[153]. Moreover, the POSCAR file can be converted to other formats, e.g., Protein Data Bank (.pdb) [154], Crystallographic Information Work (.cif) [155], and XCrysDen (.xsf) [145].

In the post-processing module, raw data from the VASP code is extracted and analyzed. Using this extracted data, several properties are calculated, including electronic, optical, magnetic, and mechanical properties, etc.

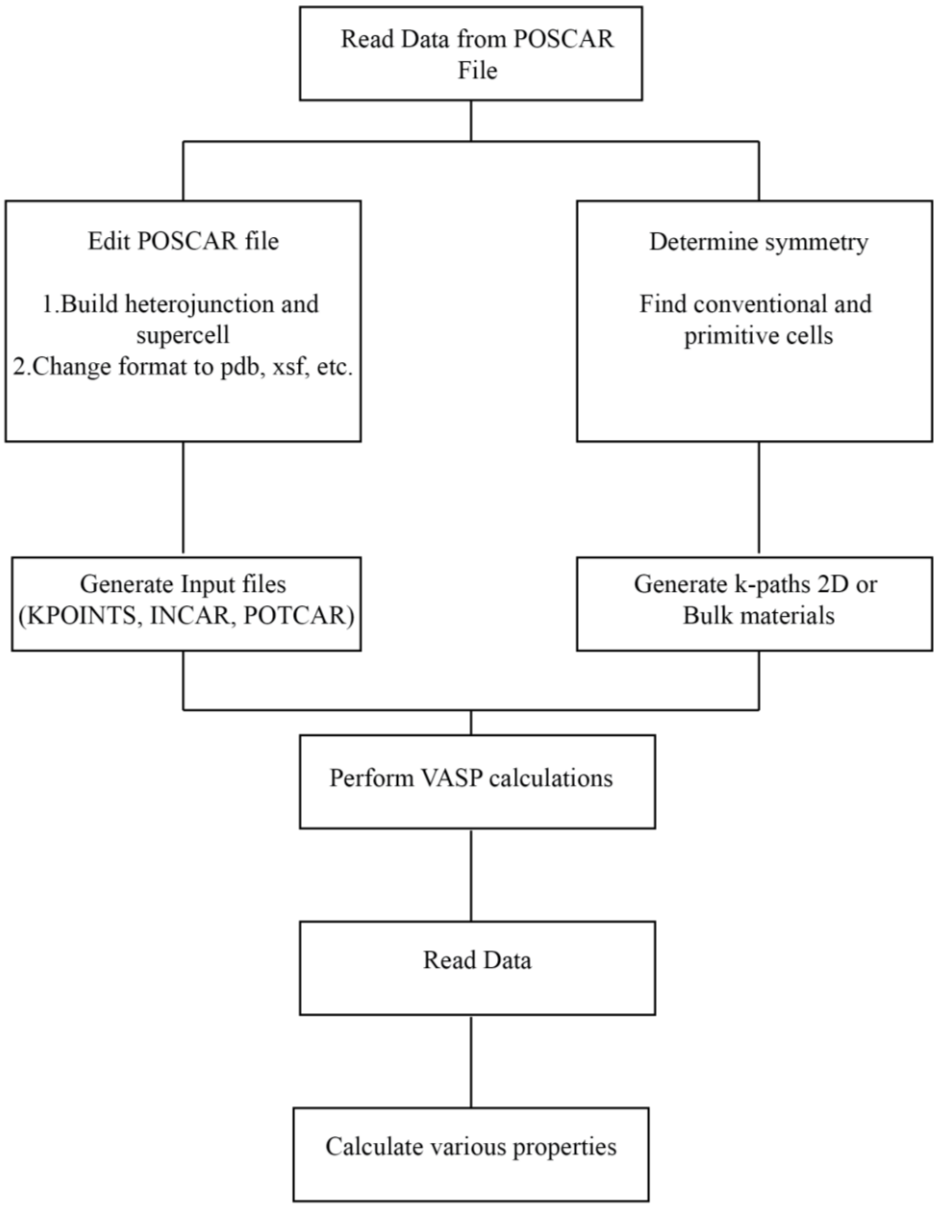

Figure 7 the preprocessing capabilities of VASPKit

3.3 Implementation of DFT in VASP

There are different computational software packages that use the principles of theoretical chemistry and physics to assess different molecules, and atoms to understand their properties and structures. In this context, Kresse et al. have pioneered the development of VASP, a sophisticated computer software exclusively designed for atomic-scale materials

modeling [156-159]. It can perform intricate quantum-mechanical molecular dynamics simulations as well as electronic structure calculations. Furthermore, VASP emerges as a prominent tool for investigating interactions occurring on as well as within metal oxide substrates. For performing calculations, VASP employs the plane waves with project augmented pseudopotential in a periodic system (PPW-PP) [160, 161].

This thesis employs the concept of PPW-PP to encapsulate both the wave function of valence electrons and the stationary wave function nodes associated with the core electrons during the optimization process. This strategy effectively limits the plane wave number employed in simulating the system. Throughout this study, a cutoff energy of 500 eV has been consistently applied to these plane waves. VASP utilizes a matrix diagonalization technique, combined with the Broyden mixing method, to effectively solve the self-consistent Kohn Sham ground-state equations, thereby ensuring convergence in calculations [162]. The DFT implementation employed in this study is of the GGA type, utilizing the PBE functional. The self-consistency procedure can be summarized as a three-step process. Initially, the Hamiltonian is constructed based on the charge density. Next, iterative calculations of the wave functions are performed until an approximation closely resembling the exact wave functions of the Hamiltonian is achieved. Finally, an optimized wave function generates a new charge density, which is merged with the input charge density using the Broyden mixing technique. The self-consistency scheme employed in this thesis is given in the figure below

3.4 Periodic Boundary Conditions

The sum total of all the particles, including electrons and nuclei, in a solid, is the multiple of 6.02×10^{23} i.e. Avogadro`s number. To perform DFT calculations, one has to extend

one-electron wave function over the entire system because each electron of the solid spreads throughout the system, thus the basis set required for the extension of KS orbitals should be infinite. A crystalline structure has a periodic arrangement of nuclei and electrons repeating in a regular manner and for such an infinite system, the structure is considered to be homogenous in every direction. Thus, for the approximation of this large solid, we introduce periodic boundary conditions (PBCs) by considering a periodically repeating unit cell called a supercell extending in 3 dimensions throughout the system[163].

Bloch`s theorem (put forward by Swiss scientist Felix Bloch), states that while solving the Schrodinger wave equation in periodic potential presence, the energy eigenfunction is taken as the product of plane wave function and periodic function having periodicity identical to that of potential`s [157].

$$\phi_{n\vec{k}}(\vec{r}) = e^{\iota\vec{k}.\vec{r}} u_{n\vec{k}}(\vec{r}) \qquad (3\text{-}1)$$

Here, r represents the position, ϕ represents the wave function, u represents the periodic function, $\vec{k}$ is the wave vector called crystal momentum vector, e represents the Euller`s number and ι is iota, or imaginary unit. For a vector $\overrightarrow{R_e}$ of the crystal lattice, we know that $u_{n\vec{k}}$ is invariable translationally, so we can write:

$$u_{n\vec{k}}(\vec{r}) = u_{n\vec{k}}\left(\vec{r} + \overrightarrow{R_e}\right) \qquad (3\text{-}2)$$

This eigenstate is called the Bloch function, represented by $\phi_{n\vec{k}}$, transforms under translation by the vector R_e as follows:

$$T_{vec\overrightarrow{R_e}}\phi_{n\vec{k}}(\vec{r}) = \phi_{n\vec{k}}\left(\vec{r} + \overrightarrow{R_e}\right) = e^{\iota\vec{k}.\overrightarrow{R_e}} u_{n\vec{k}}(\vec{r}) \qquad (3\text{-}3)$$

Since we are considering PBC, the eigenvalues and their eigenstates $\phi_{n\vec{k}}$ are periodic in $\vec{k}$-Space.

$$\phi_{n,\vec{k}+\vec{K}}(\vec{r}) = \phi_{n\vec{k}}(\vec{r})E_{n,\vec{k}+\vec{K}}(\vec{r}) = E_{n\vec{k}}(\vec{r}) \quad (3\text{-}4)$$

The reciprocal lattice vector is represented by the symbol $\vec{K}$ in this equation is arbitrary.

It is adequate to focus on the Bloch functions and corresponding eigenvalues of a system in the first Brillouin zone. Furthermore, by substituting the value of Bloch functions into the Kohn-Sham equation for a given value of $\vec{k}$, a set of eigen equations can be obtained making computational calculations much more acceptable. Since electronic wave functions at $\vec{k}$ points in close proximity yield similar results, it is only necessary to calculate a finite number of $\vec{k}$ points within a small region of the reciprocal lattice to determine the total energy of a solid. This reduces the computational workload significantly.

3.5 Geometry Optimization

When the energy of a system is minimized, geometry optimization finds the local energy minimum on the potential energy surface, which results in the most stable configuration for the system. Certain material properties, including defect thermodynamics or electrical structures, may be dramatically impacted if geometry optimization is not carried out. A conjugate-gradient algorithm (CGA) [160, 161]is used to detect ion motion and optimize modeled systems. In this thesis, the CGA is implemented by including the tag (IBRION=2) in the input file for VASP. The CGA is a three-stage process with initial, trial, and corrector stages that involve assessing the steepest drop. Based on computed energies and forces, the steepest descent is identified in the initial step, and the ions' locations are modified accordingly. The following stages of this procedure are continued until a configuration with the least amount of energy is obtained or the desired cut-off is

reached. A fresh gradient is examined after the first stage, and then additional stages are evaluated.

To accommodate the huge supercell used in the tetrahedron technique and ensure accurate band occupation, a Gaussian spreading value is applied by setting the (ISMEAR=0) tag. Additionally, a small smearing width is specified using the (SIGMA=0.05 eV) tag. The (EDIFF=10^{-4} eV) tag is used to calculate a convergence threshold value for the self-consistent minimization method. Furthermore, a threshold force value set by the (EDIFFG=0.02 eV/ Å) is used to allow relaxation of all modeled structures.

Since all the systems in this thesis have huge sizes and tiny reciprocal space, the k-point mesh is sampled using the Monkhorst-Pack scheme[162, 164], and a -centered mesh is employed throughout the simulations. Therefore, it is possible to precisely assess the variation throughout the Brillouin zone using a modest k-point mesh. It is permissible to describe the electronic structures of insulators and semiconductors using a single value of k-point.

Similar to other transition metal oxides, TiO_2 exhibits deviations in density functional theory (DFT) calculations due to its strong correlation effects. As discussed earlier in section 2.7, it is crucial to incorporate the U-term in the calculations to obtain precise electronic structure outcomes. In this thesis, a U value of 4.2 eV is applied to the Ti 3d orbital, which was initially reported by Morgan and Watson[165-167]. At this value, the band gap values are closely comparable to the experimentally measured values for rutile TiO2 [168].

3.6 Plane Wave Basis Set

A basis set refers to a collection of functions, known as basis functions, employed to represent the electronic wave function in DFT. This representation involves changing the

model's partial differential equations into algebraic equations compatible with working efficiently on a computer. These basis sets can be a group of any mathematical functions [169]. The basis set can be comprised of atomic orbitals, a popular choice within the quantum chemistry field, where the method of combining atomic orbitals in a linear manner is employed. Alternatively, it may be constituted by plane waves, a common preference in the solid-state community. Furthermore, Guassian, Slater, or numerical atomic orbitals can be used [170].

One of the remarkable benefits of utilizing plane waves is their completeness in mathematical terms, as well as their simplicity in computational handling. To solve the Kohn Sham equations, an essential step is to expand the Kohn Sham orbitals by employing a specific basis set. Therefore, it becomes crucial to determine an appropriate basis set that can accurately represent the KS orbitals. Various options for basis sets are available each with its own benefits and drawbacks [171-173].

Usually, when choosing the basis set of plane waves, it is customary to utilize an energy cut-off. The cut-off energy for the plane waves is set to 500 eV for all modeled systems in this thesis. The plane waves that satisfy the energy threshold within the simulation cell are subsequently included in the computational process. Furthermore, these basis sets are extensively utilized in 3D periodic boundary conditions.

The primary benefit of employing a plane-wave basis is its assured smooth and monotonous convergence towards the desired wavefunction [174]. In contrast, the utilization of localized basis sets may pose challenges in achieving a monotonous convergence due to issues related to over-completeness. In the case of a large basis set, functions associated with different atoms become increasingly similar, and numerous eigenvalues associated with the overlap matrix tend to fall towards zero.

In systems where, periodic boundary conditions can be applied, utilizing a plane wave (PW) basis set is a preferable choice due to its efficiency in reciprocal space representation. This is because plane waves are precise eigenfunctions of the uniform electron gas. The use of a plane wave basis set comes with an advantage i.e., it can be used for any type of atom or for any position. Additionally, via the fast Fourier transform (FFT), PW can be conveniently transformed from real space to reciprocal space. These sets are comprised of basic mathematical functions in the form of plane waves, which form comprehensive basis sets. The extent of completeness can be easily controlled by modifying the cut-off kinetic energy. The self-consistent procedure used in this thesis is presented in **Figure 8.**

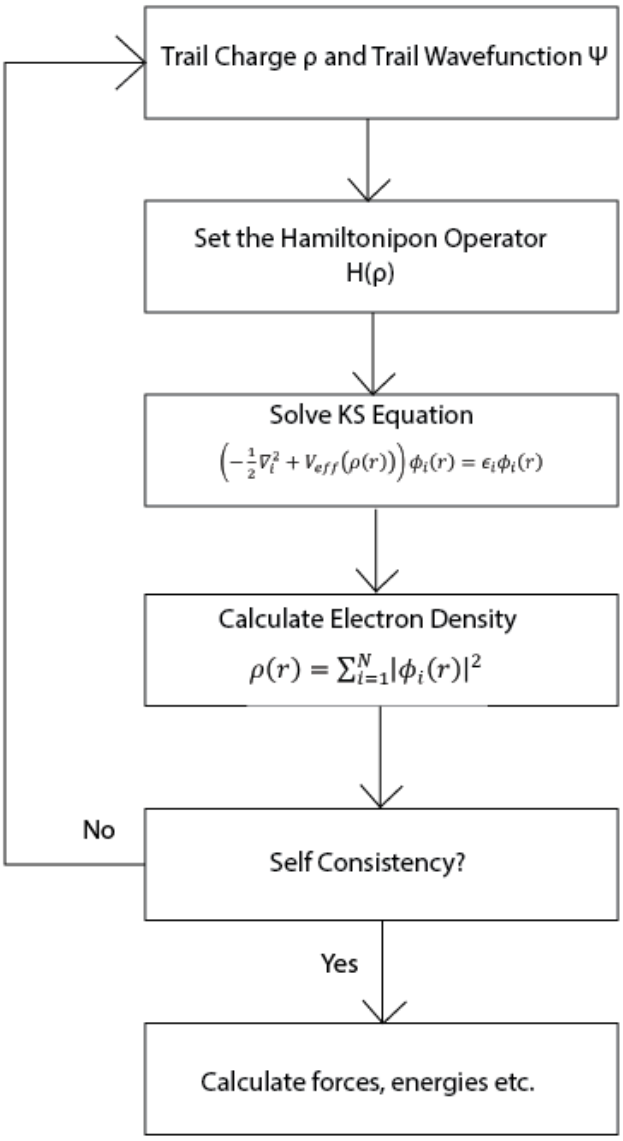

Figure 8 Self-consistent procedure used in this thesis.

3.7 PAW-PP (Pseudopotential)

One of the main disadvantages of utilizing the plane-wave technique in Density Functional Theory (DFT) calculations is the need for a high number of plane-waves, typically exceeding 10,000, to accurately capture the quick variations of the wave function within the core region. This can result in a significant increase in the

computational cost required to perform and analyze calculations for electronic structures. It is important to note that in most cases, the physical and chemical properties of molecules and solids rely primarily on the behavior of their valence electrons, with the contribution of core electrons being completely negligible.

As a result, in order to significantly speed up calculations, the all-electron problem can be simplified by treating it as a problem involving valence-electron only and using pseudopotentials (PSPs) which are actually weaker nuclear potentials. The pseudopotential technique is crucial in achieving this, as it replaces the core potential with a weaker pseudopotential [175-178].

The innermost electrons, also known as core electrons, reside in close proximity to the atomic nucleus and are strongly attracted to it. Consequently, they exhibit a high degree of localization. On the other hand, valence electrons occupy positions much farther from the nucleus and experience relatively weaker attraction. As a result, they are considered to be more delocalized. To comprehensively account for the involvement of every electron, it is necessary to broaden their wavefunctions using plane wave basis sets. This expansion of the fundamental wavefunctions demands a substantial quantity of plane waves. The swift fluctuations exhibited by the valence states in the central zone, stemming from their orthogonality with the core electrons, necessitate an increased number of plane waves possessing higher kinetic energy. Numerous characteristics of a substance are influenced by how the atoms are connected to their nearby atoms. The bonding primarily involves the participation of valence electrons, enabling us to approximate the interaction of core electrons and ionic potentials using a pseudopotential. This pseudopotential operates on a collection of pseudo wave functions instead of the actual valence wavefunctions. Consequently, there is no need for a high energy cut-off in

the plane wave expansion. By utilizing fewer plane waves, we can construct the Kohn Sham orbitals and significantly decrease the computational expenses involved.

The pseudopotential and pseudo wavefunction must exhibit complete similarity to the all-electron counterpart beyond the specified cut-off radius. A visual representation of these criteria is depicted in the figure. By employing the pseudopotential approximation, solely the valence electrons residing outside the cut-off radius are explicitly taken into account. Within the core region, the pseudo-wave functions lack nodes. To avoid any kind of overlap among the adjacent atoms of the core region, it is crucial to select an appropriate cut-off radius, represented by r_c.

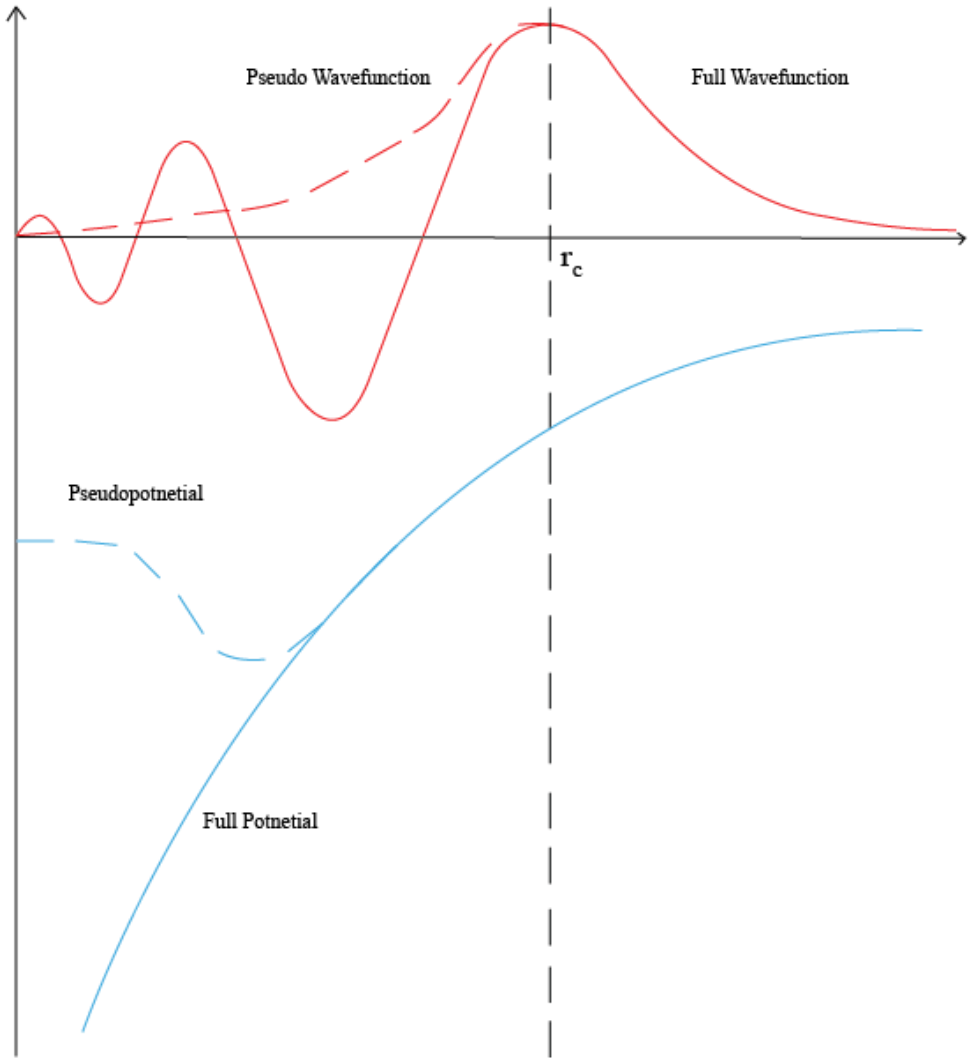

Figure 9-Pseudowavefunction is represented by a dashed red line and full wavefunction by a solid red line whereas pseudopotential is represented by a dashed blue line and full potential by a solid blue line. They are plotted against the distance r from the nucleus [179].

In simpler terms, using pseudopotentials has the advantage that complicated wave functions can be substituted with easier ones, while still retaining the system's essential

properties and significantly reducing computational costs [180]. It is worth noting that the Ag (4d and 5s), Ce (4f and 5d), Ti (3s, 4s, 3p, and 3d), Si (3s and 3p), O (2s and 2p), and H (1s) atomic orbitals are considered to be valence electrons.

Another approach to Pseudopotential as an alternative technique is Blöchl's projector augmented wave (PAW) approach which offers a more refined means of producing wave functions in the vicinity of atomic centers [161]. This technique involves the use of auxiliary localized functions, similar to the "ultrasoft" pseudopotential approach, making it similar to pseudopotential calculations in many aspects. However, the PAW method stands out by transforming the rapidly fluctuating valence wave functions of single particles, which are close to the nucleus, into several smooth auxiliary functions. This transformation is the core characteristic of the PAW formalism.

Overall, the PAW method is designed to improve the accuracy of quantum mechanical calculations, particularly in regions close to the atomic nuclei. By using auxiliary functions, the PAW technique can overcome the limitations of PSPs, which often fail to capture the subtle electronic interactions in these regions. The smoother wave functions produced by PAW can provide a better representation of the electronic structure, leading to more accurate results in various applications, such as in materials science and solid-state physics. The PAW technique is an exceptional approach to ascertaining the electronic structure of materials. It stands out from other methods as it accurately characterizes the nodal behavior of the valence-electron wave function. Furthermore, it enables the integration of upper core states into the self-consistent iteration process. This remarkable feature distinguishes it from other existing methods [181, 182].

If Ψ represents the valence wave function fluctuating at a fast rate in the vicinity of the nucleus, and $\tilde{\Psi}$ represents several smooth auxiliary functions, then they can be interconverted as follows:

$$\Psi = T\tilde{\Psi} \tag{3-5}$$

And here,

$$\mathrm{T} = \mathrm{I} + \mathrm{T_o} \tag{3-6}$$

Furthermore, T_o can be expanded as:

$$\mathrm{T_o} = \mathrm{I} + \sum_{\mathrm{R}} \mathrm{S_R} \tag{3-7}$$

R represents the nonoverlapping sphere in the vicinity of the nucleus. The formula for the real wave function involves non-overlapping spheres arranged around the atoms. In order to derive this formula, both the real and auxiliary wave functions are expressed as combinations of plane waves within these spheres (denoted as R) in a linear manner as [161]:

$$|\Psi\rangle = |\tilde{\Psi}\rangle + \sum_{n} C_n\{\langle\Psi| - |\tilde{\Psi}\rangle \tag{3-8}$$

Incorporating projector functions $|P_n\rangle$ into the equation gives us [161] :

$$|\Psi\rangle = |\tilde{\Psi}\rangle + \sum_{\mathrm{n}} \{\langle\Psi| - |\tilde{\Psi}\rangle\} \langle \mathrm{P_n}|\tilde{\Psi}\rangle \tag{3-9}$$

$$\mathrm{T} = \mathrm{I} + \sum_{\mathrm{n}} \{\langle\Psi| - |\tilde{\Psi}\rangle\} \langle \mathrm{P_n}| \tag{3-10}$$

To calculate the operator's expectation value, we can write:

$$\langle \mathrm{A} \rangle = \sum_{\mathrm{n}} \mathrm{C_n}\{\langle \Psi_\mathrm{n}|\mathrm{T} + \mathrm{AT}|\tilde{\Psi}_\mathrm{n}\rangle \tag{3-11}$$

The Final expression for the energy can be written as:

$$E = \widetilde{E} + \sum_{R} E_R^1 - \widetilde{E_R^1} \qquad (3\text{-}12)$$

In conclusion, this section highlights the superiority of the PAW (Projector Augmented-Wave) method compared to the PSPs (Pseudopotentials) technique in terms of the PSPs' transferability and the accuracy it offers in electronic structures evaluation for various systems.

3.8 Bader Charge Analysis

The calculations conducted in this thesis employ DFT to obtain charge densities. Bader charge analysis is a useful tool for understanding the electronic structure of molecules and solids, and it plays a significant role in theoretical and computational chemistry[183]. The concept behind atomic charges is commonly utilized to investigate and explain reactivity and structural variations. Bader's approach is recognized as one of the most rigorous methods for calculating charges on individual atoms [184, 185]. Bader charge analysis is a technique employed to comprehend the distribution of electrical charges within molecules or solids. This method is founded upon the findings of Richard Bader, who proposed a theory delineating the division of molecules into distinct entities known as atoms. To accomplish this division, special surfaces are employed, referred to as zero-flux surfaces, where the electric charge reaches its minimum point perpendicular to surface. These surfaces are typically situated between atoms and are influenced by the specific elements present. The zero-flux surfaces serve as boundaries, demarcating the atoms and defining the spatial occupation of each atom, which is termed the Bader volume. When investigating the dispersion of electric charges, the focus lies on the charge present within Bader volume of each atom. This charge is employed as an estimation of

the overall charge magnitude of the atom. The Bader charge analysis relies on determining the lowest energy state. It involves calculating the charge of each atom by making a comparison with an atom's valence electrons. In this approach, the positive charge represents electron loss to the atoms in its surrounding, while a negative charge represents electron gain.

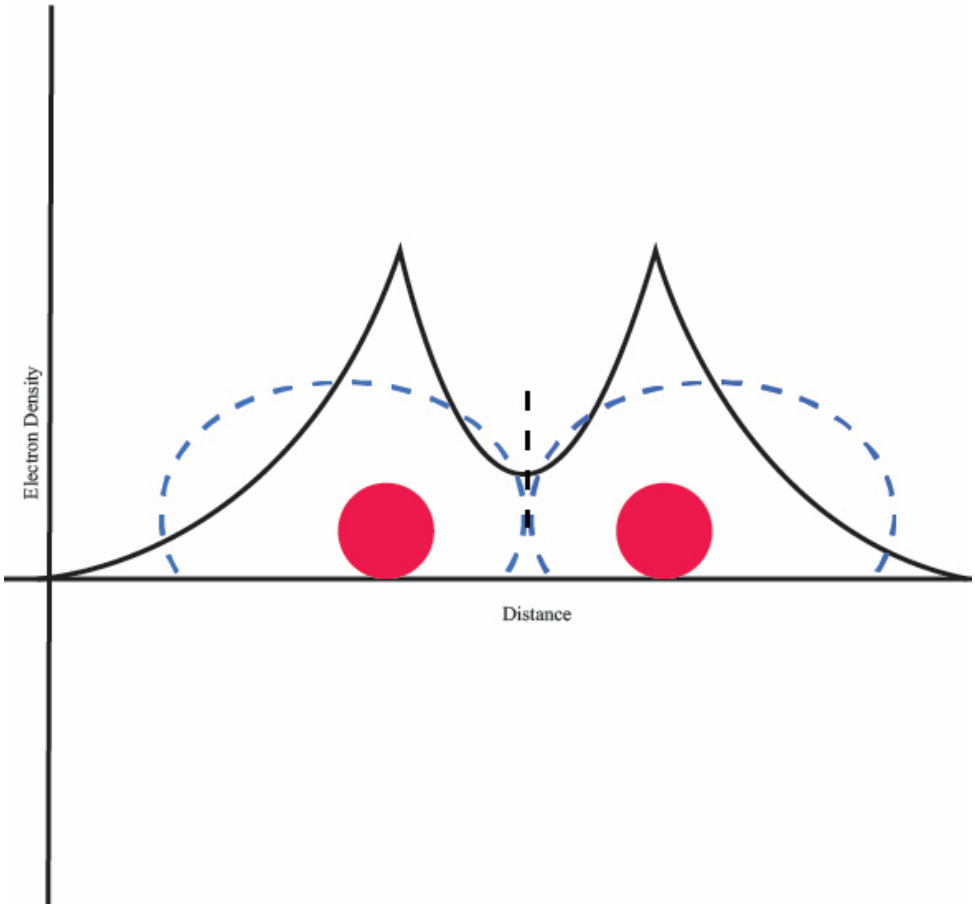

Figure 10 The image portrays the Bader charge analysis of a pair of atoms (red). The electron density variation is represented by the continuous black line. The dashed black line represents zero flux and the dashed blue circle represents the Bader volume of each atom [186]

In this approach, we can examine the electron distribution of a system generated by plane wave calculations by analyzing the electron density, denoted as $\rho(x, y, z)$, which depends

on three spatial coordinates. The nuclei within the system act as concentrated attractive forces surrounded by an electronic cloud. Specifically, the charge density function reaches its highest value at the nuclei positions and gradually diminishes as we move farther away from these points.

Henkelman et al. developed a fast and efficient method for analyzing the distribution of electrons in a molecule or material [187-189]. This method is known as the Bader decomposition of electron density. The technique utilizes a grid-based algorithmic approach, where the electron density is evaluated at discrete points on a three-dimensional grid. In their approach, the researchers use the steepest ascent trajectories that are restricted to the grid points. These trajectories are employed to identify and define the regions in space called Bader regions. The Bader region is a localized region around an atom or a group of atoms where the electron density is concentrated. To perform the Bader decomposition, the algorithm starts from a specific grid point on the density grid, denoted by its coordinates (i, j, k). From this starting point, a trajectory is traced along the direction that maximizes the charge density gradient, which is a measure of how rapidly the electron density changes. Specifically, the gradient is computed along the r using a formula that captures the change in charge density at each grid point, given as follows

$$\nabla\rho(\mathrm{i},\mathrm{j},\mathrm{k}).\hat{\mathrm{r}}(\mathrm{di},\mathrm{dj},\mathrm{dk}) = \frac{\Delta\rho}{|\Delta\vec{\mathrm{r}}|} \tag{3-13}$$

The value of $\Delta\rho$ in x, y, and z direction is given as:

$$\Delta\rho_{\mathrm{x}} = \frac{\{\rho(\mathrm{i}+1,\mathrm{j},\mathrm{k}) - \rho(\mathrm{i}-1,\mathrm{j},\mathrm{k})\}}{|\vec{\mathrm{r}}(\mathrm{i}+1,\mathrm{j},\mathrm{k}) - \rho(\mathrm{i}-1,\mathrm{j},\mathrm{k})|}$$

$$\Delta\rho_{\mathrm{y}} = \frac{\{\rho(\mathrm{i},\mathrm{j}+1,\mathrm{k}) - \rho(\mathrm{i},\mathrm{j}-1,\mathrm{k})\}}{|\vec{\mathrm{r}}(\mathrm{i},\mathrm{j}+1,\mathrm{k}) - \rho(\mathrm{i},\mathrm{j}-1,\mathrm{k})|} \tag{3-14}$$

$$\Delta\rho_z = \frac{\{\rho(i,j,k+1) - \rho(i,j,k-1)\}}{|\vec{r}(i,j,k+1) - \rho(i,j,k-1)|}$$

3.9 Density of States

The Density of States (DOS) refers to the number of possible energy levels per unit frequency range in a system. It quantifies the distribution of energy states available to particles in that system. The density of states is calculated by dividing the number of energy states in a given volume by that volume. Mathematically, the density of states is represented as:

$$D(E) = \frac{N(E)}{V} \tag{3-15}$$

where N(E)δE represents the number of states whose energies fall within the range from E to E+δE, and V represents the volume of the system. The density of states is often expressed as a probability density function, which describes the likelihood of finding a particular energy state. It is typically an average over both space and time, taking into account all the states occupied by the system. The density of states is closely connected to the dispersion relations of the system's properties. If there is a high density of states at a specific energy level, it means that there are many available states for particles to occupy at that energy. This has implications for various phenomena and behaviours of the system. In most cases, the density of states in matter is continuous, meaning that there is a smooth distribution of energy levels. However, in isolated systems such as atoms or molecules in the gas phase, the density distribution becomes discrete, resembling a spectral density. Local variations in the density of states, often caused by distortions or deviations from the original system, are known as local densities of states (LDOSs).

The electronic density of states (DOS) holds significant importance in the analysis of electronic structures in VASP, where it is used to examine simulated systems. DOS refers to the count of accessible states with energies that fall below the Fermi energy level, also referred to as the highest occupied molecular orbitals (HOMO), as well as those with energies above the Fermi energy level, known as the lowest unoccupied molecular orbitals (LUMO). It is important to note that the calculations made by the Vaspkit software for all of the DOS numbers that are displayed automatically shift the Femi energy level to zero eV. As an illustrative example, the pDOS for the pristine surface of rutile TiO2 (110) is shown in **Figure 11**. In the case of bulk systems, the DOS per unit volume at a specific energy can be expressed as follows:

$$\mathrm{E} = \frac{1}{\mathrm{V}} \cdot \frac{\mathrm{dN}}{\mathrm{dE}} = \frac{1}{2\pi^2} \left(\frac{2\mathrm{me}}{\hbar} \right) \sqrt{\mathrm{E}} \qquad (3\text{-}16)$$

A comparison between DOS and experimental techniques like Valence-Band X-ray Photoelectron Spectroscopy (VB-XPS) or Hard X-ray Photoelectron Spectroscopy (HAXPES) can be made. This correlation can be achieved by incorporating both Lorentzian and Gaussian broadening functions and by applying weighting factors to the DOS based on atomic orbital photo-ionization cross sections documented by Scofield[190] or Yeh and Lindau [191]. This methodology has been effectively employed in numerous studies to accurately characterize the electronic states produced by XPS measurements [183, 192-194].

3.10Energy Calculations

3.10.1Adsorption energy

In catalyst research, precisely determining the adsorption energy is crucial as it affects both selectivity and catalytic activity. DFT enables accurate computations of the adsorption energy and provides insight into the strength of the interactions between catalyst surfaces and adsorbate molecules. Rational catalyst design, optimization, and reaction mechanism elucidation are made possible by these computations, which frequently include periodic boundary conditions and dispersion corrections. Predicting catalyst poisoning and creating robust catalysts with lengthy operational lives are also significant. All things considered, the computation of adsorption energy is fundamental to comprehending and regulating catalyst-adsorbate interactions for the progress of catalysis studies and the creation of more productive and environmentally friendly industrial processes.

Using a catalyst has a main problem i.e., its stability has to be controlled for its practical use. So the adsorption energy of the catalyst based on its adsorption stability is calculated by employing the following formula:

$$\mathrm{E_{adsorption}} = \mathrm{E_{total}} + \mathrm{E_{slab}} - \mathrm{E_m} \qquad (3\text{-}17)$$

Here, E_{total} represents the total energy of the catalyst and adsorbate, $\mathrm{E_{slab}}$ is the total energy of the catalyst and E_m represents the total energy associated with isolated absorbate. When the overall answer to this equation comes out to be negative, the adsorption mechanism is stable.

3.10.2 The formation energy of an oxygen vacancy

An important quantity in the study of materials, especially in the fields of solid-state physics and chemistry, is the formation energy of an oxygen vacancy. The energy needed to produce an oxygen vacancy in a crystal lattice is represented by this energy. The

electronic structure, lattice relaxation, thermodynamic stability, and other complex aspects of the system's initial and final states are all considered when calculating the formation energy. Predicting and understanding the behavior of materials, particularly in the context of semiconductor devices, catalysts, and ion-conducting materials, requires an understanding of the formation energy of oxygen vacancies. Advanced computational techniques, such as DFT, are frequently used by researchers to precisely determine the formation energy and learn more about the stability and functionality of materials containing oxygen vacancies. This information is crucial for the design and optimization of materials for a variety of uses, including electronic devices and energy storage. To create defects in the system, one of the oxygen atoms is removed from the bulk, and the formation energy of the oxygen vacancy $\mathrm{E_V}$ is calculated as follows:

$$\mathrm{E_V} = \mathrm{E_{s+v}} + \frac{1}{2}\mathrm{E_{O_2}} - \mathrm{E_s} \qquad (3\text{-}18)$$

Here E_{s+V} is the total energy of the defective system, E_{O_2} represents the total energy of gas phase oxygen and E_s is the total energy of the perfect system. For the evaluation of formation and adsorption energies, DFT at the GGA+U level is used.

3.11 Vibrational frequency analysis

In computational chemistry, vibrational frequency analysis is a technique used to study the dynamic behavior of molecules by computing their vibrational modes. Through the use of DFT in VASP, researchers are able to learn more about the vibrational properties of molecular systems, which helps them to better understand stability, reactivity, and other thermodynamic features. A system's thermodynamic properties are its physical attributes that characterize its behavior with respect to temperature, pressure, and other

state variables. In this thesis, the VASPKIT code was utilized to compute the zero-point energies and entropy contributions to the free energies at room temperature (298.15 K) using vibrational frequency analysis. The electrochemical system's free energy is computed using the expression[195].

$$G = E_{DFT} + E_{ZPE} - TS \quad (3\text{-}19)$$

The electronic energy computed using DFT is denoted by E_{DFT}, and the terms TS and E_{ZPE} stand for the entropic energy and total vibrational zero-point energy, respectively.

4 Adsorption of Cu_5/silicates deposited on rutile TiO_2 as a photocatalyst

Titanium dioxide (TiO_2) is an exceptional compound with unique optical properties, which have been intensively used for applications in photocatalysis. Recent studies show that Cu_5 atomic quantum clusters (AQCs) could facilitate visible light absorption and enhance the photocatalytic properties of rutile TiO_2 by creating mid-gap states. In this work, to move the theory of these catalysts closer to the experiment, I investigate the electronic structures of Cu_5 adsorbed on a perfect and reduced rutile TiO_2 surface in the absence and presence of silicate SiO_3^{2-} ions, which are introduced for the purification of Cu_5 AQCs. Encouragingly, my DFT simulations predict that the presence of SiO_3^{2-} does not reduce the gap states of the Cu_5@TiO_2 composite and could even enhance them by shifting more states into the band gap. My results also demonstrate that the polarons created by oxygen vacancies (Ov) and Cu_5 coexist within the band gap of TiO_2. Indeed, an Ov behaves like a negative gate on the electronic states located on the AQCs, thereby shifting states out of the valence band into the band gap, which could lead to enhanced photocatalytic performance.

4.1 INTRODUCTION

The continuous use of non-renewable fossil fuels to fulfil energy demands has released a huge amount of carbon dioxide into the atmosphere resulting in increased global warming and air pollution [196]. To address this issue, the production of hydrogen gas (H_2) is necessary as it is sustainable, energy-dense, and eco-friendly[197]. Hydrogen is used in various fields such as gas welding, petroleum refinery, electricity production, automobile, rocket fuel [198], and transportation fuel [199]. Therefore, it is important to find a cost-effective method of hydrogen manufacture. Current state-of-the-art technologies using water electrolysis to produce pure H_2 have low overall conversion efficiencies (below 20%) because they first require conversion from other forms of energy to electricity[52]. Hence, photocatalytic water splitting to produce hydrogen from water is particularly attractive due to the abundance, availability, and low cost of the water feedstock for a renewable energy source.

Titanium dioxide (Titania; TiO_2) is an exceptional compound with unique optical properties that facilitate photocatalytic activity[200]. It has been intensively utilized in photocatalysis as it is highly stable, non-toxic, eco-friendly, and not costly [201].

However, various limitations prevent the use of TiO_2 in photocatalytic applications[202], which has a large band gap energy of about 3.2 eV. This limits its ability to absorb light to ultraviolet. Additionally, it exhibits a high rate of charge recombination between photogenerated holes in the valence band (VB) and photogenerated electrons in the conduction band (CB). Multiple attempts have been made to successfully modify the band gap of TiO_2 using various doping strategies[203, 204]. According to earlier research, doping with non-

metals or transition metals[205, 206], might be a potential strategy for changing the band edges and boosting TiO_2's photocatalytic activity under visible light.

.Another method to promote the photocatalysis of TiO_2 is by combining TiO_2 and advanced materials such as carbon-based materials, transitional metal dichalcogenides, metal oxides, metal clusters, and metal-organic frameworks[207], which could facilitate charge separation and diffusion of light-induced electrons and holes. In addition, charge separation and catalytic properties are dependent on the size and shape of adsorbed metal particles. For ground-state reactions, the increased catalytic activity is due to the formation of new active sites at the interfaces between metal particles and the surface or in the support overlayer[208].

Metal clusters such as Cu_5 possess a sub-nanometre size and molecule-like electronic structures. They do not sustain their metallicity, lack plasmonic behavior, and have a HOMO−LUMO energy gap like a molecule, which enhances their chemical and physical properties for innovative applications[209] [210]. Cu_5 clusters have a low reactivity to oxygen dissociation, making them resistant to oxidation. As a result, Cu_5 clusters are particularly interesting candidates for catalytic applications than larger systems such as Cu_8 or Cu_{20} [76, 77]. When these copper clusters are deposited on the surface of TiO_2, they can shift the adsorption from the high energy range of the solar spectrum (UV spectrum) to the visible range, corresponding to the highest intensity region of the spectrum of sunlight. Therefore, much more energy can be harvested from sunlight, and the coated TiO_2 can store this energy in the form of electron and hole charge pairs, for later use[211, 212]. Kinetic control through electrochemical methods is used to synthesize Cu_5 clusters exhibiting outstanding chemical and thermodynamical stability in solution throughout the pH range[213]. Nevertheless, the AQCs need to be purified and separated from several contaminants such as Cu^{2+} ions, nitrates, and isopropyl alcohol (IPA). In order to obtain the catalysts with high photocatalytic

performance and achieve scaling up, it is urgent and challenging to improve the purity of Cu_5 clusters, especially by removing the Cu^{2+} ions, which could poison the catalysts. Silicates can be expected to be used as precipitants to extract those Cu_5 clusters and possibly other contaminants as well, where those inorganic groups are predicted to bind to the copper clusters, but not be reduced by them[214] [215] [216] [217] [218]. Due to the presence of silicates, AQCs could be lyophilized and redispersed in pure water, with no loss. This can then be followed by a series of complicated purification processes to remove other contaminants, but the presence of AQC/silicate composites is inevitable. For this reason, it is of interest to examine the properties of such composites when adsorbed onto the surface of titania, to determine if their catalytic properties are hindered or not.

Therefore, in what follows, I explore the interaction between Cu_5 AQCs and silicates and the effect of silicates binding to Cu_5 AQCs on the structural and electronic properties. More specifically, the adsorption properties of Cu_5/silicate on the perfect and reduced TiO_2 are investigated to obtain an in-depth understanding of their electronic properties. Importantly, it is found that the presence of silicates does not hinder the emergence of mid-gap polaronic states, and even increases the number of gap states by behaving like a negative gate on the AQC, which shifts states into the gap from the TiO_2 valence band. In addition, the polaron states due to oxygen vacancies, which coexist with those originating from Cu_5, are not impacted by the presence of silicates.

4.2 COMPUTATIONAL METHODS

By using the method of periodic boundary condition in Vienna Ab initio Simulation Package (VASP)[219-221], the electronic properties, as well as the geometrical properties, are determined for rutile TiO_2 and Cu_5@TiO_2 in the absence and presence of silicates and oxygen

vacancies. Interactions between valence electrons and the ion core of copper, oxygen, silicon, and titanium are described through the projector augmented wave (PAW Method) method[156, 222] using the Spin-polarized Density Functional Theory approach. The $3d^{10}4s^1$ orbitals of Cu, $2s^2\ 2p^4$ of O, $3s^2 3p^2$ of Si, $3s^1$ of Na, and $3s^2\ 3p^6\ 4s^2\ 3d^2$ of Ti are referred to as valence electrons. The Generalized Gradient Approximation (GGA) functional alone is unsuitable for electronic structure calculations, as it introduces more than a 50 percent error in the bandgap calculation for some materials[223]. Since such inaccuracies render it much more challenging to locate the conduction and valence bands, I introduce some corrections to bring the value closer to the experimental one[223]. Here the electronic exchange-correlation was introduced by a GGA functional along with the correction term, GGA + Hubbard U, as GGA in its original form, cannot predict the polaronic states, i.e., the SOMO that arises in Ti^{3+} of TiO_2 and that of Ce^{3+} in CeO_2[224, 225]. In accordance with the literature, the value of U for titanium and copper is taken as 4.2 eV and 5.2 eV, respectively[211]. Using the basis set of plane wave types, with a cut-off energy of 500 eV, the wavefunctions of Kohn-Sham were further extended. Samples of Γ-point were taken for all the cases. Further corrections for portraying the states of 3D orbitals in transition metal oxides were achieved using hybrid functional HSE06[226].

The D3 technique of Grimme incorporates Van der Waals corrections from spin-polarized Perdew, Burke, and Ernzerhof (PBE) along with Becke-Jonson damping function to precisely determine binding or adsorption energies along with the geometrical optimizations [209]. Using the HSE06 basis set, the electronic properties and structures of all the systems, i.e., rutile TiO_2 (110) surface, rutile TiO_2 (110) surface with Cu_5 AQCs in the absence and presence of SiO_3^{2-} and reduced TiO_2 (110) surface with Cu_5 AQCs in silicate presence and absence, were computed based on configurations optimized by the spin-polarized DFT D3 technique. The Bader analysis technique[227] for studying the distribution of atomic charge is adopted for the

results obtained by the calculations through Spin-polarized hybrid functional HSE06[209, 226-228].

Due to its abundance and accessibility, rutile TiO_2 has been the subject of the majority of surface science studies. Surfaces are essential for understanding the reactivity of materials and play a significant influence in determining the characteristics of nanomaterials. The (110) surface of rutile, among periodic TiO_2 slabs of the (001), (100), (110), and (011) face, has the lowest surface energy, indicating that it is the most stable surface, according to DFT and ab initio calculations[229]. This thesis investigates rutile TiO_2 (110) as one of its slab models. **Figure 11** illustrates the pristine surface of rutile TiO_2 (110) and EDOS.

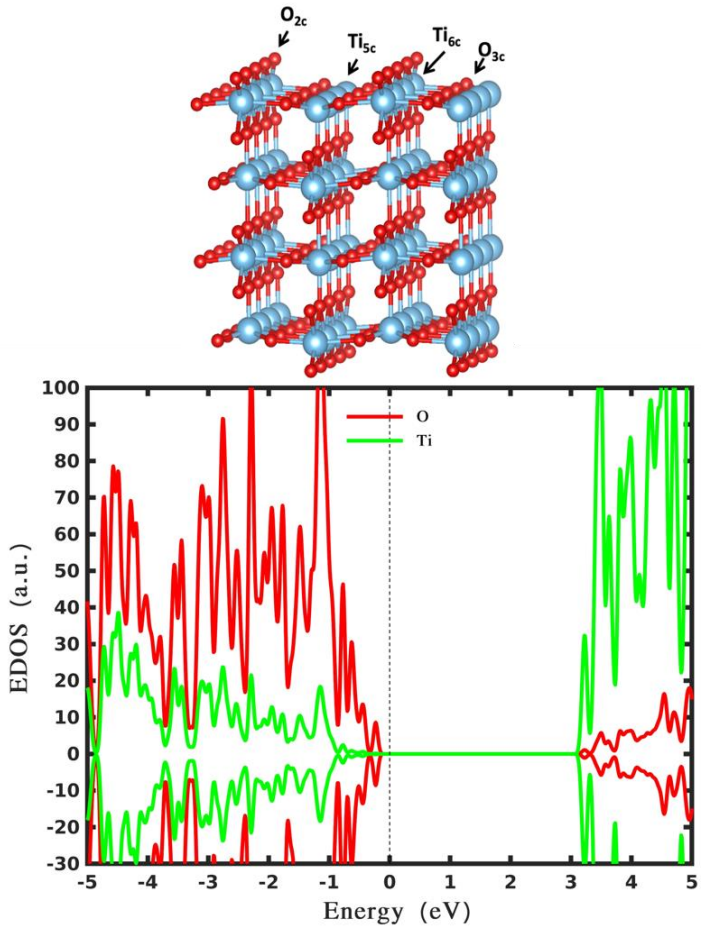

Figure 11 Schematic of the rutile TiO_2(110) slab model and the corresponding density of states. Blue and red balls in the left panel represent titanium and oxygen atoms (the color scheme is used in the following figures). O_{2c} denotes the two-fold coordinated oxygen atom while O_{3c} represents the three-fold coordinated oxygen atom. Ti_{2c} stands for the five-fold coordinated titanium atom while Ti_{6c} is for the six-fold coordinated titanium atom. The green and red curves depict the projected density of states on titanium and oxygen atoms, while the black curve is the total density of states.

The rutile TiO_2 (110) surface containing 64 Ti atoms and 128 oxygen atoms is modelled by 12.04 Å x 13.12 Å unit cells in four O-Ti-O trilayers periodic slab. To ensure that the supercell itself and the periodic images in the z-direction will not interact, a 20 Å vacuum is employed in the z-direction. The active sites on the rutile TiO_2(110) surface, are under-coordinated atoms, containing two-fold coordinated oxygen atoms (O_{2c}) at bridge sites and five-fold coordinated titanium atoms (Ti_{5c}), whereas the inactive saturated atoms are three-fold coordinated oxygen atoms (O_{3c}) and x-fold coordinated titanium atoms (Ti_{6c}) shown in **Figure 11.** VESTA software [230] is used to build and visualize all of the structures shown.

4.3 RESULTS AND DISCUSSION

4.3.1 The adsorption of SiO_3^{2-} on Cu_5

First, as a benchmark calculation, I investigated the gas-phase stability of Cu_5 AQCs. **Figure 14a, c** illustrates the geometries of Cu_5 AQCs. These simulations reveal that the 2-dimensional (2d) planar configuration in **Figure 14,**is more energetically preferable by 0.26 eV than the 3-dimensional (3d) bipyramidal configuration shown in **Figure 14a** in the gas phase. As seen in

Figure 14, the bipyramidal Cu_5 cluster lacks precise D3h symmetry and consists of a trigonal ring (equatorial Cu atoms) with capping atoms (axial Cu atoms) above and below the ring. Those results are consistent with \ previous publication [209]. Next, the effect of a silicate ion SiO_3^{2-} on structural and electronic properties is investigated, because silicates are introduced as a by-product during the Cu_5 purification process. In order to simulate the silicate ion SiO_3^{2-} using DFT, we examined a neutral system consisting of two sodium Na^+ ions adsorbed on one silicate ion SiO_3^{2-}. From Bader charge analysis, it is found that two Na atoms donate 2 electrons to silicon oxide moiety and SiO_3^{2-} is formed, which indicates that the correct silicate model with 2- a valence charge is adopted. The model for a neutral system with a Cu atom as the cation fails to give a divalent silicate ion, and was therefore abandoned. (See more details in **Figure 12).** More importantly, the sodium atoms make no contributions to the gap states, which further demonstrates the neutral system Na_2SiO_3 is an appropriate model molecule for understanding the effect of silicate ions.

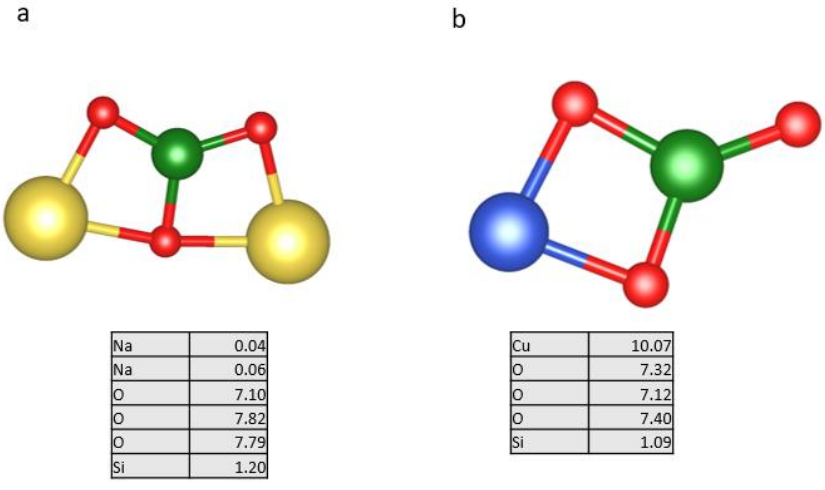

Figure 12 Simulations for neutral system Na_2SiO_3 (a) and $CuSiO_3$ (b). The yellow ball represents Na atom, the blue represents Cu atom, the red represents O atom, and the

green represents Si atom. The bottom tables show the number of valence electrons for each atom.

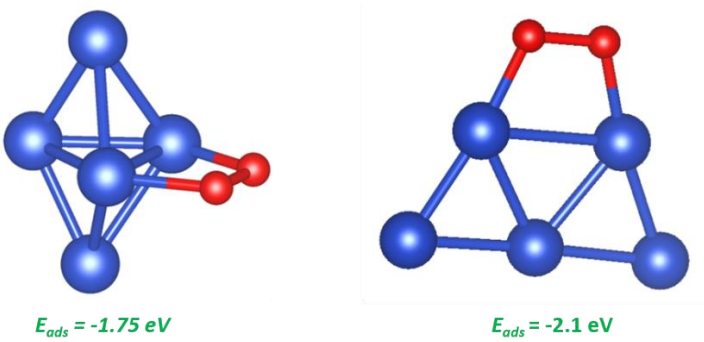

Figure 13 One oxygen dimers adsorbed on a pyramidal (a) and trapezoidal (b) Cu_5 AQC. the green numbers show the adsorption energies of the most stable configurations of oxygen.

To gain a better understanding of the impact of silicate, I first studied the adsorption of SiO_3^{2-} on the gas phase Cu_5 AQCs, as shown in **Figure 14b** and **d** which are the most stable pyramidal and trapezoidal Cu_5/ SiO_3^{2-}. It is found that the SiO_3^{2-} binds more strongly to a Cu_5 AQC than oxygen (see **Figure 13**) for both pyramidal and trapezoidal shapes with a large adsorption energy E_a = -2.92 eV (pyramidal) and E_a = -2.45 eV (trapezoidal) respectively, while for O_2, E_a = -2.1 eV and -1.75 eV. This means that in the presence of O_2 and SiO_3^{2-}, the SiO_3^{2-} will bind first to the Cu_5 AQCs. The adsorption energies E_a of SiO_3^{2-} were estimated to examine the stability of the complex using the equation

$$E_a = E_{Cu_5SiO_3^{2-}} - (E_{Cu_5} + E_{SiO_3^{2-}}) \qquad (4\text{-}1)$$

In this equation, $E_{Cu_5SiO_3^{2-}}$ is the total energy of Cu_5 with the silicate SiO_3^{2-} adsorbed, E_{Cu_5} is the total energy of Cu_5 without SiO_3^{2-}, and $E_{SiO_3^{2-}}$ is the total energy of SiO_3^{2-}. (Note: silicate

ion is accompanied by two Na cations). Net charges from Bader charge analysis are displayed by the green numbers around each atom. As expected, each of the sodium atoms loses roughly 0.9 electrons to create the silicate ion of interest. Additionally, the pyramidal Cu_5 gains about 0.18 electrons from the bonded silicate. While the trapezoidal loss is around 0.1 electrons. A metastable binding configuration (right panel) alongside the most stable (left panel) one for both pyramidal and trapezoidal is presented in **Figure 15 and Figure 16**respectively. **Table 2** illustrates the bond lengths for both pyramidal and trapezoidal with and without SiO_3^{2-} . It is clear that after adding SiO_3^{2-}. Most of the bonds have been changed; for example, the bond between 4 and 5 atoms has been elongated in both pyramidal and trapezoidal, while the bond length between 2-5 and 4-2 has been shortened.

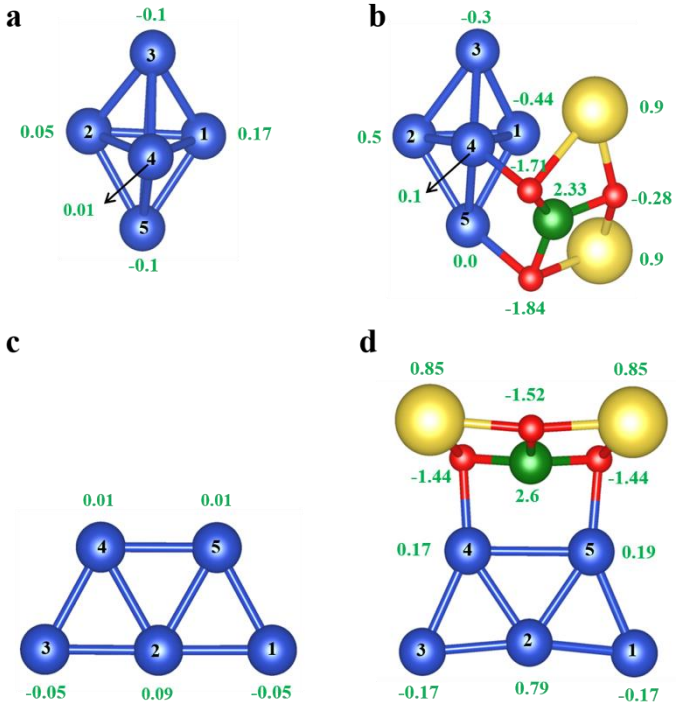

Figure 14. Configurations and net charges of pyramidal Cu_5 (a) and pyramidal Cu_5/SiO_3^{2-} (b), trapezoidal Cu_5 (c) and trapezoidal Cu_5/SiO_3^{2-} (d). The green number displays the net (excess) charges on each atom and the black number orders each atom. The Blue balls

represent Cu atoms, the red ones are for O atoms, the yellow for Na atoms, and the green for Si atoms.

Table 2 Bond lengths comparison for pyramidal and trapezoidal Cu_5 isomers.

Bond length	Pyramidal	Pyramidal/ SiO_3^{2-}	Trapezoidal	Trapezoidal/ SiO_3^{2-}
1-3	2.40 Å	2.40 Å	…….	…….
1-5	2.40 Å	2.42 Å	2.35 Å	2.36 Å
4-3	2.42 Å	2.35 Å	2.35 Å	2.36 Å
4-5	2.42 Å	2.62 Å	2.37 Å	2.68 Å
2-3	2.42 Å	2.55 Å	2.33 Å	2.33 Å
2-5	2.42 Å	2.36 Å	2.38 Å	2.36 Å
1-2	2.33 Å	2.42 Å	2.33 Å	2.33 Å
1-4	2.33 Å	2.47 Å	…….	……..
4-2	2.53 Å	2.35 Å	2.38 Å	2.36

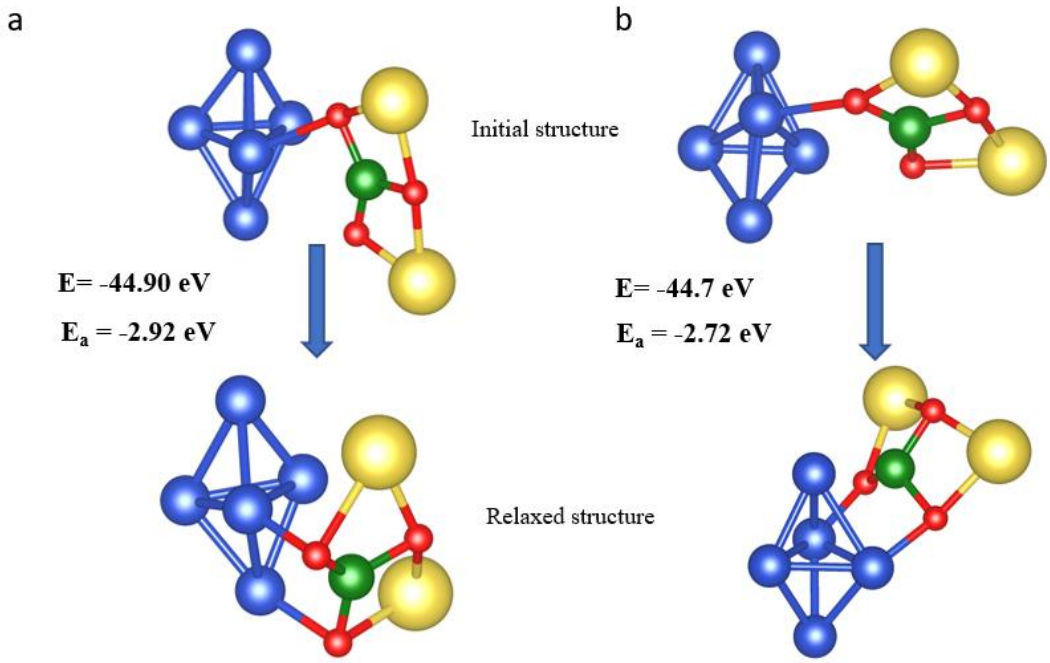

Cu 1	10.50
Cu 2	11.44
Cu 3	11.0
Cu 4	10.9
Cu 5	11.3
Na 1	0.11
Na 2	0.13
O 1	7.84
O 2	6.28
O 3	7.71
Si	1.76

Cu 1	10.73
Cu 2	10.71
Cu 3	11.36
Cu 4	10.78
Cu 5	11.19
Na 1	0.12
Na 2	0.11
O 1	7.53
O 2	7.51
O 3	7.58
Si	1.38

Figure 15 Configurations, adsorption energies, and total energy of SiO_3^{2-}adsorbed on a bipyramidal Cu_5 cluster. Most sable (a), metastable (b). The bottom tables show the number of electrons in the valance bands for each atom.

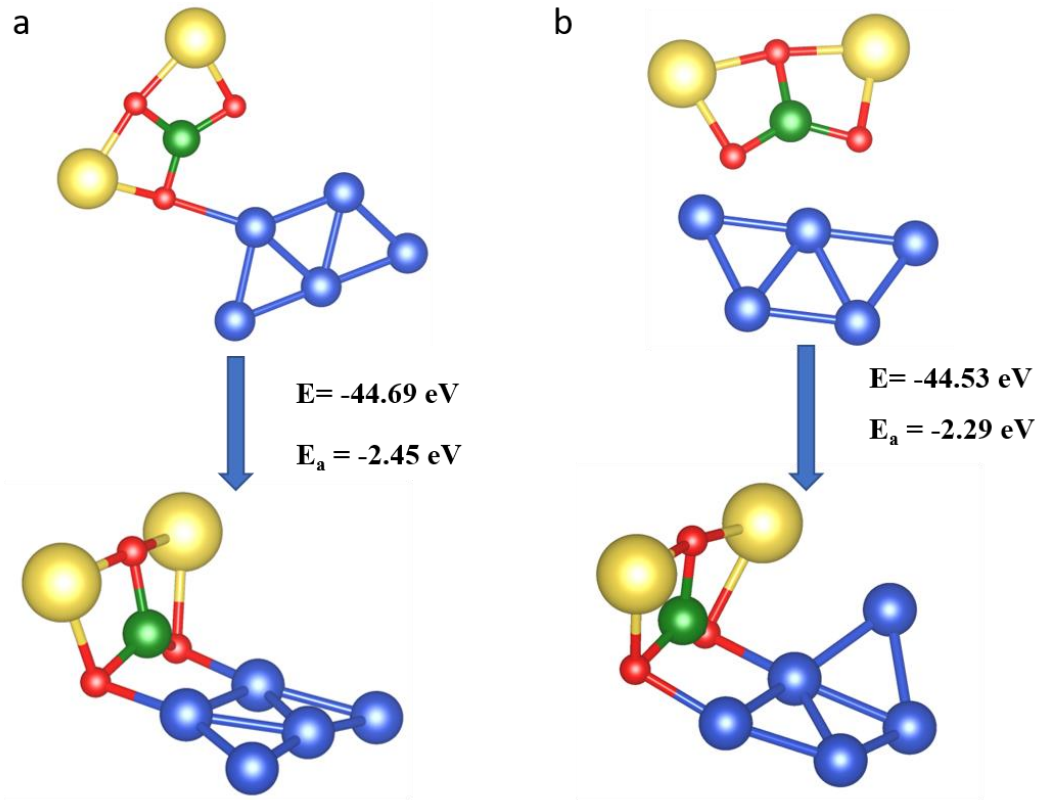

Cu 1	11.18
Cu 2	10.94
Cu 3	11.16
Cu 4	10.83
Cu 5	10.81
Na 1	0.16
Na 2	0.15
O 1	7.44
O 2	7.52
O 3	7.42
Si	1.40

Cu1	11.10
Cu2	10.21
Cu3	11.65
Cu4	10.68
Cu5	11.46
Na1	0.09
Na2	0.19
O1	7.66
O2	6.98
O3	7.02
Si	1.95

Figure 16 Configurations, adsorption energies, and total energy of SiO_3^{2-} adsorbed on a trapezoidal Cu_5 cluster. Most sable (a), metastable (b). The bottom tables show the number of electrons in the valance bands for each atom.

4.3.2 The deposition of Cu_5 on a pristine and reduced rutile TiO_2(110)

To investigate the geometrical stability of AQCs on the pristine rutile TiO_2 (110) substrate, I deposited the optimized trapezoidal and pyramidal clusters on the surface of TiO_2 at different angles and positions, as shown in **Figure 17a**. Furthermore, I calculated the total energies with respect to the different configurations created by tilting and displacing the Cu_5 AQCs on supports, as depicted in **Figure 17b**. The results exhibit that structure 4 is the most stable configuration, which deforms to a new pyramid-shaped structure with the adsorption energy up to -2.26 eV. In contrast, structures 3 and 7 are found to be the metastable structures which are shed light on in the following texts and the remaining are presented at the end of this chapter **(Figure 32).**

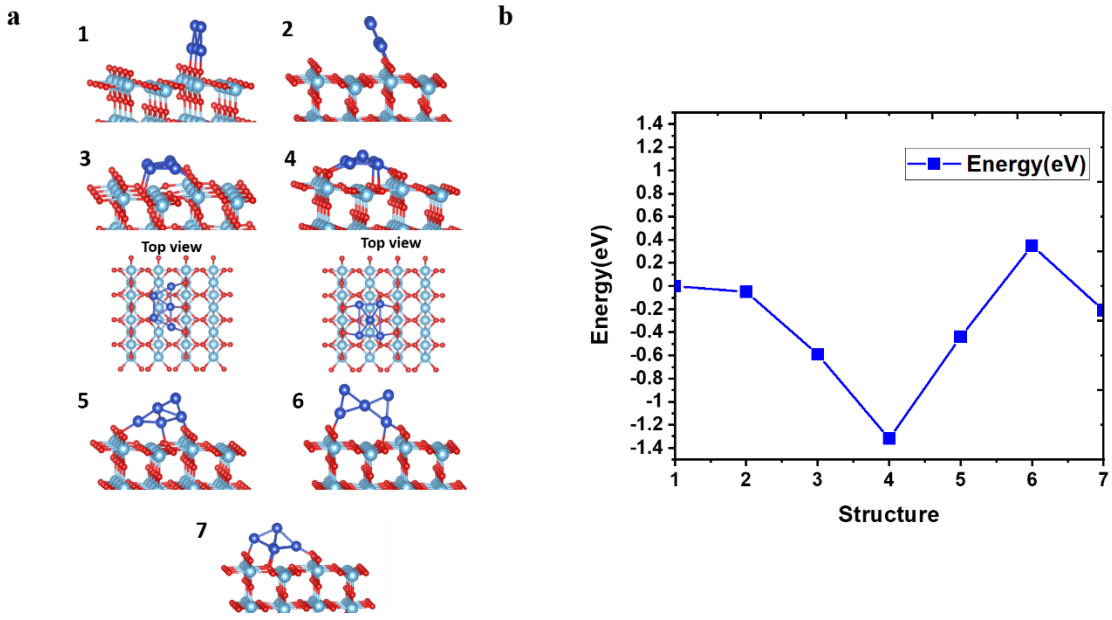

Figure 17. Configurations and energetics of Cu_5 cluster deposited on rutile TiO_2 (110) surface. Geometrically optimized configurations based on different positions (a), and energy evolution as the function of different positions of Cu_5 cluster (b).

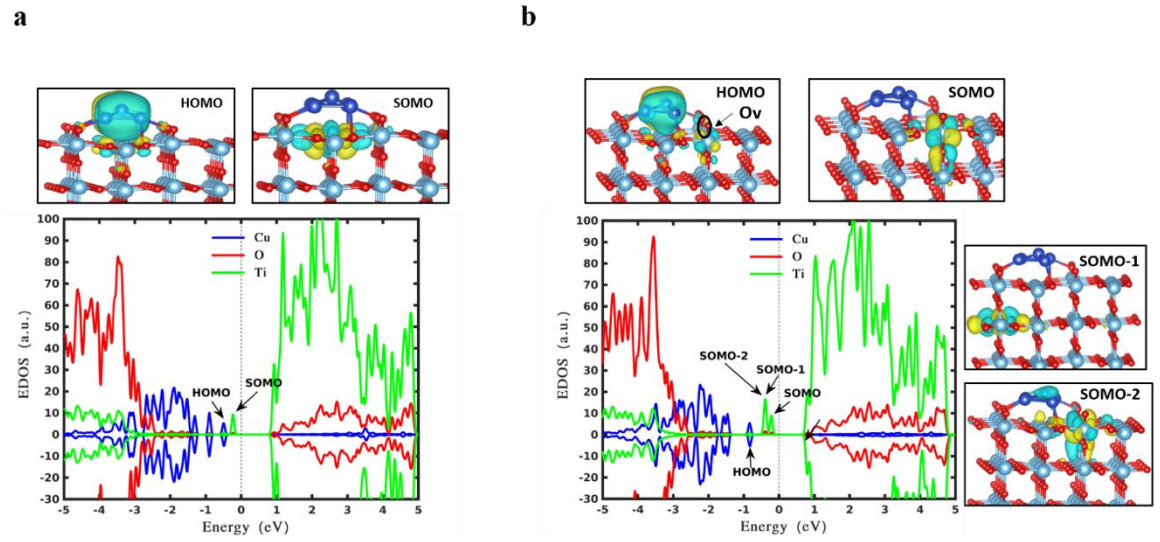

Figure 18. Frontier molecular orbitals and spin density of states of the most stable structure originating from the trapezoidal Cu_5 on a pristine rutile TiO_2 (110) surface (a) and a reduced rutile TiO_2 (110) (b). The SOMOs and HOMO are presented (SOMO: the singly occupied molecular orbital; HOMO: the highest occupied molecular orbital). The green, red, and blue curves represent the states located on titanium, oxygen, and copper atoms respectively. Bader charge analysis reveals that 1.1 electrons (a) and 0.99 electrons (b) are transferred from Cu_5 to the support. The dashed line at 0 eV indicates the Fermi energy level.

The hybrid HF/DFT HSE06 functional provides a direct band gap of 3.26 eV for the (rutile) TiO_2 (110) surface in this work (see **Figure 11**). Moreover, this approach likewise considers restricted gap states in various modifications of TiO_2, such as introducing localized Ti^{3+} 3d states below the conduction band. Bader analysis reveals that a Cu_5 cluster transfers 1.1 electrons to the pristine TiO_2; As can be observed in **Figure 18a**, the donated electron becomes

localized in one specific 3d orbital lying at the surface plane and cantered at the titanium (5f) atom right below the Cu_5 cluster, resulting in a localized polaron at 1.0 eV below the conduction band. This polaronic state is depicted by the green peak in the vicinity of 0 eV in the density of states (DoS) plot, and by the yellow and green electronic clouds in the wavefunction SOMO (the Singly Occupied Molecular Orbital) at the top of the graph. The wavefunction of the HOMO (the Highest Occupied Molecular Orbital) situated on the Cu_5 clusters, is represented by a blue peak near -0.5 eV. It is also noted that many gap states are observed resulting from the copper cluster, which improves the absorption of visible photons and enables photocatalytic activities.

Creating oxygen vacancies in TiO_2 can introduce variations in electronic, optical, and structural properties. This can result in enhanced applications of TiO_2 such as improved photocatalytic and magnetic properties [22]. Furthermore, they can also serve as active sites for water splitting. The oxygen vacancies cause the distortion of the TiO_2 lattice, which results in the formation of polaronic states [231]. These oxygen defects give rise to Ti^{3+} 3d states, the presence of which can be confirmed by observing the peaks of the photoemission spectrum [232]. Through the spectrum obtained by optical absorption spectroscopy, it can be demonstrated that oxygen vacancy allows absorption in the visible region of electromagnetic radiation[233]. In this current study, I have investigated the effects of depositing those trapezoidal and pyramidal Cu_5 clusters on a reduced rutile TiO_2(110) in order to understand the interactions between adsorbates and oxygen vacancies to gain more sights into the more practical issues. As benchmark calculations, one bridging oxygen vacancy on the rutile TiO_2 (110) surface is created, and a defective substrate[231] is formed, where two excess electrons are generated resulting in two polarons as shown in **Figure 19**. The polaronic states represented by the green peeks below the bottom of the conduction band can be observed. Similar results

were obtained for various oxygen vacancy positions, where the energies of these gap states are in very good agreement with EELS observations[234].

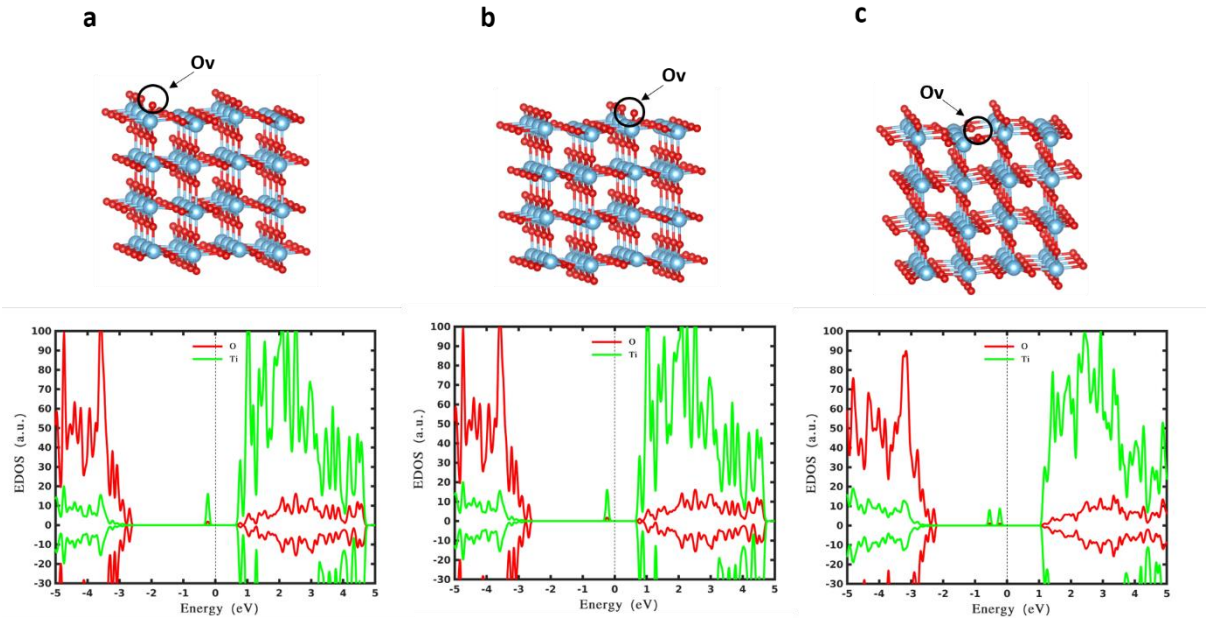

Figure 19 Relaxed configurations of reduced TiO_2 for different positions of Oxygen vacancy, and their corresponding spin densities of states.

Figure 18b represents gap states when the trapezoidal Cu_5 cluster is deposited onto the surface of reduced rutile TiO_2. Overall, the gap states due to the copper (blue curves) decrease a little, which might originate from the shape change of the cluster in the absence and presence of the oxygen vacancy. However, the polaron state increases from one (SOMO peak of **Figure 18a**) to three (green peaks below the Fermi level: SOMO-2, SOMO-1, SOMO peaks of **Figure 18b**). As previously mentioned, the oxygen vacancy in rutile TiO_2 leads to two excessive electrons resulting in two polaronic states, which get concentrated on the oxygen atoms in the neighborhood. An additional alteration of the surface by placing AQC on TiO_2 induces the formation of the third polaronic state owing to the one-electron transferred from AQC to the substrate which gets trapped into the empty 3d state of the titanium atom. [235-237]. It is

concluded that the polarons originating from oxygen vacancy and deposited cluster coexist with each other and no suppression is observed.

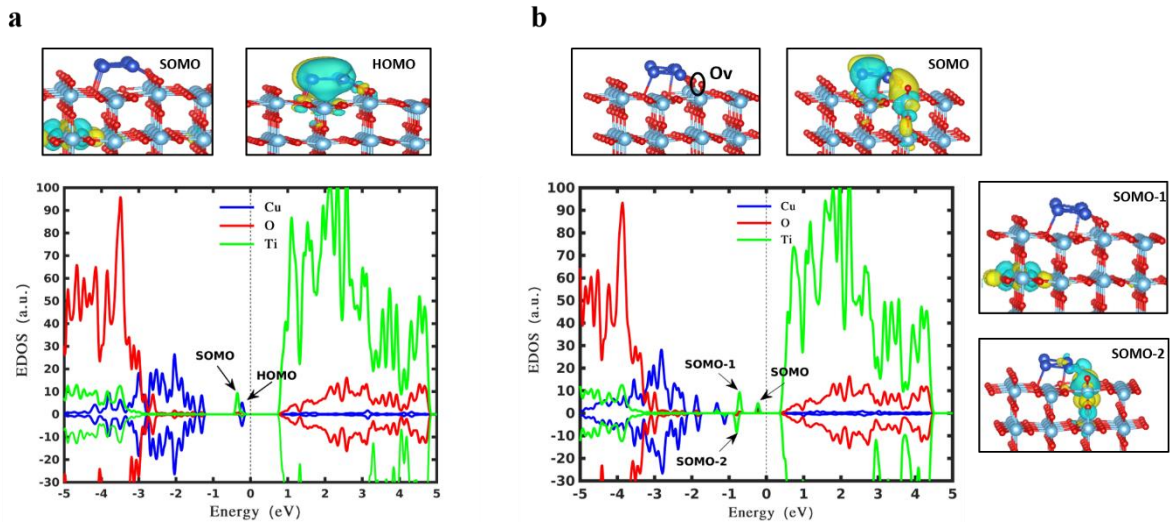

Figure 20 Frontier molecular orbitals and spin density of states of the metastable trapezoidal Cu_5 cluster deposited on a pristine (a) and reduced (b) rutile TiO_2(110). The green, red, and blue curves represent the states located on titanium, oxygen, and copper atoms respectively. Bader charge analysis reveals that 1.03 electrons (a), and 0.77 electrons (b) electrons are transferred from Cu_5 to the support. The dashed line indicates the Fermi energy level of 0 eV.

The undeformed planar Cu_5 is further investigated, which is the metastable structure shown in **Figure 20a**. This trapezoidal Cu_5 transfers 1.03 electrons to the titania support, which induces one polaronic state to sit at around -0.3 eV. The overall gap states due to copper atoms (blue curves) decrease a little compared with the most stable structure shown in **Figure 18**a. By contrast, on the reduced surface presented in **Figure 20b**, the cluster donates 0.77 electrons to the support, which is 0.26 electron less than the stoichiometric surface. This may be explained by the fact that the oxygen vacancy induces a less evenly distributed charge on the reduced TiO_2 surface[231].

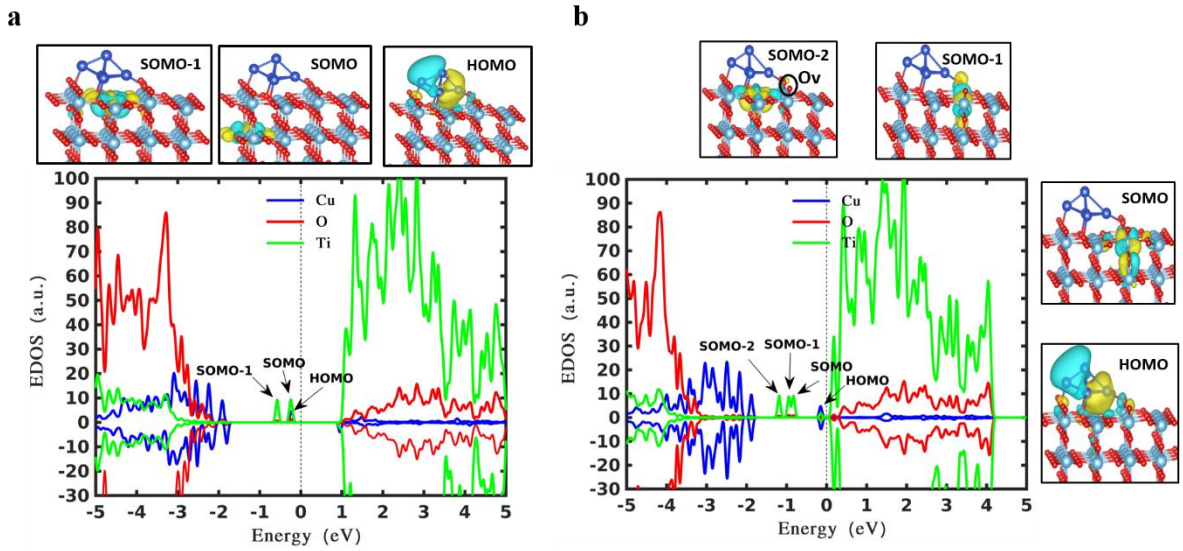

Figure. 21. Frontier molecular orbitals and spin density of states of bipyramidal Cu_5 deposited on a pristine (a) and reduced (b) rutile TiO_2(110). The green, red, and blue curves represent the states located on titanium, oxygen, and copper atoms. Bader charge analysis reveals that 1.4 electrons (a) and 1.0 electrons (b) are transferred from Cu_5 to the support. The dashed line indicates the Fermi energy level of 0 eV.

In contrast, the decoration of bipyramidal AQC is shown in **Figure. 21** on a pristine and reduced TiO_2 surface. On a pristine surface, two polaronic states (green peaks in the vicinity of the Fermi level) are obtained which stem from the charge transfer of 1.4 electrons, and fewer gap states originating from the Cu_5 cluster are observed compared to the more planar structures shown in **Figure 18** and **Figure 20**. These benchmark calculations are consistent with a previous publication. [13] When this bipyramidal Cu_5 is deposited on the reduced surface, very interesting results are obtained. First, the blue curves shift out from the valence band leading to more gap states, which can promote the absorption of light in the visible range. This suggests that the reduced surface imposes a negative gating effect on the Cu_5 cluster, which causes an upward shift for the electronic states sitting on the cluster. Second, three polarons (SOMO-2,

SOMO-1, and SOMO) are created instead of four. From the Bader charge analysis, 1 electron is transferred to the substrate, which is 0.4 less than the case of the pristine substrate, indicating that the reduced surface with unevenly dispersed charges also prevents the charge transfer from Cu_5. Actually, the above negative gating effect and the prevention of the charge transfer are both reflections of the strong interaction between the reduced surface and the bipyramidal Cu_5. However, it still can be concluded that the polarons created by charge transfer of AQC and oxygen vacancy coexist. This phenomenon is not observed for the new pyramidal Cu_5 in **Figure 18**. Last but not least, a high-energy HOMO (the little blue peak in the vicinity of the Fermi level) is obtained, where the states are located on the Cu_5 cluster. This high energy level indicates the presence of active sites on the Cu_5 cluster, which can easily donate electrons to the proton to promote the hydrogen evolution reaction (HER). It is noted that one Cu-Cu bond is elongated due to the nearby oxygen vacancy on the surface. Finally, we suggest that the high-energy level is associated with specific bond elongation, which is verified by constructing a similar metastable structure on the pristine surface **Figure 22**.

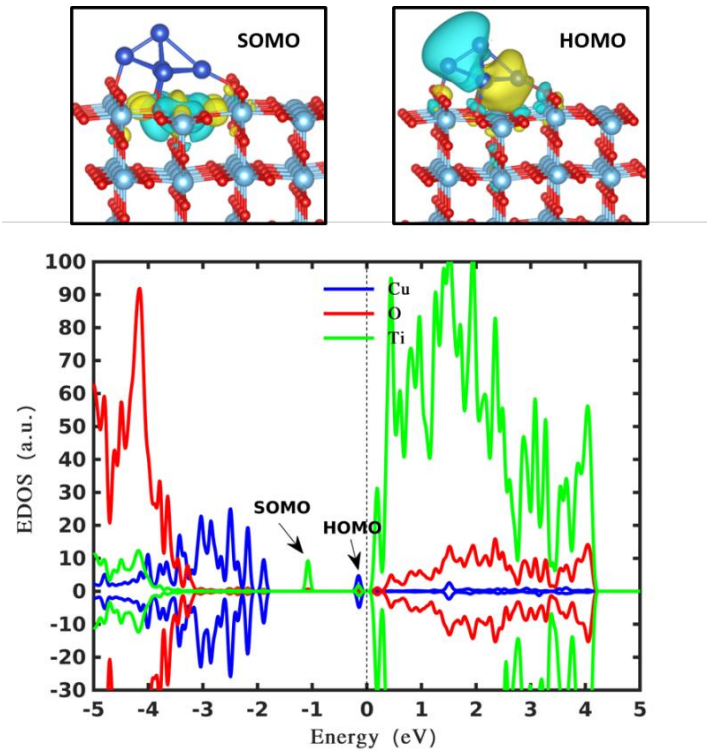

Figure 22 Frontier molecular orbitals and spin density of states of the metastable pyramidal Cu_5 cluster deposited on a pristine rutile TiO_2(110). The green, red, and blue curves represent the states located on titanium, oxygen, and copper atoms respectively. The dashed line indicates the Fermi energy level of 0 eV.

4.3.3 The deposition of Cu_5/ SiO_3^{2-} on a pristine and reduced rutile TiO_2(110)

As one of the key issues of this work, I aim to study and understand the influence of silicates, which are introduced experimentally during the purification process. Therefore, further calculations are carried out in terms of the geometric and electronic properties of Cu_5/ SiO_3^{2-} deposited on TiO_2, based on the optimal adsorption configuration of Cu_5 on TiO_2 shown in **Figure 17** and the most stable trapezoidal Cu_5/ SiO_3^{2-} in **Figure 14d**. From **Figure. 23**, it is clear that there is no contribution from sodium atoms to the gap states. As for the gap states, no decrease is observed compared to the bare AQC shown in **Figure 18**, which shows that the

adsorption of silicate does not affect the electronic structures of AQCs and therefore photo absorption will not be impacted. Bader charge analysis demonstrates that the Cu_5/ SiO_3^{2-}complex transfers around 1.04 electrons to the TiO_2, creating a polaronic state at 1.1 eV below the bottom of the conduction band (see the green peak at ~-0.2eV). This polaron is located at the sublayer of the TiO_2 (110) slab as seen from the wavefunction plotting in the top panel of **Figure. 23a**. By contrast, on the reduced surface shown in **Figure. 23b**, two polarons are observed which stem from the 0.94 electron transfer from the AQC complex and the one oxygen vacancy (SOMO and SOMO-1) as seen in the top panel of **Figure. 23b.** While the second green peak at around -0.3 eV corresponds to the SOMO-2 which is created by the transferred electron from the cluster to the second layer of the substrate**.**

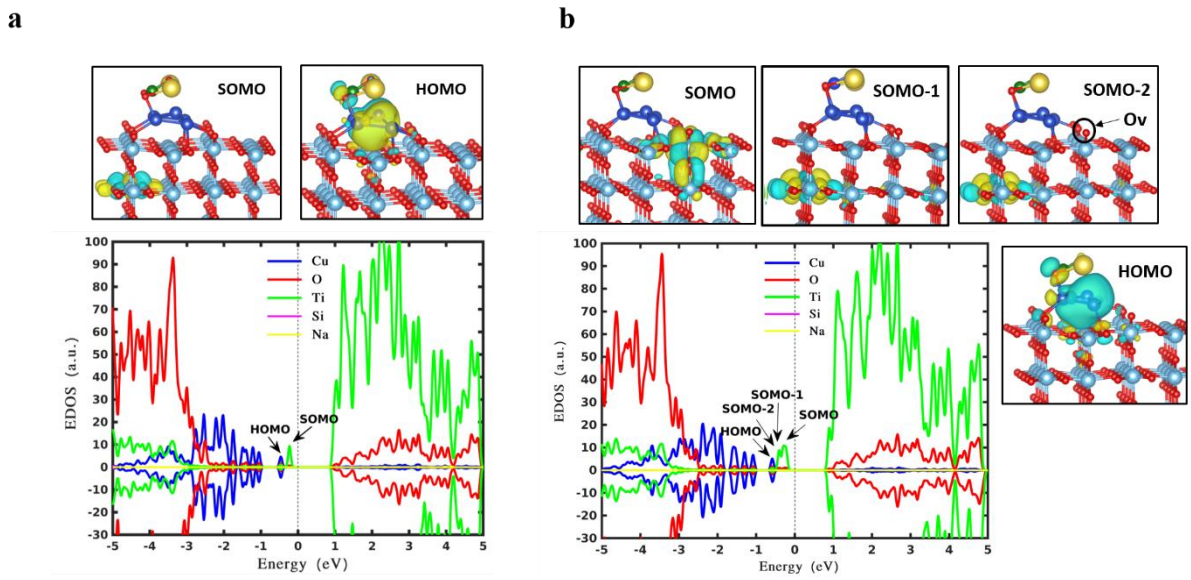

Figure. 23. Wavefunctions of trapezoidal Cu_5 cluster in the presence of SiO_3^{2-}deposited on a pristine rutile TiO_2(110) surface(a), and on a reduced rutile TiO_2(110) surface (b), and their corresponding spin densities of states. The green, red, and blue curves represent the states located on titanium, oxygen, and copper atoms respectively. Bader charge analysis reveals that 1.02 electrons (a) and 0.94 electrons (b) are transferred from Cu_5 to the support. The dashed line indicates the Fermi energy level of 0 eV.

Figure. 24 shows the adsorption of SiO_3^{2-} onto the pyramidal AQC adsorbed on rutile TiO_2 (110). In comparison to the bare pyramidal Cu_5 on support presented in **Figure. 21**, several differences are observed. First, whatever the stoichiometric or the reduced nature of the surface, the gap states increase, as indicated by the upward shifting of the blue curves, which will promote the absorption of light in the visible range. This suggests that the silicate ions apply a negative gating effect on those 3-dimentional Cu_5 cluster, which causes the upward displacement of the electronic states sitting on the cluster. Secondly, one polaron (SOMO) is formed for the stoichiometric surface shown in **Figure. 24a**. From the Bader charge analysis, 1 electron is transferred to the substrate, which is 0.4 less than the case of the bare cluster shown in **Figure. 21a.** However, the results shown in **Figure. 24b** demonstrates that the polarons created by charge transfer of AQC and oxygen vacancy coexist. Third, the high-energy HOMO is not obtained with silicate adsorption, which might be understood by the fact the AQC deforms a lot and many elongations in bond length occur. In addition, different positions of oxygen vacancies have been investigated for both pyramidal and trapezoidal **(s**ee **Figure 33).**

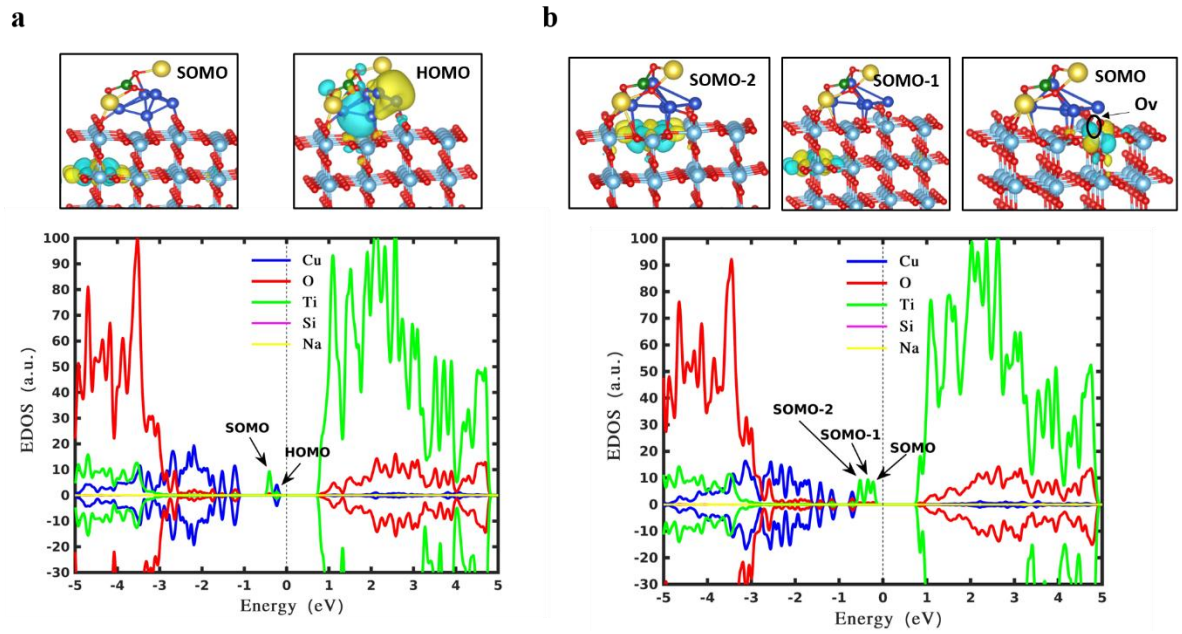

Figure. 24. Wavefunctions of pyramidal Cu_5 cluster in the presence of SiO_3^{2-} deposited on a pristine rutile TiO_2(110) surface (a), and on a reduced rutile TiO_2(110) surface (b), and their corresponding spin densities of states. The green, red, and blue curves represent the states located on titanium, oxygen, and copper atoms respectively. Bader charge analysis reveals that 1.0 electrons (a) and 1.0 electrons (b) are transferred from Cu_5 to the support. The dashed line indicates the Fermi energy level of 0 eV.

For more detailed investigations, I also considered different deposition positions of the metastable trapezoidal and pyramidal of Cu_5/SiO_3^{2-} on rutile TiO_2(110) surface (**see Figure 25 and Figure 26**) , and we also considered more silicate adsorption such as two and three SiO_3^{2-} on a perfect and reduced TiO_2(110) See more details in (**Figure 27, Figure 28, Figure 29, Figure 30, Figure 31**) .To conclude, during the purification process of the Cu_5 AQCs in a water solution, the doping of Cu_5/ SiO_3^{2-} does not reduce and even, in some cases, enhances the gap states of TiO_2 (110).

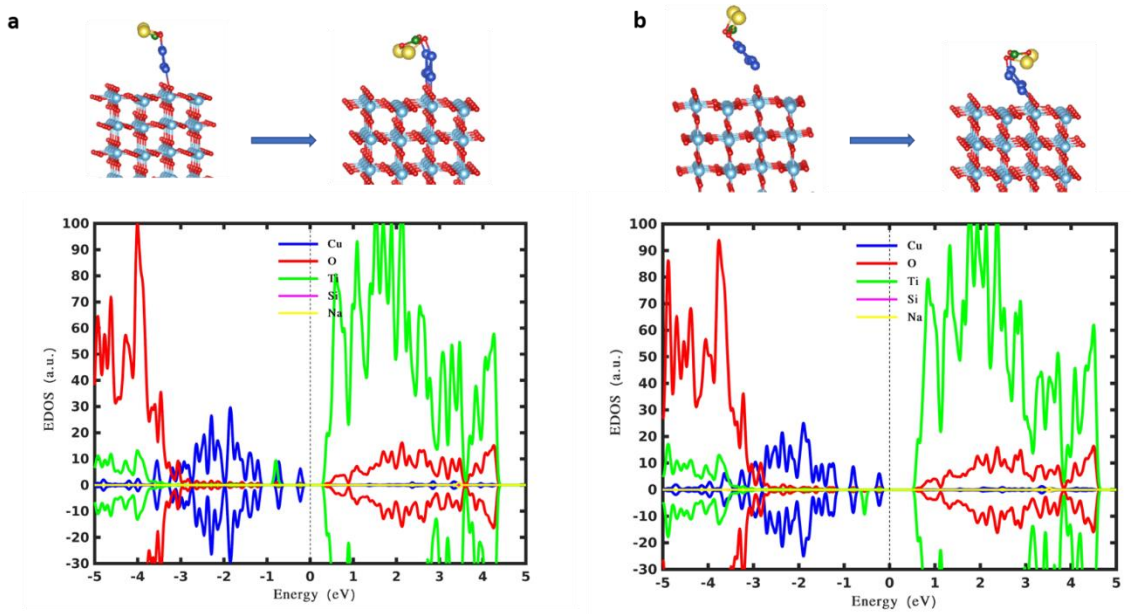

Figure 25 Wavefunctions of trapezoidal (a), and tilted trapezoidal (b) Cu_5 cluster in the presence of SiO_3^{2-} deposited on rutile TiO_2(110) surface, and their corresponding spin densities of states. The SOMO and HOMO wavefunctions are presented in the top panels (HOMO: highest occupied molecular orbital). The green, red and blue curves represent the states located on titanium, oxygen, and copper atoms respectively. Bader charge analysis reveals that 0.7 electrons (a) and 0.8 electrons (b) are transferred from Cu_5 to the support. The dashed line indicates the Fermi energy level of 0 eV.

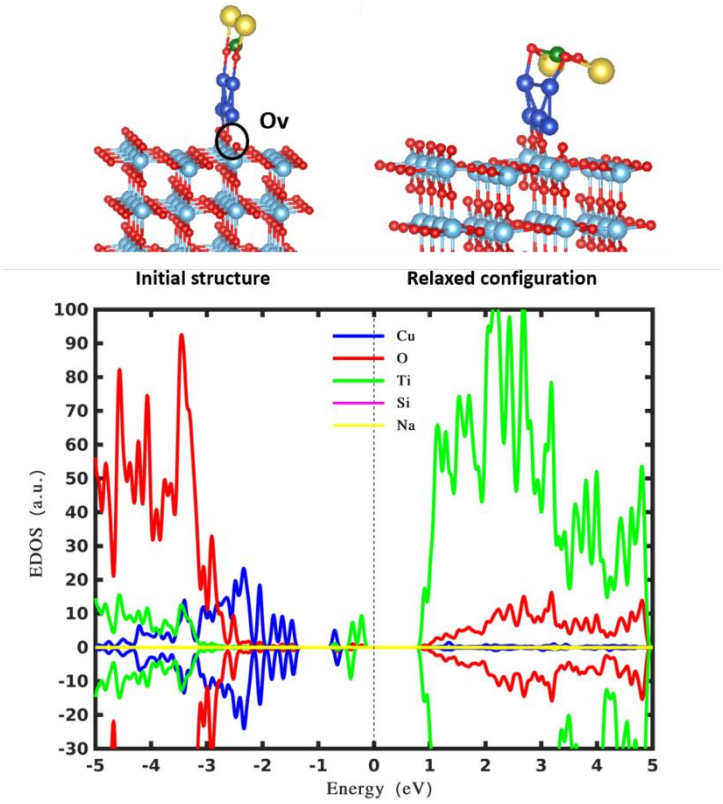

Figure 26 Configurations of trapezoidal Cu5/ SiO_3^{2-} deposited on rutile TiO2(110) and the corresponding density of states. The green, red and blue curves represent the states located on Titanium, oxygen, and copper atoms. The dashed line indicates the Fermi

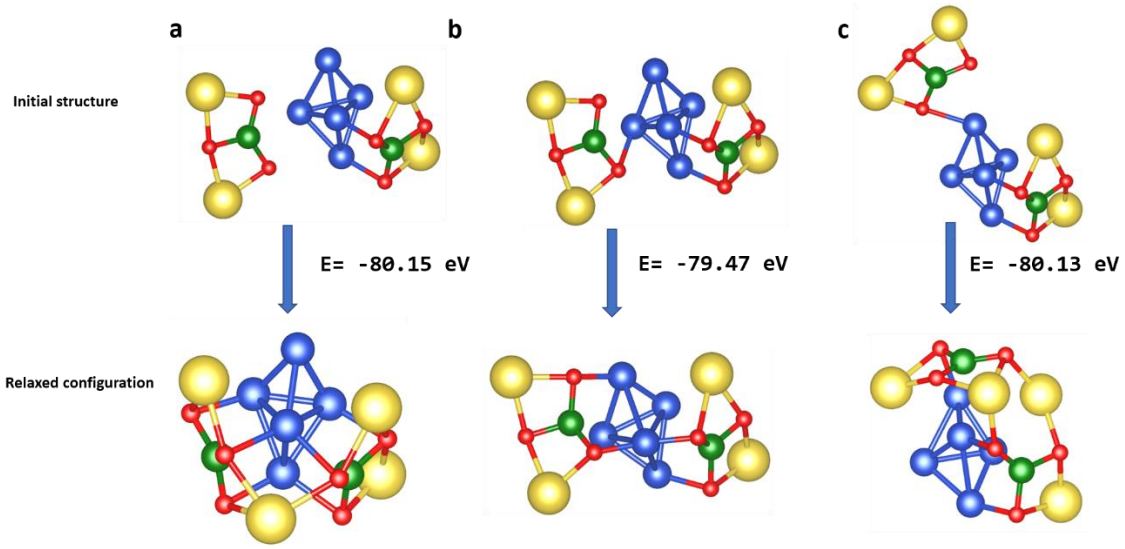

Figure 27 Configurations and total energy of SiO_3^{2-}adsorbed on a pyramidal Cu_5 cluster.

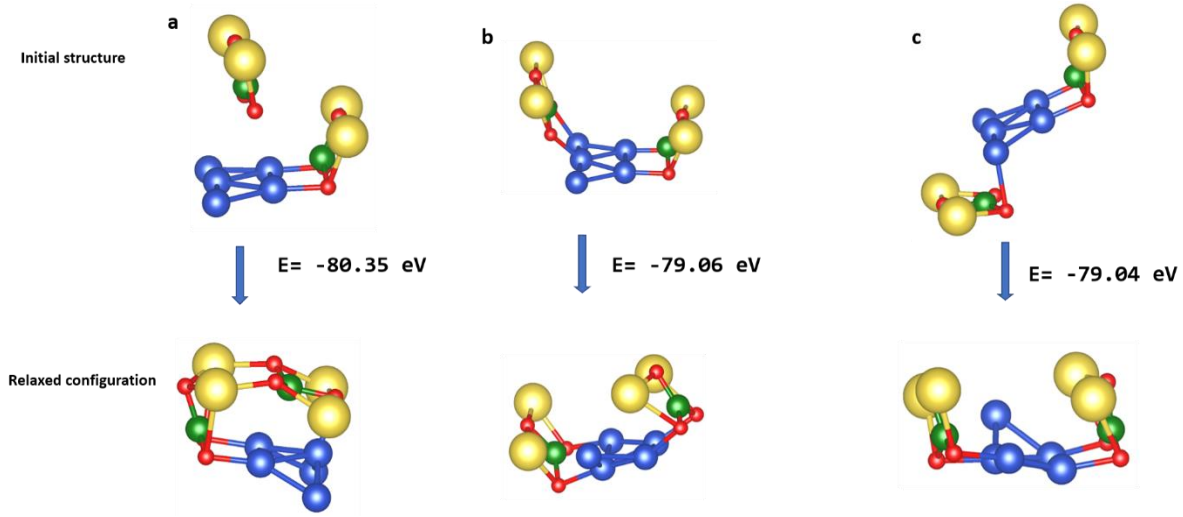

Figure 28 Configurations and total energy of SiO_3^{2-}adsorbed on a trapezoidal Cu5 cluster.

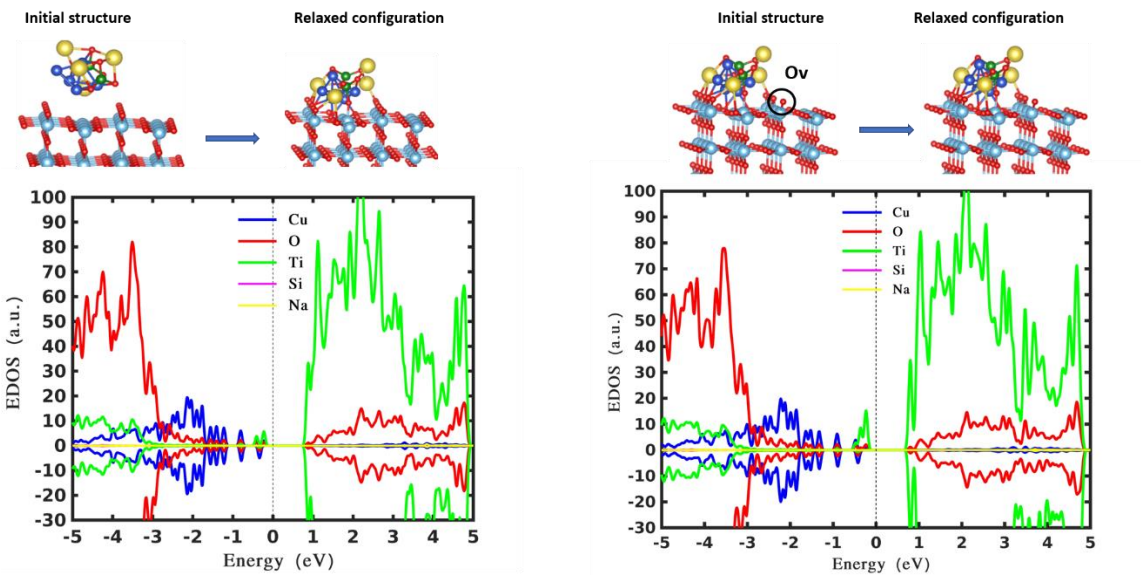

Figure 29 Configurations of pyramidal Cu_5/ SiO_3^{2-} deposited on perfect (a) and reduced (b) rutile TiO_2(110), and the corresponding density of states. The green, red and blue curves represent the states located on Titanium, oxygen, and copper atoms. Bader charge analysis reveals that 1.3 electrons (a) and 1.3 electrons (b) are transferred from Cu_5 to the support. The dashed line indicates the Fermi energy level of 0 eV.

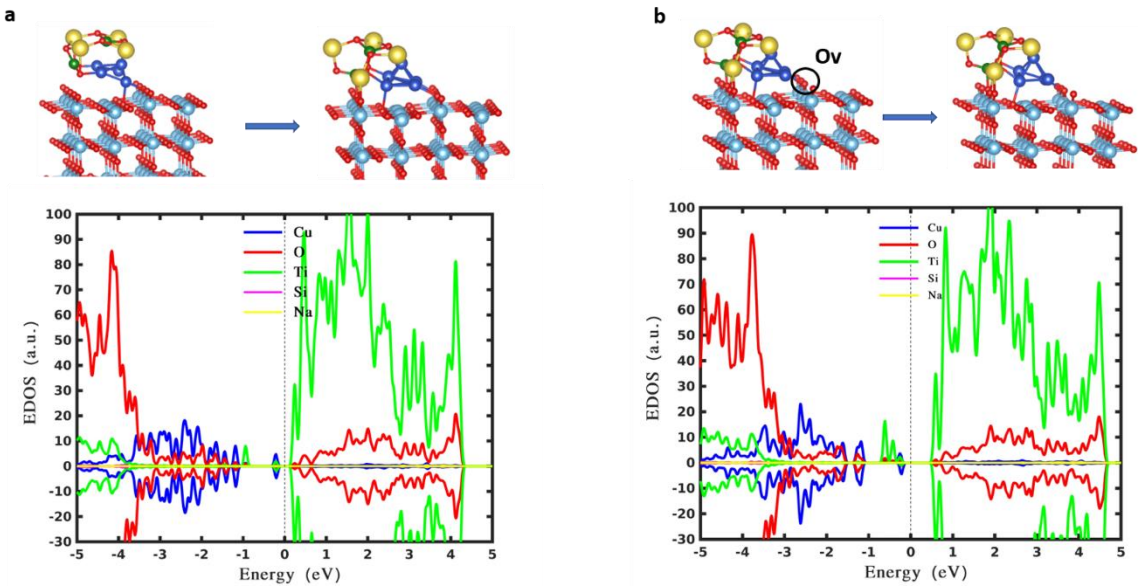

Figure 30 Configurations of pyramidal Cu_5/ SiO_3^{2-} deposited on perfect (a) and reduced (b) rutile TiO_2(110), and the corresponding density of states. The green, red and blue curves represent the states located on Titanium, oxygen, and copper atoms. Bader charge analysis reveals that 1 electron (a) and 0.8 electrons (b) are transferred from Cu_5 to the support. The dashed line indicates the Fermi energy level of 0 eV.

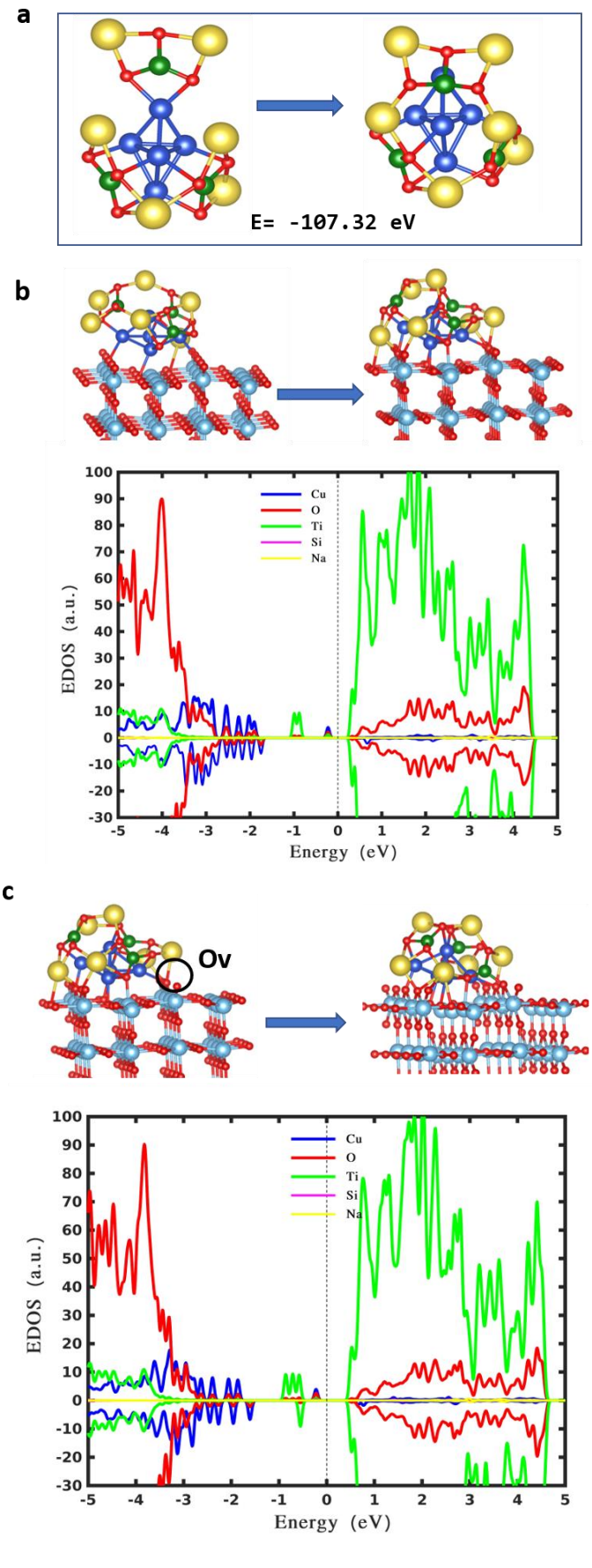
a
E= -107.32 eV
b
Cu
O
Ti
Si
Na
EDOS (a.u.)
Energy (eV)
c
Ov
Cu
O
Ti
Si
Na
EDOS (a.u.)
Energy (eV)

Figure 31 Configurations of pyramidal Cu_5/SiO_3^{2-} (a) deposited on perfect (b) and reduced (c) rutile TiO2(110), and the corresponding density of states. The green, red and blue curves represent the states located on Titanium, oxygen, and copper atoms.

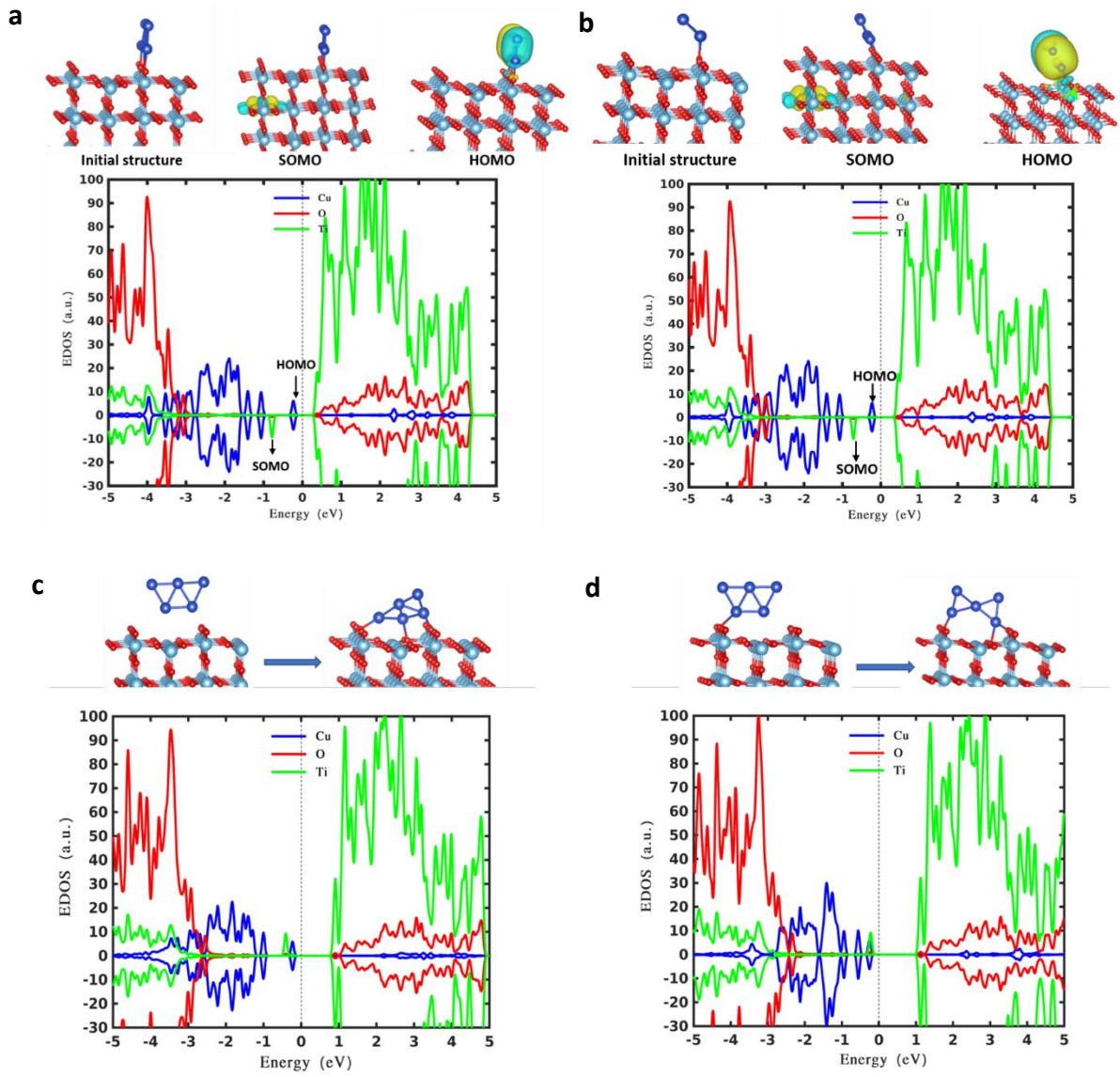

Figure 32 Wavefunctions of trapezoidal (a), and tilted trapezoidal (b) Cu_5 cluster deposited on rutile TiO_2 (110) surface, and their corresponding spin densities of states. The SOMO and HOMO wavefunctions are presented in the top panels (HOMO: highest occupied molecular orbital). The green, red and blue curves represent the states located on titanium, oxygen, and copper atoms respectively. Bader charge analysis reveals that 0.8 electrons (a), 0.79 electrons (b), 0.87 electrons(c), and 0.8 (d) electrons are transferred from Cu_5 to the support. The dashed line indicates the Fermi energy level of 0 eV.

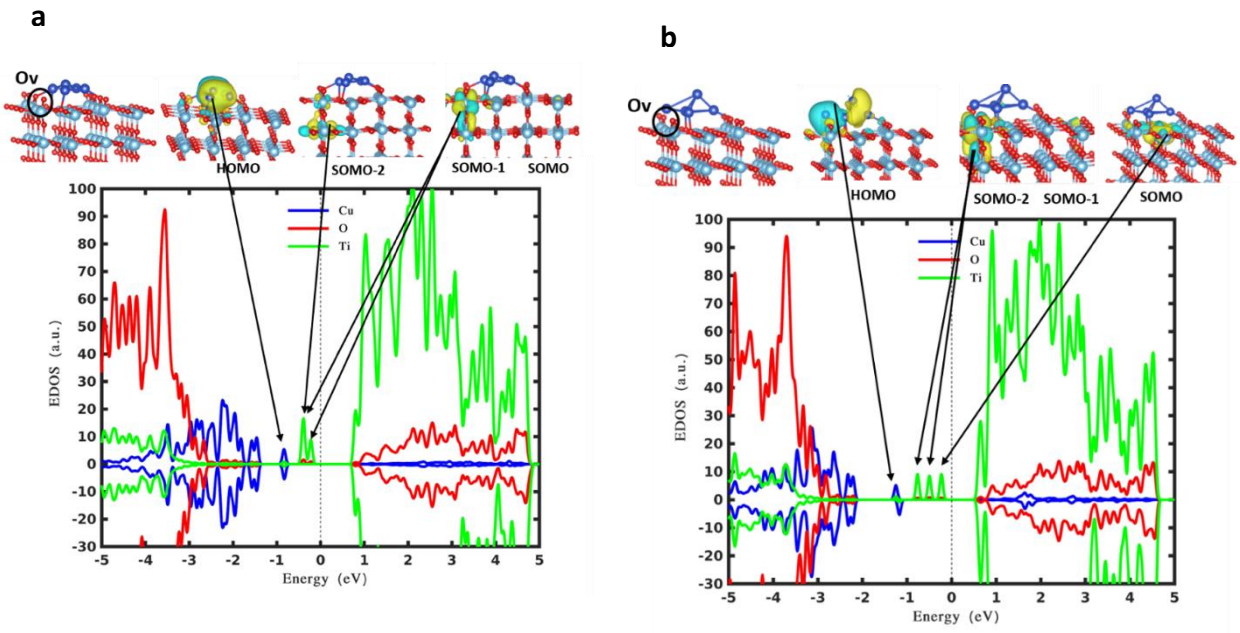

Figure 33 Wavefunctions of trapezoidal (a), and pyramidal (b) Cu_5 cluster deposited on reduced rutile TiO_2(110) surface, and their corresponding spin densities of states. The SOMO and HOMO wavefunctions are presented in the top panels (HOMO: highest occupied molecular orbital). The green, red and blue curves represent the states located on titanium, oxygen, and copper atoms respectively, while the two green peaks between −1 ~ 0 eV stand for the polaronic states located on one 5-fold coordinated Ti3+(3d) atom in the surface and one 6-fold coordinated Ti3+(3d) in the subsurface. The dashed line indicates the Fermi energy level of 0 eV.

4.4 CONCLUSION

In this study, I have carried out DFT calculations to understand the effects of adsorbing AQCs on perfect and reduced rutile TiO_2 in the presence and absence of SiO_3^{2-}. The geometric properties, wavefunctions, and their corresponding spin density of states of each relaxed structure were calculated. It is concluded that the adsorbed AQCs serve to reduce the bandgap in the stoichiometric as well as reduced TiO_2 substrates by introducing polaronic states in the band gap and those gap states sitting on Cu cluster can shift the solar absorption from ultraviolet to the visible region. Both pyramidal and trapezoidal Cu AQCs are oxidized by donating one or two electrons to the substrate. The polarons induced by charge transfer from AQCs to the substrate can persist in the presence of oxygen vacancies and even coexist with those created by the Ov. It is also found that the reduced surfaces behave like a negative gate to the AQC and gate the states sitting on the Cu out of the valence band and exist in the band gap. This means the enhancement of the photocatalysis due to oxygen vacancies can be interpretated from at least three aspects: one is the polaron states created by Ovs; second, Ovs behave like a negative gate to the states located on the AQCs; third, Ovs enhance the adsorption of adsorbates. Furthermore, a high-energy HOMO in the vicinity of the conduction band is obtained, indicating the presence of active sites on the Cu_5 cluster, which will easily donate electrons to a proton to promote the hydrogen evolution reaction (HER). In addition, my results also demonstrate that the presence of SiO_3^{2-} will not reduce the gap states and even enhance the gap states for some geometric structures by providing a negative gating to the AQCs. This demonstrates that the by-product during the purification process with silicate ions as precipitants will not destroy the photo absorption ability of Cu_5 AQC/support and could even enhance it.

5 CO_2 reduction improved by Cu_5 on Cu (111) compared to the pristine Cu surface

The electrochemical reduction of CO_2 on copper (Cu) surfaces has attracted a lot of attention because of its exceptional selectivity toward desired products and ideal reaction conditions. DFT computations are utilized in this work to elucidate the complex mechanics behind different types of reaction pathways on both pristine and defect-rich Cu (111) interfaces: formic acid and CO. The effects of surface properties, including surface index, shape, and crystallinity, are methodically investigated, with particular attention to the role of Cu_5 atomic quantum clusters (AQCs) as defect sites. The synthesis of formic acid (HCOOH) and CO from the intermediates COOH and HCOO is explained by the suggested energy diagram, which also shows that the presence of Cu_5 significantly lowers the energy barriers for the formation of *HCOO and COOH intermediates. This lower energy barrier improves the production's activity, demonstrating Cu_5's potential as a surface modification to maximize catalytic performance. The results of this study not only enhance our comprehension of CO_2 reduction on Cu surfaces, but also offer a useful method for creating better catalysts through the strategic use of Cu_5 clusters to create more active sites on the Cu (111) surface.

5.1 INTRODUCTION

Carbon dioxide is a potentially plentiful carbon resource on the planet. It is also a greenhouse gas, with its atmospheric concentration steadily growing over the last two centuries contributing up to 75.4% of the overall greenhouse effect [238]. So, there is an urgency for developing efficient technologies aimed at carbon capture and storage[239-243]. Consequently, there is a proposition that CO_2 could serve as a potential feedstock, enabling the economic production of essential commodity chemicals and hydrocarbon fuels [244]. As an alternate to carbon capture and storage (CCS), the idea of carbon capture and utilization (CCU) is garnering more interest [245, 246]. CCU entails the capture of CO_2 and its transformation into valuable chemicals, all achieved without relying on petrochemical feedstocks [247]. As CO_2 is thermodynamically very stable, efficient catalysts are required for its activation[248]. Several methodologies for catalyst design have been developed, including modifying the morphology[249, 250], oxidation state[251, 252], alloying [253, 254], and manipulating the surface facets of the catalyst [255]. Among many homogeneous and heterogeneous catalysts, Cu-based materials have received particular attention due to their high activity in CO_2 reduction among all other transition metals and having low cost [256-266]. Various products are formed on the electrochemical reduction of CO_2, such as CO, formic acid (HCOOH), methane (CH_4), and ethylene (C_2H_4)[267-269]. Nevertheless, a complex array of resulting compounds and high overpotentials have imposed restrictions on its practicality. Extensive efforts have been committed to finding copper-derived substances capable of electrocatalyzing the CO_2 reduction reaction (CO_2RR) with greater efficacy.

The primary goal is to lower the overpotentials and increase the selectivity of CO over its counterparts, namely H_2 and HCOOH. More specifically, the distinguishing characteristic of copper (Cu) is believed to stem from its ability to exhibit a moderate adsorption capacity

towards *CO intermediates. This moderate adsorption retards the desorption kinetics of *CO species from the copper surface, leading to their prolonged residence time. Furthermore, it establishes an environment conducive to *CO, with a moderate activation energy barrier on the Cu surface [270]. As a consequence, *CO can engage in dimerization reactions with other C_1 intermediates or undergo coupling reactions with other *CO molecules, culminating in the formation of larger C_2 products. In the ongoing scientific investigations, researchers are focused on devising methodologies to enhance the *CO binding ability by incorporating a second metal species, such as Au, Ag, or Zn, into the system or by introducing defects onto copper surface [271-274].

For a long time, electrochemical reactions for CO_2 reduction faced obstacles due to the absence of real-time characterization techniques capable of directly monitoring these processes at the electrode/electrolyte interface. CO_2 reduction reaction (CO_2RR) mechanisms were speculated to be based on limited experimental data on reaction kinetics. The proposed reactions were examined and rationalized by quantum chemical calculations[267, 275-281]. Recently, Cheng et al. employed ab initio molecular dynamics (AIMD) simulation to investigate the pathways for CO* and HCOO* formation on the surface of Cu(100) [279]. Their findings suggested that $^{*}CO_2^{\delta-}$ may serve as an intermediate in the formation of CO, whereas a proton-coupled electron transfer (PCET) mechanism is involved in the formation of $HCOO^-$. Research using computational techniques has fit very well, and however, gaining insights into the electrochemical CO_2 reduction mechanism remains essential, as well as the development of efficient catalytic materials [267, 282, 283]. In different metal structures, the way a catalyst works can be quite different depending on how its atoms are arranged and how its surface is shaped [284, 285]. Copper (Cu), for example, has a specific arrangement called a face-cantered cubic (FCC) structure. These various orientations affect how the catalyst behaves and its efficiency in reactions [286, 287]. The CO_2RR on Cu-based catalysts encompasses multiple

reaction pathways that are influenced by operating and catalyst surface conditions, resulting in diverse chemical products [275, 288-290]. Notably, Hori et al. [291] reported significant yields of C_2H_4 and CH_4 on Cu (100) and Cu (111) surfaces, respectively. Additionally, Takahashi et al. [292] and Hori et al. [293] demonstrated the production of CH_4, C_2H_4, and CH_3COOH using a series of single-crystal Cu-based electrodes. Concerning alloy catalysts, Vasileff et al. [289] categorized the properties of alloying metals based on their relative affinities for hydrogen and oxygen compared to Cu. It was observed that CO_2RR selectivity improved with bimetallic catalysts based on Cu with alloying metals. For instance, a Cu-Au alloy exhibited lower oxygen and hydrogen affinities than Cu, inhibiting the CH_4 pathway. By employing DFT to compute the free energies associated with various reaction paths of CO_2 reduction on the Cu (111) facet, Nie et al. discovered that the activation energies for the formation of *CHO and *COH from *CO at -1.15V vs. RHE were 0.39 and 0.21 eV, respectively [277, 294]. Consequently, *COH emerged as the crucial intermediate in the production of CH4 on Cu (111) following the pathway *CO → *COH → *C → *CH → *CH2 → *CH3 → CH4 [295]. Lim et al. [296] and Shin et al. [297, 298] further supported these studies. Xiaowa et al. presented the formation of ethylene and methane on Cu(111) facets through carbon monoxide reduction with methylidyne as an intermediate [299]. Methane forms when COH is reduced to C followed by hydrogenation, whereas ethylene competes with methane in the same pathway depending upon H and CH_2 coverages.

In this study, I have investigated the d reduction of CO_2 on the active sites of Cu (111) surface to understand the mechanism behind the chemical reaction. All the calculations are performed by using spin-polarized DFT. I investigated the CO_2RR mechanism through two pathways i.e., HCOOH and CO pathways to study the Gibbs free energy for the paths leading to Formate or formic acid, CO, to see which one is favoured on pristine Cu (111) and defective (containing Cu_5 clusters) Cu (111) electrode.

5.2 COMPUTATIONAL METHODS

In this study, we used the Vienna ab initio simulation program (VASP) to perform all of the DFT computations with a periodic slab model [219-221]. The D3 technique of Grimme incorporates Van der Waals corrections from Spin-polarized Perdew, Burke, and Ernzerhof (PBE) along with Becke-Jonson damping function to precisely determine binding or adsorption energies along with the geometrical optimizations [209]. Interactions between valence electrons and the ion core of copper, oxygen, carbon, and hydrogen are described through the projector augmented wave (PAW Method) method[156, 222] using the Spin-polarized DFT approach. Using the basis set of plane wave types with a cut-off energy of 500 eV, the wavefunctions of Kohn-Sham were further extended. The Brillouin zone is sampled using a gamma (1 × 1 × 1) point. Using coordinates derived from the experimental copper lattice constant (3.61491), the Cu (111) surface was modelled [300].

I constructed the Cu (111) surface consisting of four atomic layers in a 4 × 4 (16 atoms per layer) surface unit cell. A vacuum layer of ~20 Å was introduced perpendicular to the surface to avoid the interactions of the periodically repeated surface models. Using VESTA, the atomic-scale structures were shown (see **Figure 34**).

In thermodynamic simulation, the zero-point vibrational energy (E_{ZPE}), and vibrational entropy (TS) correct the free energies[301]. Vibrational frequency analysis was used to calculate the zero-point energies and entropy contributions to the free energies at room temperature (298.15 K) through the VASPKIT code [302]. The free energy of the electrochemical system is calculated according to the expression[195],

$$G = E_{DFT} + E_{ZPE} - TS \qquad 5\text{-}1$$

E_{DFT} donates the electronic energy computed with DFT, while E_{ZPE} and TS denote the total vibrational zero-point energy and entropic effect, respectively.

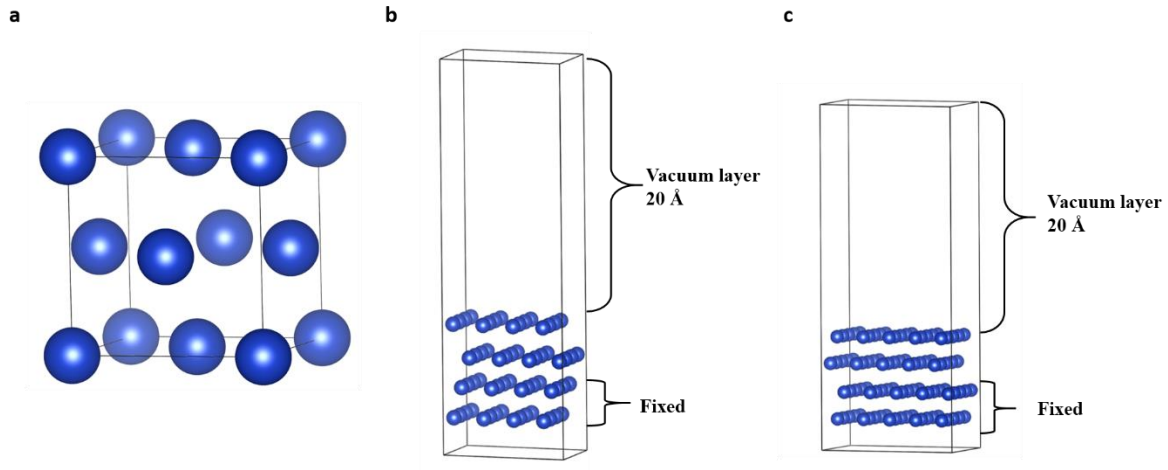

Figure 34 Optimized structures of (a)conventional Cu unit cell, and Cu (111) surface slap model 4 × 4 supercell(b) 5 × 5 supercell (c). The Cu atoms in the bottom two layers are fixed in the simulation.

5.3 RESULTS AND DISCUSSION

The optimized structures of CO_2, CO, H_2O, H_2, and HCOOH in the gas phase are shown in Figure 35. A linear structure was observed in CO_2 with a bond length of 1.17 Å between the carbon (C) and oxygen (O) atoms, while in HCOOH, the bent structure was obtained with an ∠H-C-O (formyl group) angle of 125.5°, ∠C-O-H (hydroxyl group) angle of 107° and core C=O bond length of 1.2 Å. These structures closely match experimentally reported C=O bond lengths for both CO_2 (1.16 Å) and HCOOH (1.23 0.03 ± Å) [303, 304].

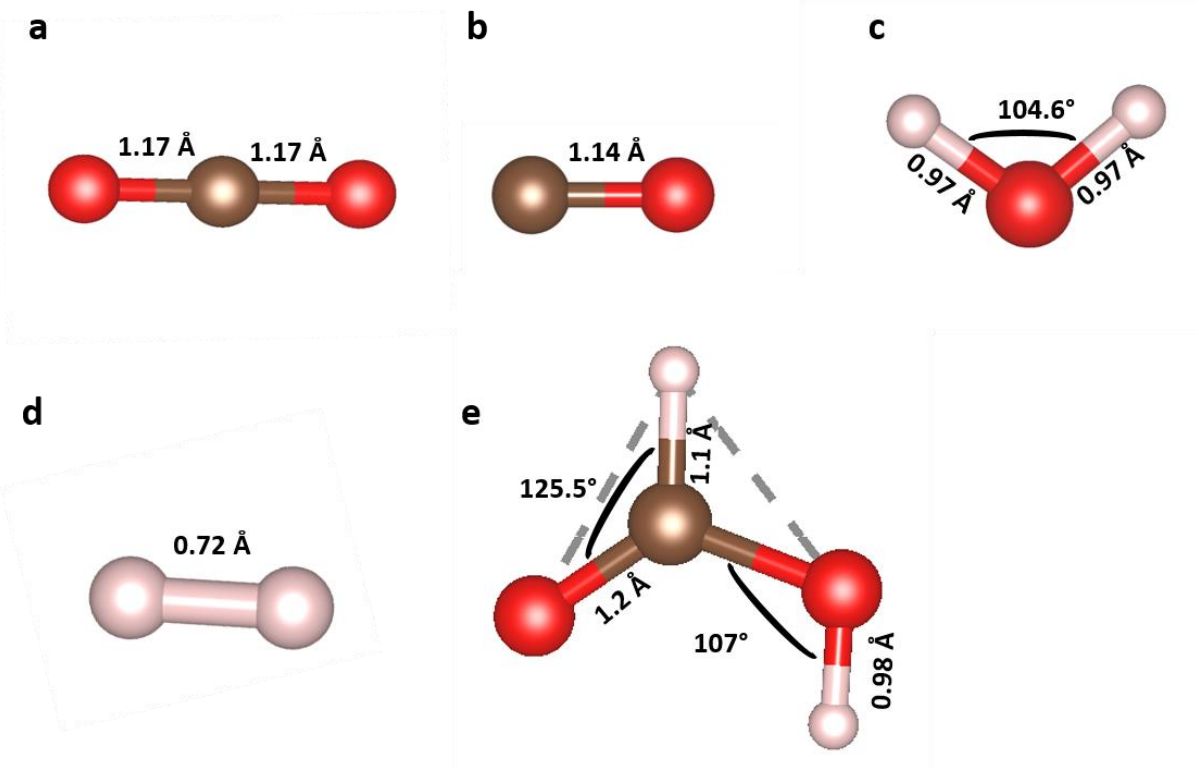

Figure 35 Optimized structures of gaseousCO_2 (a), CO(b), H_2O(c), H_2(d), and HCOOH(e). The white, red, and brown spheres indicate hydrogen, oxygen, and carbon, respectively.

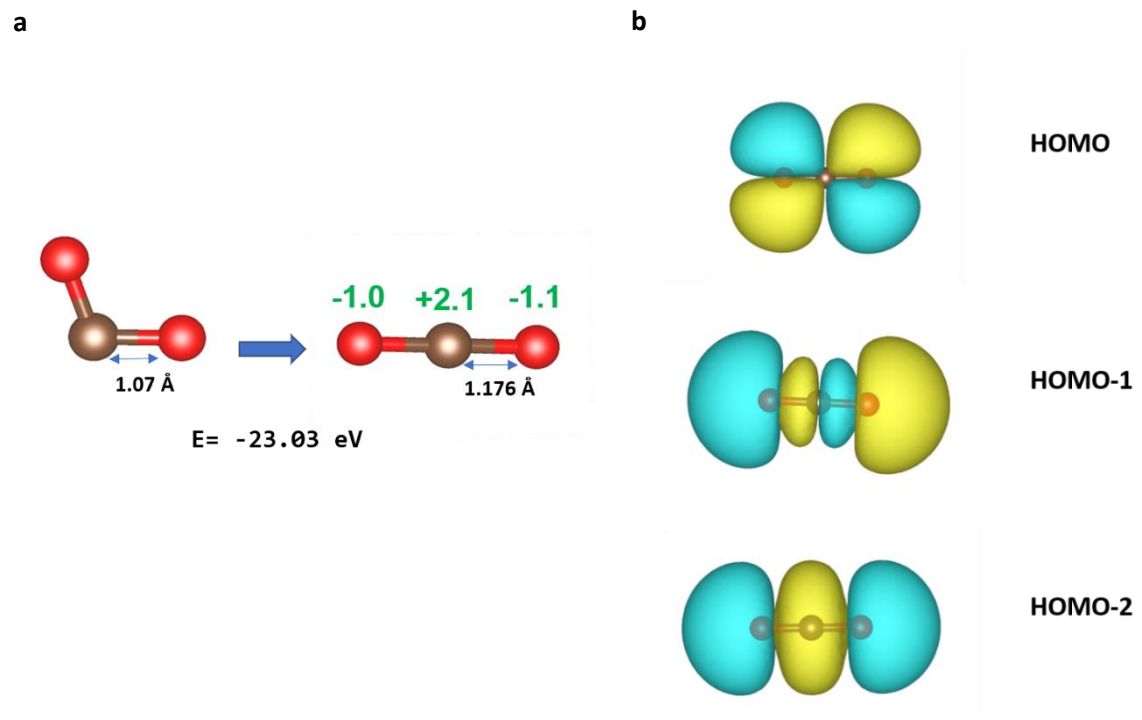

Figure 36 Initial and optimized structure of gaseous CO_2(a) with their corresponding wavefunctions (b). The green number displays the net (excess) charges on each atom. The red and brown spheres indicate oxygen, and carbon, respectively.

5.3.1 CO_2/Cu_5 Structure

I investigated the interaction mechanism of the CO_2 molecule with the pyramidal and trapezoidal Cu_5 AQC by exploring its geometric optimization and electronic properties, including adsorption energy and charge transfer. I considered different positions of CO_2 around both pyramidal and trapezoidal Cu_5 clusters to find the most stable structure (see **Figure 37 and Figure 38).**

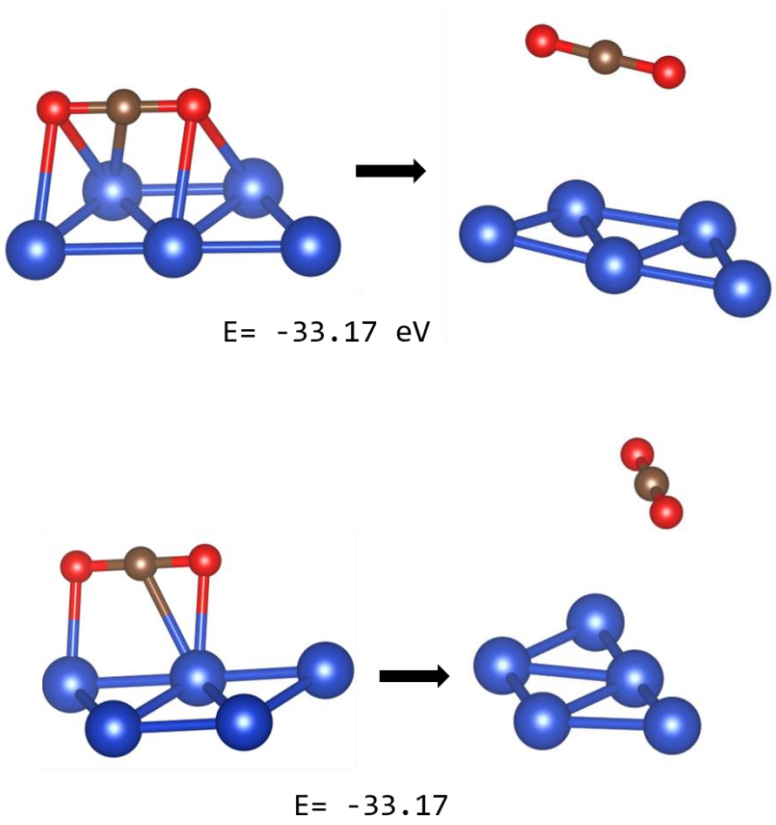

Figure 37 Initial (a) and optimized (b) of the CO2/Cu5. The red and brown spheres indicate oxygen, and carbon, respectively.

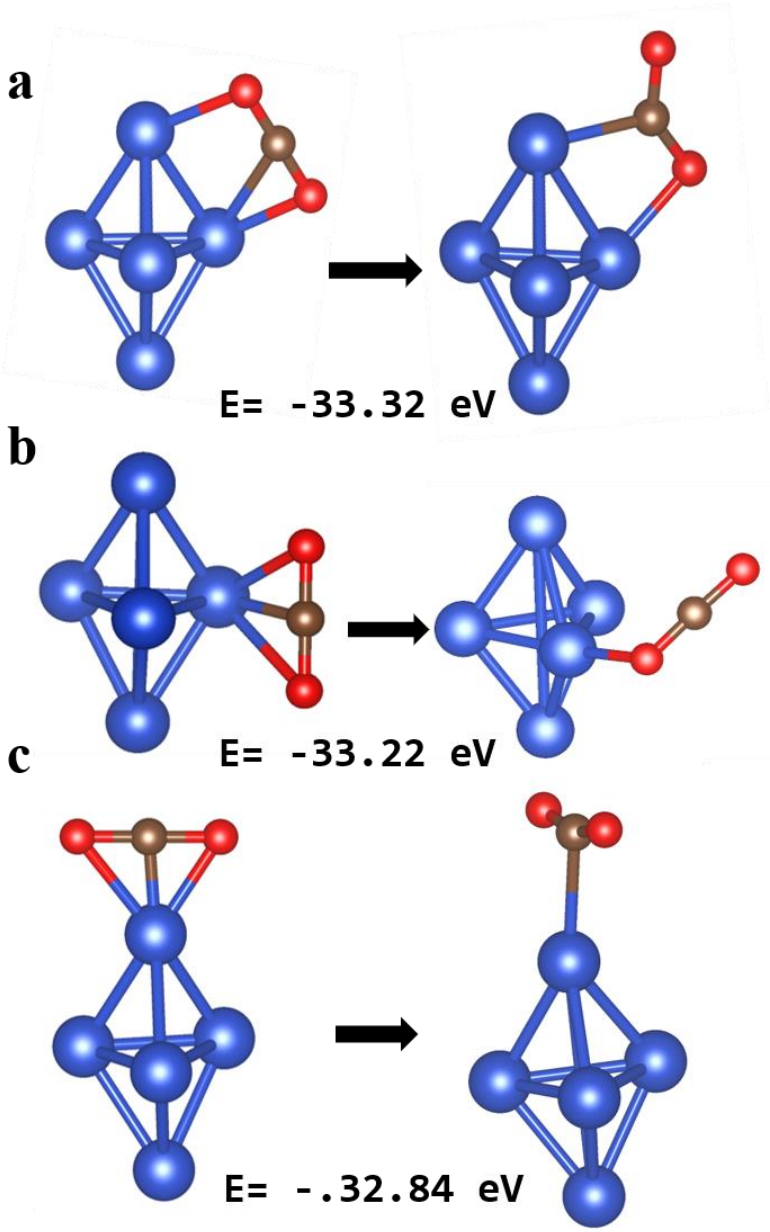

Figure 38 Initial (a) and optimized (b) of the CO2/Cu5. The red and brown spheres indicate oxygen, and carbon, respectively.

The initial and optimized structures of the most stable configurations of CO_2/Cu_5 for both structures are presented in **Figure 39**. It is found that the CO_2 molecule was physisorbed to the trapezoidal and pyramidal Cu_5 cluster with an adsorption energy of −0.68 eV and -0.54 eV respectively. This means that CO_2 binds more strongly to the trapezoidal than pyramidal. **Figure 39** clearly shows that in the two structures, the CO_2 molecule was bent and connected with two copper atoms after optimization, with a bond length of around 2.0 **Å** of the Cu-C bond

(see **Figure 39** and **Table 3**).To investigate the charge transfer between the Cu_5 AQC and the CO_2 molecule, I conducted Bader charge analysis calculations[183] [38]. The results of the Bader charge distribution revealed a charge donation from the copper cluster to the CO_2 molecule, amounting to approximately 0.6 e− from the trapezoidal and 0.5 e− from the pyramidal cluster. This charge transfer indicates that the cluster was oxidized.

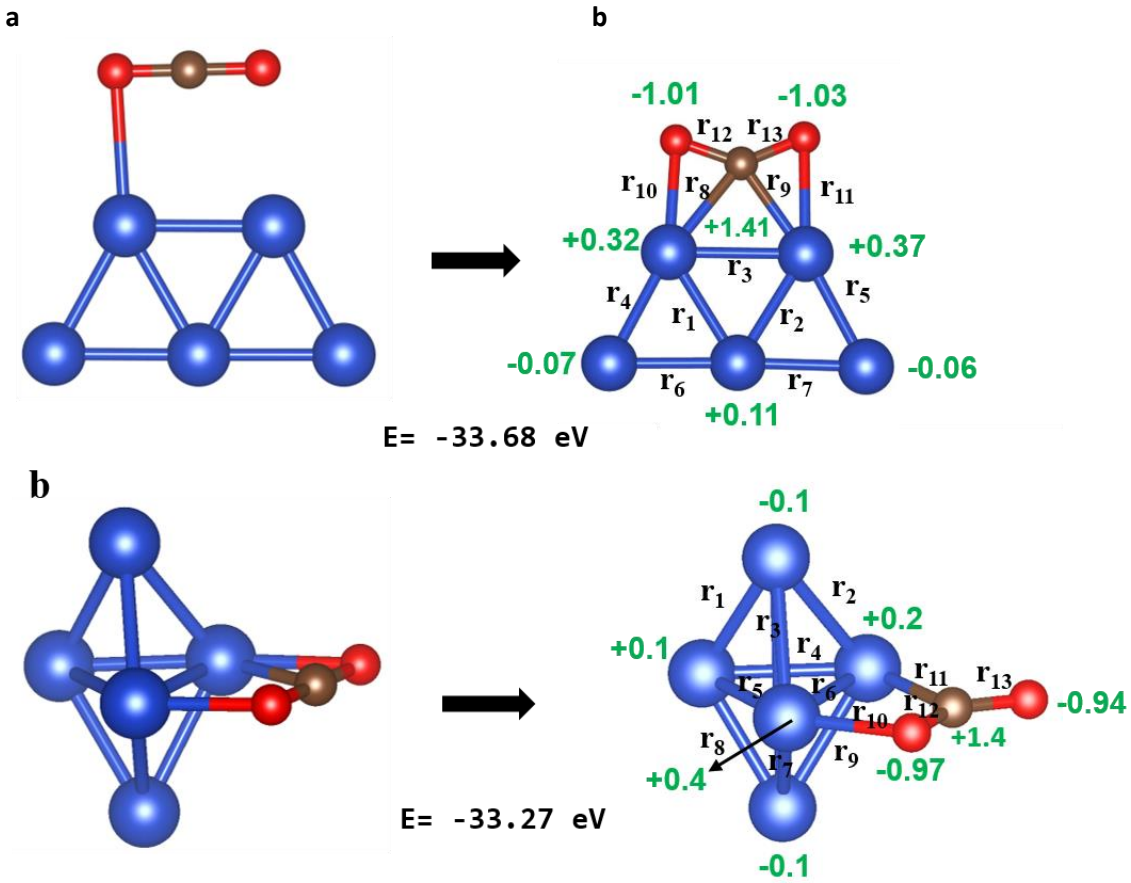

Figure 39 Initial and optimized of the most stable configurations of adsorbed CO_2 on trapezoidal (a), and pyramidal (b). The green number displays the net (excess) charges on each atom. The blue, red, and brown spheres indicate cupper, oxygen, and carbon, respectively.

Table 3 Bond lengths of CO_2/Cu_5 structure

Symbol	Bond length Trapezoidal CO_2/Cu_5 (Å)	Bond length Pyramidal CO_2/Cu_5 (Å)
r_1	2.36 Å	2.36 Å
r_2	2.37 Å	2.44 Å
r_3	2.48 Å	2.49 Å
r_4	2.34 Å	2.49 Å
r_5	2.33 Å	2.34 Å
r_6	2.34 Å	2.34 Å
r_7	2.33 Å	2.48 Å
r_8	2.0 Å	2.36 Å
r_9	2.1 Å	2.46 Å
r_{10}	2.1 Å	2.0 Å
r_{11}	2.1 Å	2.03 Å
r_{12}	1.2 Å	1.26 Å
r_{13}	1.2 Å	1.2 Å

5.3.2 CO_2 adsorption on Cu (111)

Since CO_2 reduction routes begin with the adsorption of the reactants on the catalyst surface, the CO_2 adsorption parameters of the interfaces were first established. We considered different adsorption sites for CO_2 on Cu (111) as shown in **Figure 40a**. Before the relaxation, the original

orientation of CO_2 molecules is parallel to the surface plane. Because prior studies revealed that CO_2 molecules are adsorbed parallel to the surface of Cu (111), I chose this orientation [305-307]. I noticed the molecules are very marginally adsorbed on the Cu surface. The adsorption of CO_2 on various sites is depicted in **Figure 40**, we found that CO_2 is weakly adsorbed on the Cu surface, prefers adsorption in bridge sites, and is oriented perpendicular to the surface. For CO_2 in a bridge site, I obtained −0.22 eV adsorption energy with C–O and Cu–C interatomic distances of 3.6 and 1.17 Å, respectively, which is consistent with a previous DFT study[308, 309]. The adsorption energies of CO_2 are listed in **Table 4**.

Table 4 Adsorption energies (E_{ads}) and adsorption structures of CO_2 on Cu (111). The terms dC–O, and dC–Cu define the C–O bond length of adsorbed CO_2, and the interatomic distance between the nearest Cu and C atoms respectively.

Sites	**E_{ads} (eV)**	**$D_{C\text{-}O}$(A°)**	**$D_{C\text{-}Cu}$(A°)**
Top	**-018**	**1.17**	**3.1**
Bridge	**-0.22**	**1.17**	**3.6**
fcc	**-0.19**	**1.17**	**3.3**
hcp	**-0.19**	**1.17**	**3.3**

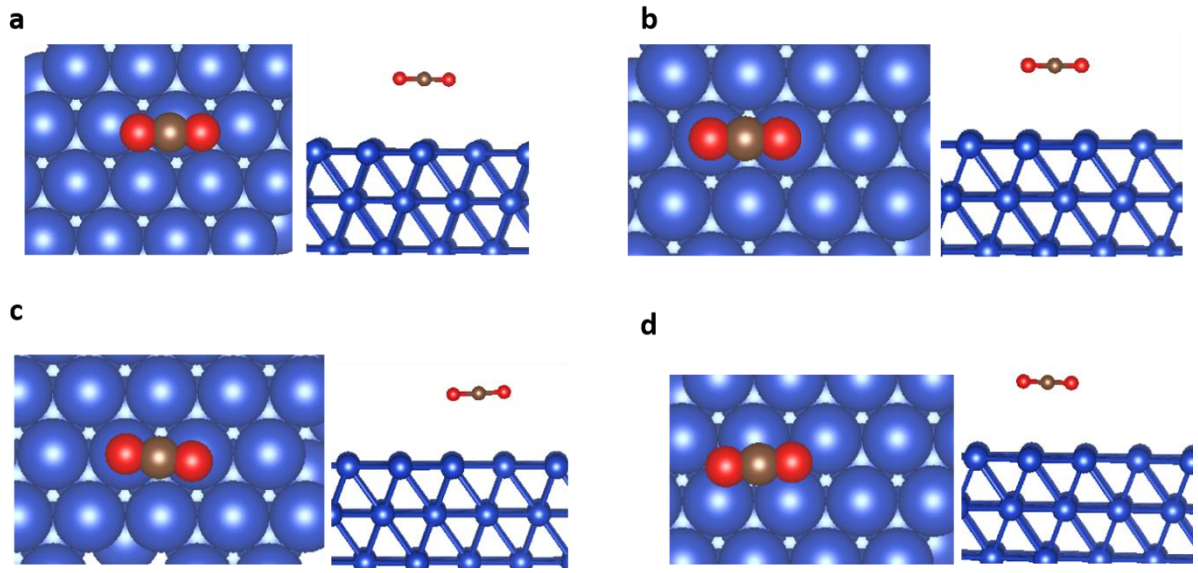

Figure 40 Top and side view of CO_2 on a) top, (b) bridge, (c) hcp hollow, and (d) fcc hollow adsorption structures on Cu (111). The blue, white, red, and brown spheres indicate copper, hydrogen, oxygen, and carbon, respectively.

5.3.3 Thermodynamic data and reaction pathways

5.3.3.1 Cu_5 cluster on Cu (111)

To investigate the geometrical stability of CO_2 on the Cu (111)/Cu_5 substrate, First, I deposited the optimized pyramidal and trapezoidal Cu_5 clusters on the surface of Cu (111) at different angles and positions. I found that the lying-down geometry was the most stable structure, as shown in **Figure 41a**, while the pyramidal Cu_5 was less stable (see **Figure 42**). Additionally, I calculated the total energies with respect to the different configurations created by depositing the CO_2 at different positions around the cluster on the Cu (111) surface (the most stable), as depicted in **Figure 43**. The results exhibit that structure 4 is the most stable configuration. In contrast, structure 2 is found to be the metastable structure.

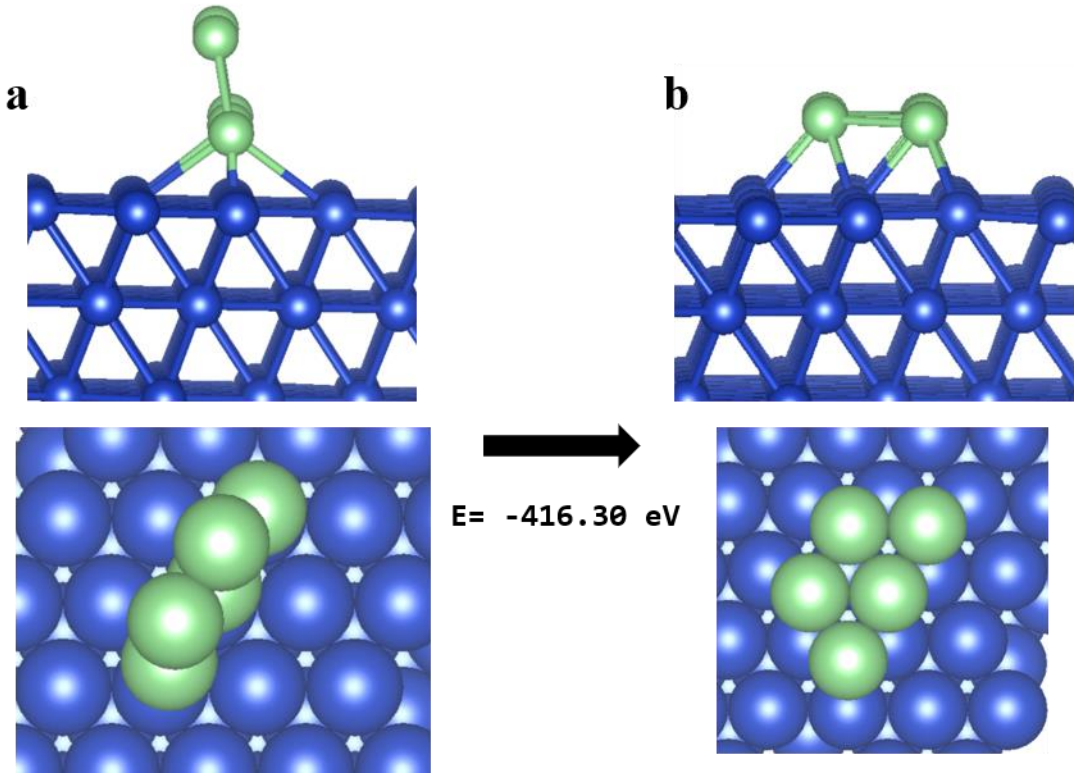

Figure 41 Initial (a), and optimized (b) Configurations of the trapezoidal Cu_5 cluster deposited on Cu (111) surface. The Blue balls represent Cu atoms, and the green are for the Cu_5 cluster atoms.

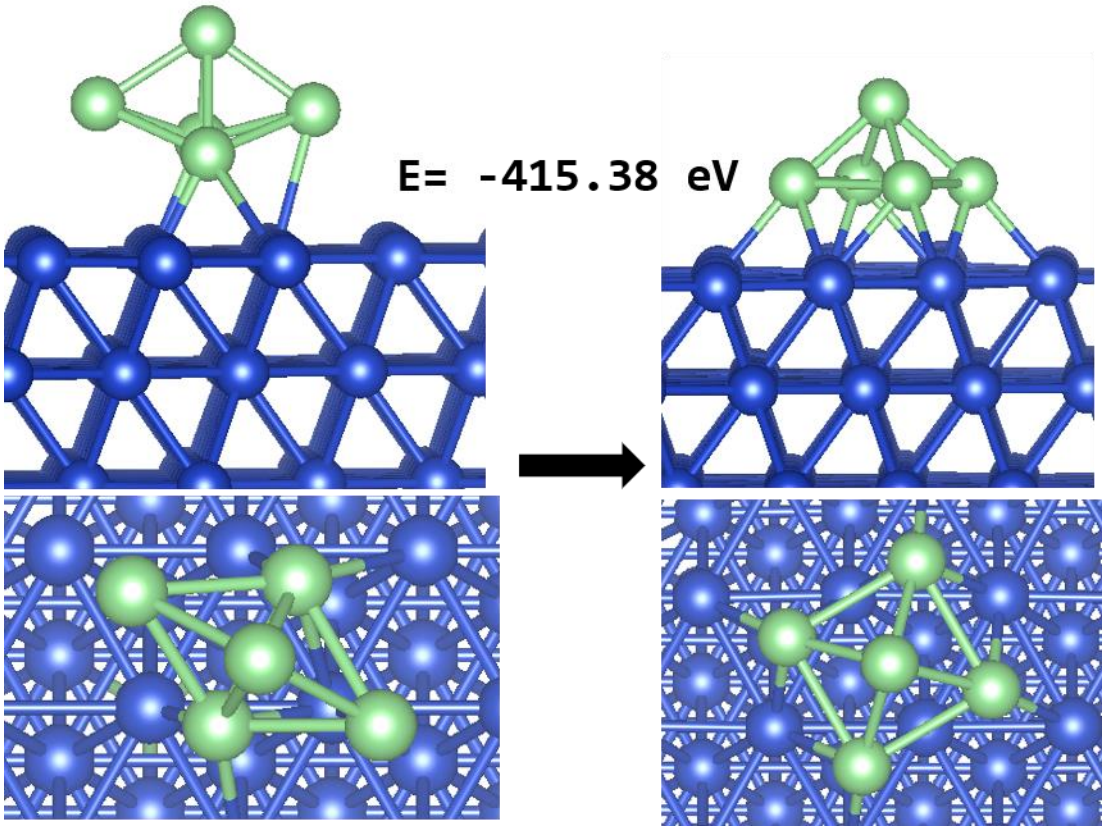

Figure 42 Initial (a), and optimized (b) Configurations of the pyramidal Cu_5 cluster deposited on Cu (111) surface. The Blue balls represent Cu atoms, and the green are for the Cu_5 cluster atoms.

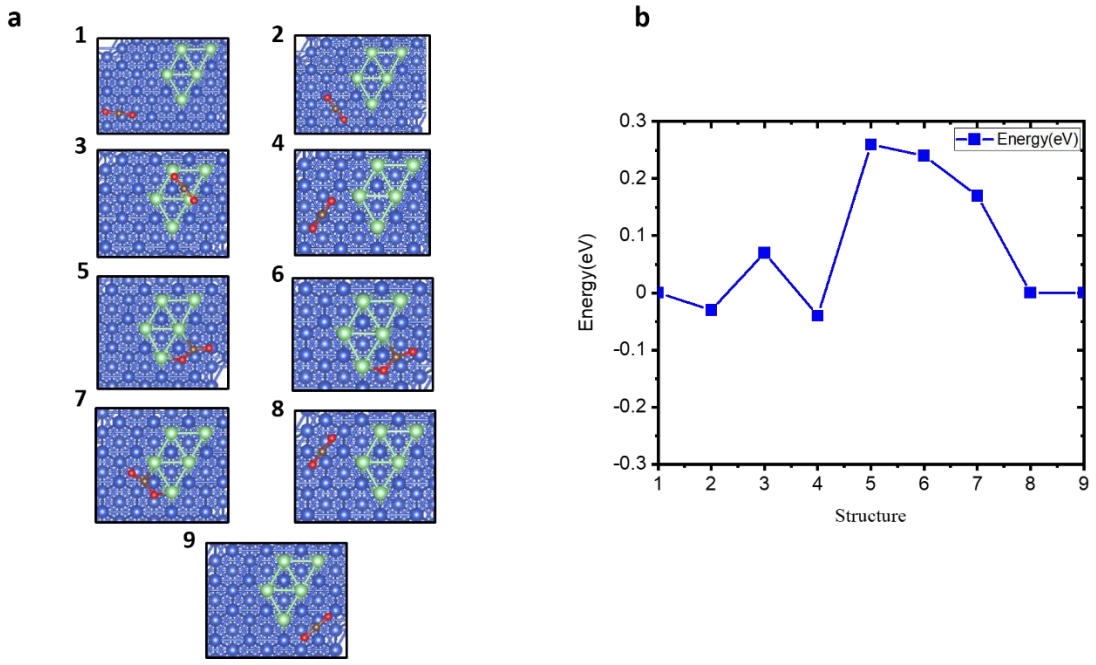

Figure 43 Configurations of CO_2 deposited on Cu (111) surface in the presence of trapezoidal Cu_5, the geometrically optimized configurations based on different positions (a), and energy evolution as the function of different positions of CO_2 (b). The Blue balls represent Cu atoms, the red ones are for O atoms, the brown ones for C atoms, and the green are for the Cu_5 cluster atoms.

5.3.3.2 CO pathway on a pristine and defective Cu (111) surface

The ground state geometry of neutral CO_2, a stable molecule, is a linear form. When neutral CO_2 goes through one-electron reduction, a CO_2 anion with bent CO_2 geometry is created[310]. Due to the bent conformation, CO_2 may become more reactive, and breaking the C-O bond can be one of the results[308, 310, 311]. It is thought that the activation of CO_2 to produce the bent structure is the first step in the electrocatalytic reduction of CO_2, and the transition from a linear

to bent geometry has a high reorganizational energy cost[263]. As a result, here we modelled both liner and pent CO_2 in both the CO and Formate pathway.

The reaction kinetics of the electrochemical reduction of CO_2 into CO on Cu (111) and Cu_5/Cu (111) surfaces are thoroughly examined in this section. I provide detailed free energy diagrams explaining the pathways for CO_2 reduction to CO, as shown in **Figure 44**, in order to thoroughly evaluate the effect of Cu_5 on the Cu (111) surface. To gain important insight into the catalytic mechanisms controlling the electrochemical reduction process, this systematic analysis attempts to disentangle the complex interactions between the modified Cu_5/Cu (111)interface and the pristine Cu (111) configuration. **Figure 44**a presents the reaction pathway configuration of the CO process on Cu (111) (top panel) and Cu_5/Cu (111) (bottom panel), while the graph in **Figure 44**b shows that the reduction of CO_2 to CO on Cu_5/Cu (111)compared to pristine Cu (111) demonstrates a significant improvement in catalytic performance. A more advantageous pathway for the formation of CO from the key intermediates (COOH*)[312] is indicated by the graph's lower energy barrier on Cu_5/Cu (111)at around 0.2 eV. The observed decrease in the energy barrier implies that the addition of Cu_5 clusters to the Cu (111) surface greatly improves the catalytic efficiency, possibly by affecting the activation and adsorption of COOH intermediates. The results highlight the beneficial interactions between Cu_5 clusters and the Cu (111) surface, providing a viable path toward the development of catalysts with higher CO_2 electroreduction activity. This realization may be crucial to the advancement of more effective and long-lasting electrocatalysts for the production of CO.

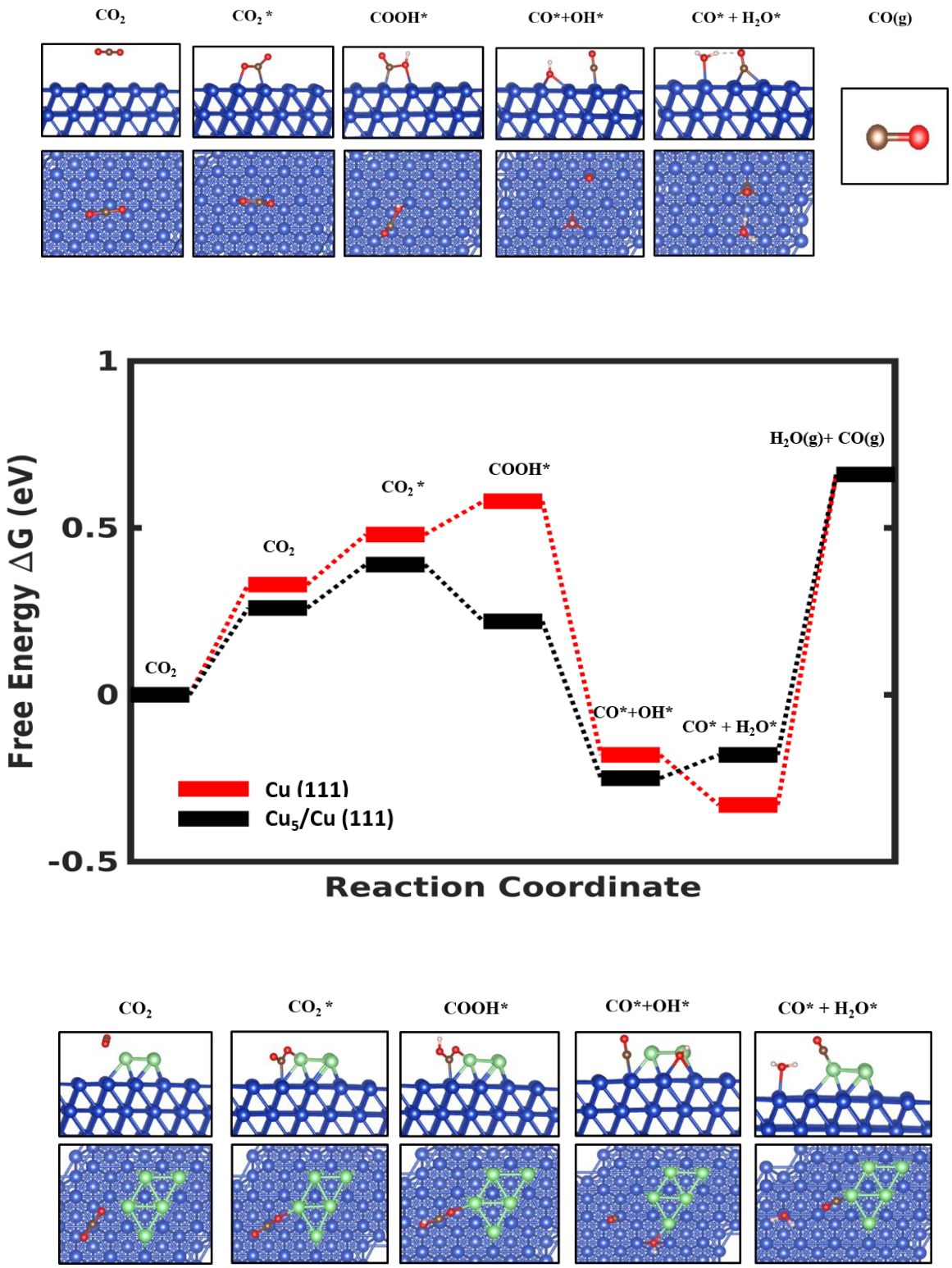

Figure 44. Optimized structures of the intermediates of CO_2 reduction to CO with and without Cu_5 (top and bottom panel). Gibbs free energy diagram of the reaction for CO_2 adsorption to CO via the (k) COOH* pathway on Cu (111) and Cu_5/Cu (111) (middle

panel). The Blue balls represent Cu atoms, the red ones are for O atoms, the brown for C atoms, the white for H, and the green are for the Cu_5 cluster atoms.

5.3.3.3 HCOOH pathway on a pristine and defect Cu (111) surface

Figure 45b shows the relative Gibbs free energy diagram for preferred CO_2 electroreduction into formic acid (HCOOH) on Cu (111) and Cu_5/Cu (111). With an emphasis on the critical intermediate HCOO—which is recognized for playing a critical role in the electrocatalytic reduction of CO_2 to formic acid (HCOOH) as demonstrated by earlier research (HCOO* → HCOOH → CO_2)[312, 313]—the Gibbs free energy diagrams that are displayed provide important information about the favored route for CO_2 electroreduction on Cu(111) and Cu_5/Cu (111)surfaces. The comparative study indicates that the Cu_5/Cu (111)composite has a clear advantage because the suggested mechanism has lower energy barriers. The lower energy barriers suggest a more energetically advantageous pathway for the formation of HCOOH, suggesting increased catalytic activity enabled by the addition of Cu_5 clusters to the Cu (111) surface. To sum up, the catalytic benefits of this composite are highlighted by the lower energy barriers found on Cu_5/Cu(111)for the preferred CO_2 electroreduction into formic acid (HCOOH) through the primary intermediate HCOO.

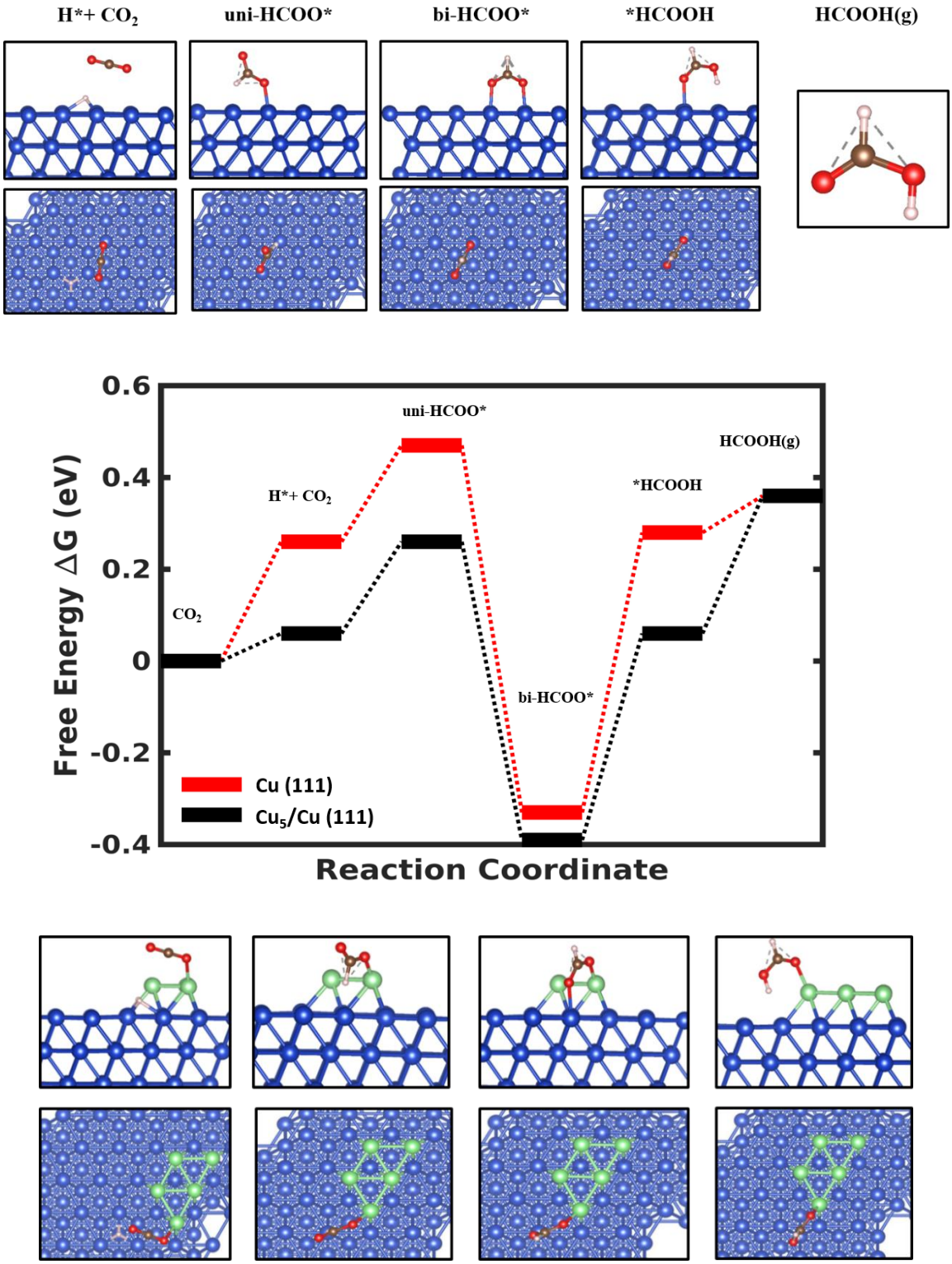

Figure 45 Optimized structures of the intermediates of CO_2 reduction to HCOOH with and without Cu_5 (top and bottom panel). Gibbs free energy diagram of the reaction for CO_2 adsorption to HCOOH via the (k) HCOO* pathway on Cu (111) and Cu_5/Cu (111)

(middle panel). The Blue balls represent Cu atoms, the red ones are for O atoms, the brown for C atoms, the white for H, and the green are for the Cu_5 cluster atoms.

5.3.3.4 Hydrogen evolution reaction (HER)

Despite the fact that CO_2 electrocatalytic reduction has been the subject of extensive investigation, there are still some difficulties with the electrochemical reaction. The primary competitive reaction to the electrochemical CO_2 reduction cycle is the hydrogen evolution reaction (HER) [314, 315]. Thus, developing and discovering electrocatalysts that can suppress the (HER) is a vital necessity in CO_2 electrocatalytic reduction research. In this section further calculating the free energy profiles of the H_2 evolution reaction (HER) provided.

A comparison of Cu_5/Cu (111) and Cu (111) shows a significant difference in the energy barrier for hydrogen (*H) adsorption (**Figure 46**,). In particular, the energy barrier of Cu_5/Cu (111) is -0.14 eV lower than that of Cu (111) (-0.31 eV). This finding implies that the hydrogen evolution process (HER) is not inhibited by the adsorption of *H on Cu_5/Cu (111), which is different from the HER on Ag_5/Ag(111) carried out by my colleague Bandar Alsuwayni. The reason for the different behaviours on different substrates will be investigated in my future work.

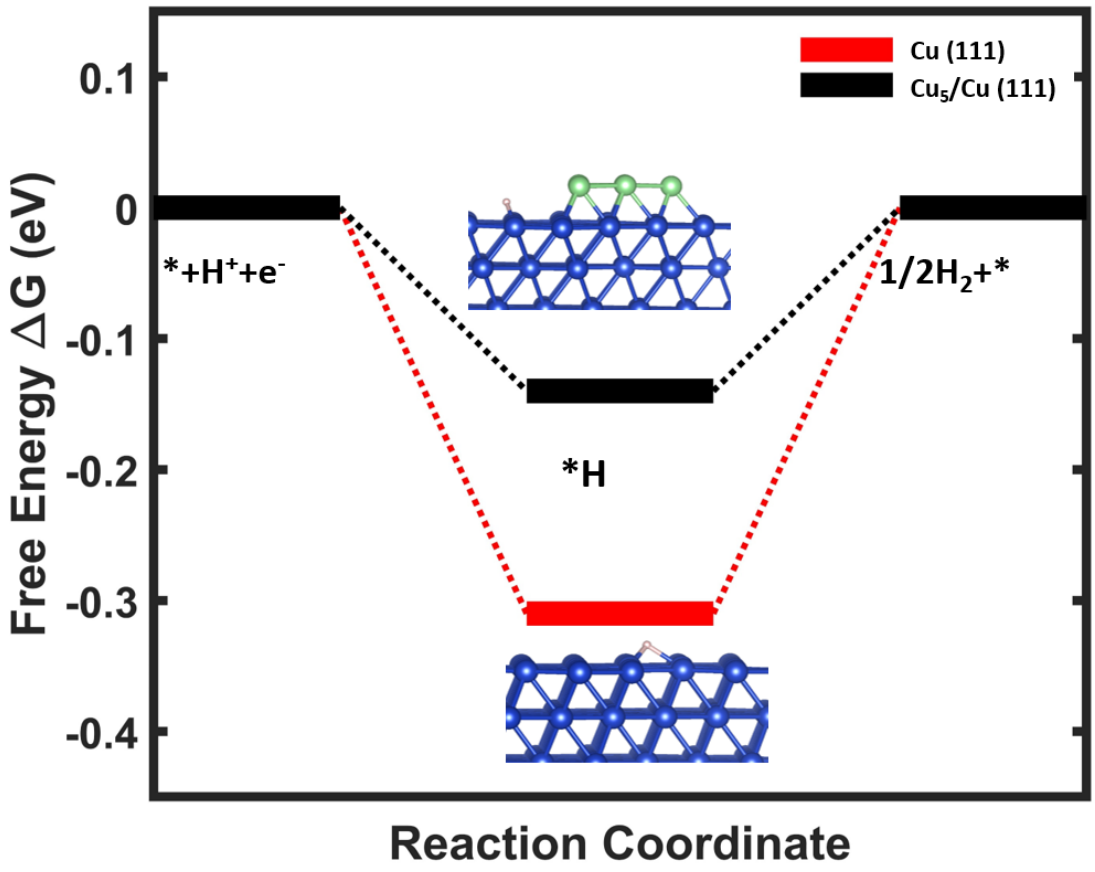

Figure 46 Free energy diagram of the HER on Cu (111) and Cu_5/Cu (111)with corresponding optimized structures of adsorbates.

5.4 CONCLUSION

In summary, the simultaneous investigation of CO_2 reduction to CO and formic acid (HCOOH) on Cu (111) and Cu_5/Cu (111) surfaces provides interesting new information about 'the catalytic capabilities of these materials. The observed decrease in energy barriers for both pathways on Cu_5/Cu (111) indicates a constant increase in catalytic activity relative to the unadulterated Cu (111) surface. This demonstrates the synergistic effects between the Cu (111) surface and Cu_5 clusters and implies that the inclusion of Cu_5 clusters onto Cu (111) plays a crucial role in lowering activation energies. The promising outcomes go beyond the generation of CO and include the reduction of CO_2 to formic acid, demonstrating adaptability of the catalyst Cu_5/Cu (111) to a wide range of electrochemical processes. Our understanding of catalytic mechanisms has been enhanced by these findings, which also provide a concrete path towards the development of highly effective and adaptable catalysts for the sustainable conversion of CO_2. Furthermore, compared to pristine Cu (111), Cu_5/Cu (111) exhibits lower energy barriers for the Hydrogen Evolution Reaction (HER), suggesting that *H adsorption on the Cu_5/Cu (111) interface will not suppresses HER. These findings further support the effectiveness of Cu_5/Cu (111) as an electrocatalyst for CO_2 reduction. This finding emphasizes potential of Cu_5 for influencing the electrocatalytic landscape and offers a useful path for the creation of catalysts that reduce CO_2 selectively while reducing unwanted side reactions like HER. The catalytic ability of Cu_5/Cu (111) shines as a lighthouse, suggesting novel paths toward effective electrochemical CO_2 conversion as we make our way through the confusing terrain of renewable energy options.

6 Summary and Future Work

The goal of this thesis is to use Cu_5 AQCs to increase the catalytic activity of various metal oxides in the direction of green energy. This thesis made use of VASP software and DFT combined with HF techniques. The effect of small trapezoidal and bipyramidal copper AQCs on the photocatalytic activity of perfect and defective rutile (110) TiO_2 surfaces in the presence and absence of silicate is the main topic of Chapter 4. It is discovered that these copper AQCs undergo oxidation, giving electrons to the substrates and causing a surface polaron to form inside the bulk band gap. Moreover, when Cu_5/ $SiO_3^{2-}$and an oxygen vacancy are present, hybrid states are found on copper atoms. To increase the photocatalytic activity of the metal oxides, these gap states are necessary. In the future, further investigations can be carried out on the energetics and kinetics of water splitting process on such surfaces.

In Chapter 5, CO_2 reduction on both perfect and imperfect Cu (111) interfaces is studied via DFT. The formate and CO pathways are investigated in the study, and Cu_5/Cu (111) is found to be a promising catalyst for CO_2 hydrogenation. Lower Gibbs free energy barriers for formate and CO production are demonstrated by the research on both surfaces, highlighting the catalytic enhancement of Cu_5 clusters.

Future studies could investigate a broader range of reaction pathways, such as the production of other valuable products, such as methane, ethylene, or other hydrocarbons, in order to better understand the catalytic performance of Cu_5/Cu(111) in CO_2 reduction. A deeper comprehension of the complex reaction mechanisms at play might be possible through the

application of more advanced computational techniques than DFT. Electrochemical studies play a critical role in experimentally verifying the theoretical predictions, thereby offering concrete proof of Cu_5/Cu (111)'s catalytic capabilities in a variety of reaction pathways. Furthermore, a more thorough examination of the stability and dynamic behavior of Cu_5 clusters during CO_2 reduction may provide insight into how long the catalyst will last in practical use. To gain more insight into the wider applicability and versatility of Cu5/Cu (111) as a catalyst for sustainable CO_2 conversion, it would be beneficial to investigate the impact of different reaction parameters, including temperature, pressure, and reactant concentrations. In addition, different sizes of AQCs could be investigated. These upcoming research paths seek to bridge the gap between theoretical predictions and real-world applications by aiding in the development of effective and adaptable catalysts for a variety of CO_2 reduction products.

7Bibliography

1. Chu, S. and A. Majumdar, *Opportunities and challenges for a sustainable energy future.* nature, 2012. **488**(7411): p. 294-303.
2. Zhao, G., et al., *Heterostructures for electrochemical hydrogen evolution reaction: a review.* Advanced Functional Materials, 2018. **28**(43): p. 1803291.
3. Yang, F., et al., *Boosting hydrogen oxidation activity of Ni in alkaline media through oxygen-vacancy-rich CeO2/Ni heterostructures.* Angewandte Chemie International Edition, 2019. **58**(40): p. 14179-14183.
4. Ross, M.B., et al., *Designing materials for electrochemical carbon dioxide recycling.* Nature Catalysis, 2019. **2**(8): p. 648-658.
5. Hemalatha, K., et al., *Function of nanocatalyst in chemistry of organic compounds revolution: an overview.* Journal of Nanomaterials, 2013. **2013**: p. 4-4.
6. Anastas, P.T. and J.C. Warner, *Green chemistry: theory and practice*. 2000: Oxford university press.
7. Rodríguez-Padrón, D., A. Puente-Santiago, and A. Balu, *Environmental catalysis: present and future. ChemCatChem 11: 18–38*. 2019.
8. Prinsen, P. and R. Luque, *Introduction to nanocatalysts.* Nanoparticle Design and Characterization for Catalytic Applications in Sustainable Chemistry, 2019. **38**: p. 1.
9. Zou, Y.-Q., et al., *Ethylene glycol as an efficient and reversible liquid-organic hydrogen carrier.* Nature catalysis, 2019. **2**(5): p. 415-422.
10. Birol, F., *The future of hydrogen: seizing today's opportunities.* IEA Report prepared for the G, 2019. **20**.
11. Armor, J.N., *The multiple roles for catalysis in the production of H2.* Applied Catalysis A: General, 1999. **176**(2): p. 159-176.
12. Zou, Z., et al., *Direct splitting of water under visible light irradiation with an oxide semiconductor photocatalyst.* nature, 2001. **414**(6864): p. 625-627.
13. Romano, V., et al., *Current density in solar fuel technologies.* Energy & Environmental Science, 2021. **14**(11): p. 5760-5787.
14. Kim, J.H., et al., *Toward practical solar hydrogen production–an artificial photosynthetic leaf-to-farm challenge.* Chemical Society Reviews, 2019. **48**(7): p. 1908-1971.
15. Hisatomi, T. and K. Domen, *Reaction systems for solar hydrogen production via water splitting with particulate semiconductor photocatalysts.* Nature Catalysis, 2019. **2**(5): p. 387-399.
16. Wang, Q. and K. Domen, *Particulate photocatalysts for light-driven water splitting: mechanisms, challenges, and design strategies.* Chemical Reviews, 2019. **120**(2): p. 919-985.
17. Wang, Y., et al., *Mimicking natural photosynthesis: solar to renewable H2 fuel synthesis by Z-scheme water splitting systems.* Chemical reviews, 2018. **118**(10): p. 5201-5241.
18. Wang, Z., C. Li, and K. Domen, *Recent developments in heterogeneous photocatalysts for solar-driven overall water splitting.* Chemical Society Reviews, 2019. **48**(7): p. 2109-2125.
19. Luo, S., et al., *Plasmonic photothermal catalysis for solar-to-fuel conversion: current status and prospects.* Chemical Science, 2021. **12**(16): p. 5701-5719.
20. Azwar, M., M. Hussain, and A. Abdul-Wahab, *Development of biohydrogen production by photobiological, fermentation and electrochemical processes: a review.* Renewable and Sustainable Energy Reviews, 2014. **31**: p. 158-173.
21. Osterloh, F.E., *Inorganic materials as catalysts for photochemical splitting of water.* Chemistry of Materials, 2008. **20**(1): p. 35-54.

22. Kudo, A. and Y. Miseki, *Heterogeneous photocatalyst materials for water splitting.* Chemical Society Reviews, 2009. **38**(1): p. 253-278.
23. Chen, X., et al., *Semiconductor-based photocatalytic hydrogen generation.* Chemical reviews, 2010. **110**(11): p. 6503-6570.
24. Kubacka, A., M. Fernandez-Garcia, and G. Colon, *Advanced nanoarchitectures for solar photocatalytic applications.* Chemical reviews, 2012. **112**(3): p. 1555-1614.
25. Hisatomi, T., J. Kubota, and K. Domen, *Recent advances in semiconductors for photocatalytic and photoelectrochemical water splitting.* Chemical Society Reviews, 2014. **43**(22): p. 7520-7535.
26. Yang, J., et al., *Roles of cocatalysts in photocatalysis and photoelectrocatalysis.* Accounts of chemical research, 2013. **46**(8): p. 1900-1909.
27. Liu, G., et al., *Titanium Dioxide Crystals with Tailored Facets.* Chemical Reviews, 2014. **114**(19): p. 9559-9612.
28. Wang, H., et al., *Semiconductor heterojunction photocatalysts: design, construction, and photocatalytic performances.* Chemical Society Reviews, 2014. **43**(15): p. 5234-5244.
29. Maeda, K. and K. Domen, *Development of novel photocatalyst and cocatalyst materials for water splitting under visible light.* Bulletin of the Chemical Society of Japan, 2016. **89**(6): p. 627-648.
30. Bonaccorso, F., et al., *Graphene, related two-dimensional crystals, and hybrid systems for energy conversion and storage.* Science, 2015. **347**(6217): p. 1246501.
31. Song, H., et al., *Solar-driven hydrogen production: Recent advances, challenges, and future perspectives.* ACS Energy Letters, 2022. **7**(3): p. 1043-1065.
32. Linsebigler, A.L., G. Lu, and J.T. Yates Jr, *Photocatalysis on TiO2 surfaces: principles, mechanisms, and selected results.* Chemical reviews, 1995. **95**(3): p. 735-758.
33. Jafari, T., et al., *Photocatalytic water splitting—the untamed dream: a review of recent advances.* Molecules, 2016. **21**(7): p. 900.
34. Wang, J., et al., *Band structure tuning of TiO2 for enhanced photoelectrochemical water splitting.* The Journal of Physical Chemistry C, 2014. **118**(14): p. 7451-7457.
35. Hoffmann, M.R., et al., *Environmental applications of semiconductor photocatalysis.* Chemical reviews, 1995. **95**(1): p. 69-96.
36. Maeda, K., *Z-scheme water splitting using two different semiconductor photocatalysts.* Acs Catalysis, 2013. **3**(7): p. 1486-1503.
37. Wang, X., et al., *A metal-free polymeric photocatalyst for hydrogen production from water under visible light.* Nature materials, 2009. **8**(1): p. 76-80.
38. Chen, S., T. Takata, and K. Domen, *Particulate photocatalysts for overall water splitting.* Nature Reviews Materials, 2017. **2**(10): p. 1-17.
39. Jiang, C., et al., *Photoelectrochemical devices for solar water splitting–materials and challenges.* Chemical Society Reviews, 2017. **46**(15): p. 4645-4660.
40. Wang, S., G. Liu, and L. Wang, *Crystal facet engineering of photoelectrodes for photoelectrochemical water splitting.* Chemical reviews, 2019. **119**(8): p. 5192-5247.
41. Chen, Y., et al., *Metal oxide-based tandem cells for self-biased photoelectrochemical water splitting.* ACS Energy Letters, 2020. **5**(3): p. 844-866.
42. Fujishima, A. and K. Honda, *Electrochemical photolysis of water at a semiconductor electrode.* nature, 1972. **238**(5358): p. 37-38.
43. Fujishima, A., X. Zhang, and D.A. Tryk, *TiO2 photocatalysis and related surface phenomena.* Surface science reports, 2008. **63**(12): p. 515-582.
44. Maeda, K., *Photocatalytic water splitting using semiconductor particles: history and recent developments.* Journal of Photochemistry and Photobiology C: Photochemistry Reviews, 2011. **12**(4): p. 237-268.
45. Sakai, Y., et al., *Photoelectrochemical water splitting by tandem type and heterojunction amorphous silicon electrodes.* Canadian Journal of Chemistry, 1988. **66**(8): p. 1853-1856.

46. Khaselev, O. and J.A. Turner, *A monolithic photovoltaic-photoelectrochemical device for hydrogen production via water splitting.* Science, 1998. **280**(5362): p. 425-427.
47. Licht, S., et al., *Efficient solar water splitting, exemplified by RuO2-catalyzed AlGaAs/Si photoelectrolysis.* The Journal of Physical Chemistry B, 2000. **104**(38): p. 8920-8924.
48. Grimm, A., W.A. de Jong, and G.J. Kramer, *Renewable hydrogen production: A techno-economic comparison of photoelectrochemical cells and photovoltaic-electrolysis.* International Journal of Hydrogen Energy, 2020. **45**(43): p. 22545-22555.
49. Polman, A., et al., *Photovoltaic materials: Present efficiencies and future challenges.* Science, 2016. **352**(6283): p. aad4424.
50. Boretti, A., *Technology readiness level of solar thermochemical splitting cycles.* ACS Energy Letters, 2021. **6**(4): p. 1170-1174.
51. Cheng, W.-H., et al., *Hydrogen from sunlight and water: A side-by-side comparison between photoelectrochemical and solar thermochemical water-splitting.* ACS Energy Letters, 2021. **6**(9): p. 3096-3113.
52. Abanades, S., *Metal oxides applied to thermochemical water-splitting for hydrogen production using concentrated solar energy.* ChemEngineering, 2019. **3**(3): p. 63.
53. Jin, J., et al., *Water-splitting mechanism analysis of Sr/Ca doped LaFeO3 towards commercial efficiency of solar thermochemical H2 production.* International Journal of Hydrogen Energy, 2021. **46**(2): p. 1634-1641.
54. Zhao, Q., J.M.P. Martirez, and E.A. Carter, *Revisiting understanding of electrochemical CO2 reduction on Cu (111): competing proton-coupled electron transfer reaction mechanisms revealed by embedded correlated wavefunction theory.* Journal of the American Chemical Society, 2021. **143**(16): p. 6152-6164.
55. Hori, Y.i., *Electrochemical CO 2 reduction on metal electrodes.* Modern aspects of electrochemistry, 2008: p. 89-189.
56. Kibria, M.G., et al., *Electrochemical CO2 reduction into chemical feedstocks: from mechanistic electrocatalysis models to system design.* Advanced Materials, 2019. **31**(31): p. 1807166.
57. Nitopi, S., et al., *Progress and perspectives of electrochemical CO2 reduction on copper in aqueous electrolyte.* Chemical reviews, 2019. **119**(12): p. 7610-7672.
58. Shi, J., et al., *Enzymatic conversion of carbon dioxide.* Chemical Society Reviews, 2015. **44**(17): p. 5981-6000.
59. Zhu, D.D., J.L. Liu, and S.Z. Qiao, *Recent Advances in Inorganic Heterogeneous Electrocatalysts for Reduction of Carbon Dioxide.* Advanced Materials, 2016. **28**(18): p. 3423-3452.
60. Habisreutinger, S.N., L. Schmidt-Mende, and J.K. Stolarczyk, *Photocatalytic Reduction of CO2 on TiO2 and Other Semiconductors.* Angewandte Chemie International Edition, 2013. **52**(29): p. 7372-7408.
61. Grodkowski, J. and P. Neta, *Copper-catalyzed radiolytic reduction of CO2 to CO in aqueous solutions.* The Journal of Physical Chemistry B, 2001. **105**(21): p. 4967-4972.
62. Wang, W., et al., *Recent advances in catalytic hydrogenation of carbon dioxide.* Chemical Society Reviews, 2011. **40**(7): p. 3703-3727.
63. Klankermayer, J., et al., *Selective Catalytic Synthesis Using the Combination of Carbon Dioxide and Hydrogen: Catalytic Chess at the Interface of Energy and Chemistry.* Angewandte Chemie International Edition, 2016. **55**(26): p. 7296-7343.
64. Zhang, W., et al., *Progress and Perspective of Electrocatalytic CO2 Reduction for Renewable Carbonaceous Fuels and Chemicals.* Advanced Science, 2018. **5**(1): p. 1700275.
65. Han, N., et al., *Promises of main group metal–based nanostructured materials for electrochemical CO2 reduction to formate.* Advanced Energy Materials, 2020. **10**(11): p. 1902338.
66. Kortlever, R., et al., *Catalysts and reaction pathways for the electrochemical reduction of carbon dioxide.* The journal of physical chemistry letters, 2015. **6**(20): p. 4073-4082.

67. Leitner, W., *Carbon dioxide as a raw material: the synthesis of formic acid and its derivatives from CO2.* Angewandte Chemie International Edition in English, 1995. **34**(20): p. 2207-2221.
68. Singh, A.K., S. Singh, and A. Kumar, *Hydrogen energy future with formic acid: a renewable chemical hydrogen storage system.* Catalysis Science & Technology, 2016. **6**(1): p. 12-40.
69. Kortlever, R., et al., *Electrochemical CO2 reduction to formic acid at low overpotential and with high faradaic efficiency on carbon-supported bimetallic Pd–Pt nanoparticles.* Acs Catalysis, 2015. **5**(7): p. 3916-3923.
70. Hori, Y., A. Murata, and R. Takahashi, *Formation of hydrocarbons in the electrochemical reduction of carbon dioxide at a copper electrode in aqueous solution.* Journal of the Chemical Society, Faraday Transactions 1: Physical Chemistry in Condensed Phases, 1989. **85**(8): p. 2309-2326.
71. Choukroun, D., et al., *Bifunctional nickel–nitrogen-doped-carbon-supported copper electrocatalyst for CO2 reduction.* The Journal of Physical Chemistry C, 2020. **124**(2): p. 1369-1381.
72. Jiao, J., et al., *Copper atom-pair catalyst anchored on alloy nanowires for selective and efficient electrochemical reduction of CO2.* Nature chemistry, 2019. **11**(3): p. 222-228.
73. Vilar-Vidal, N., J. Rivas, and M.A. Lopez-Quintela, *Size dependent catalytic activity of reusable subnanometer copper (0) clusters.* ACS Catalysis, 2012. **2**(8): p. 1693-1697.
74. Tyo, E.C. and S. Vajda, *Catalysis by clusters with precise numbers of atoms.* Nature nanotechnology, 2015. **10**(7): p. 577-588.
75. Chen, P.-T., et al., *Size-selective reactivity of subnanometer Ag4 and Ag16 clusters on a TiO2 surface.* The Journal of Physical Chemistry C, 2017. **121**(12): p. 6614-6625.
76. Fernandez, E., M. Boronat, and A. Corma, *Trends in the reactivity of molecular O2 with copper clusters: influence of size and shape.* The Journal of Physical Chemistry C, 2015. **119**(34): p. 19832-19846.
77. Concepción, P., et al., *Enhanced stability of Cu clusters of low atomicity against oxidation. Effect on the catalytic redox process.* ACS Catalysis, 2017. **7**(5): p. 3560-3568.
78. Liu, L. and A. Corma, *Metal catalysts for heterogeneous catalysis: from single atoms to nanoclusters and nanoparticles.* Chemical reviews, 2018. **118**(10): p. 4981-5079.
79. Vilar-Vidal, N., J.R. Rey, and L. Quintela, *Green emitter copper clusters as highly efficient and reusable visible degradation photocatalysts.* Small (Weinheim an der Bergstrasse, Germany), 2014. **10**(18): p. 3632-3636.
80. Attia, Y.A., et al., *Structure-directing and high-efficiency photocatalytic hydrogen production by Ag clusters.* Journal of the American Chemical Society, 2014. **136**(4): p. 1182-1185.
81. Porto, V., et al., *Silver atomic quantum clusters of three atoms for cancer therapy: targeting chromatin compaction to increase the therapeutic index of chemotherapy.* Advanced Materials, 2018. **30**(33): p. 1801317.
82. Zhou, M., et al., *Evolution from the plasmon to exciton state in ligand-protected atomically precise gold nanoparticles.* Nature communications, 2016. **7**(1): p. 13240.
83. González, B.S. and M.A. López-Quintela, *New strategies and synthetic routes to synthesize fluorescent atomic quantum clusters*, in *Functional Nanometer-Sized Clusters of Transition Metals*. 2014. p. 25-50.
84. Copp, S.M., et al., *Fluorescence color by data-driven design of genomic silver clusters.* ACS nano, 2018. **12**(8): p. 8240-8247.
85. Abbas, M.A., P.V. Kamat, and J.H. Bang, *Thiolated gold nanoclusters for light energy conversion.* ACS Energy Letters, 2018. **3**(4): p. 840-854.
86. Passalacqua, R., et al., *Electrochemical behaviour of naked sub-nanometre sized copper clusters and effect of CO 2.* Catalysis Science & Technology, 2016. **6**(18): p. 6977-6985.
87. Halder, A., et al., *Perspective: Size selected clusters for catalysis and electrochemistry.* The Journal of Chemical Physics, 2018. **148**(11).

88. Boronat, M., A. Leyva-Pérez, and A. Corma, *Theoretical and experimental insights into the origin of the catalytic activity of subnanometric gold clusters: attempts to predict reactivity with clusters and nanoparticles of gold.* Accounts of chemical research, 2014. **47**(3): p. 834-844.
89. Kappes, M.M., R.W. Kunz, and E. Schumacher, *Production of large sodium clusters (Nax,. x⩽ 65) by seeded beam expansions.* Chemical Physics Letters, 1982. **91**(6): p. 413-418.
90. Ekardt, W., *Dynamical polarizability of small metal particles: self-consistent spherical jellium background model.* Physical review letters, 1984. **52**(21): p. 1925.
91. Knight, W., et al., *Electronic shell structure and abundances of sodium clusters.* Physical review letters, 1984. **52**(24): p. 2141.
92. Kappes, M.M., et al., *Probes for electronic and geometrical shell structure effects in alkali-metal clusters. Photoionization measurements on KxLi, KxMg and KxZn (x< 25).* Chemical physics letters, 1985. **119**(1): p. 11-16.
93. Bergeron, D.E., et al., *Formation of Al13I-: Evidence for the superhalogen character of Al13.* Science, 2004. **304**(5667): p. 84-87.
94. Dieste, M., et al., *CO2 valorization: A new alternative catalysis with Ag and Cu Metal Molecules.*
95. Alonso, J., *Electronic and atomic structure, and magnetism of transition-metal clusters.* Chemical reviews, 2000. **100**(2): p. 637-678.
96. Popok, V.N., et al., *Cluster–surface interaction: From soft landing to implantation.* Surface Science Reports, 2011. **66**(10): p. 347-377.
97. Huseyinova, S., et al., *Synthesis of highly stable surfactant-free Cu5 clusters in water.* The Journal of Physical Chemistry C, 2016. **120**(29): p. 15902-15908.
98. Hohenberg, P. and W. Kohn, *Inhomogeneous electron gas.* Physical review, 1964. **136**(3B): p. B864.
99. Geerlings, P., F. De Proft, and W. Langenaeker, *Conceptual density functional theory.* Chemical reviews, 2003. **103**(5): p. 1793-1874.
100. Van Mourik, T., M. Bühl, and M.-P. Gaigeot, *Density functional theory across chemistry, physics and biology*. 2014, The Royal Society Publishing. p. 20120488.
101. Orio, M., D.A. Pantazis, and F. Neese, *Density functional theory.* Photosynthesis research, 2009. **102**(2): p. 443-453.
102. Martin, R.M., *Electronic structure: basic theory and practical methods*. 2020: Cambridge university press.
103. Al-Khaykanee, M.K.A., *Quantum theory of electronic and thermal transport through nano-scale and single-molecule devices*. 2018: Lancaster University (United Kingdom).
104. Schrödinger, E., *An undulatory theory of the mechanics of atoms and molecules.* Physical review, 1926. **28**(6): p. 1049.
105. Lee, T.D. and C.N. Yang, *Many-body problem in quantum statistical mechanics. I. General formulation.* Physical Review, 1959. **113**(5): p. 1165.
106. Born, M. and W. Heisenberg, *Zur quantentheorie der molekeln*, in *Original Scientific Papers Wissenschaftliche Originalarbeiten*. 1985, Springer. p. 216-246.
107. Kohn, W. and L.J. Sham, *Self-consistent equations including exchange and correlation effects.* Physical review, 1965. **140**(4A): p. A1133.
108. Parr, R. and W. Yang, *Density-functional theory of atoms and molecules, vol. 16: Oxford university press.* New York, NY.[Google Scholar], 1989.
109. Levy, M., *Electron densities in search of Hamiltonians.* Physical Review A, 1982. **26**(3): p. 1200.
110. Lieb, E.H., *Erratum: Thomas-Fermi and related theories of atoms and molecules.* Reviews of Modern Physics, 1982. **54**(1): p. 311.
111. Hartree, D.R. *The wave mechanics of an atom with a non-Coulomb central field. Part I. Theory and methods*. in *Mathematical Proceedings of the Cambridge Philosophical Society*. 1928. Cambridge university press.

112. Hartree, D.R. and H.C.W.P.P. Fund, *The calculation of atomic structures*. 1957: J. Wiley.
113. Fock, V., *Näherungsmethode zur Lösung des quantenmechanischen Mehrkörperproblems.* Zeitschrift für Physik, 1930. **61**(1): p. 126-148.
114. Kohn, W., A.D. Becke, and R.G. Parr, *Density functional theory of electronic structure.* The Journal of Physical Chemistry, 1996. **100**(31): p. 12974-12980.
115. Zhang, G.-P., et al., *Optimizing the conductance switching performance in photoswitchable dimethyldihydropyrene/cyclophanediene single-molecule junctions.* Physica E: Low-dimensional Systems and Nanostructures, 2019. **109**: p. 1-5.
116. Jones, R.O. and O. Gunnarsson, *The density functional formalism, its applications and prospects.* Reviews of Modern Physics, 1989. **61**(3): p. 689.
117. Perdew, J.P., K. Burke, and M. Ernzerhof, *Generalized gradient approximation made simple.* Physical review letters, 1996. **77**(18): p. 3865.
118. Heyd, J., G.E. Scuseria, and M. Ernzerhof, *Hybrid functionals based on a screened Coulomb potential.* The Journal of chemical physics, 2003. **118**(18): p. 8207-8215.
119. Becke, A.D., *A new mixing of Hartree–Fock and local density-functional theories.* The Journal of chemical physics, 1993. **98**(2): p. 1372-1377.
120. Arbuznikov, A., *Hybrid exchange correlation functionals and potentials: Concept elaboration.* Journal of Structural Chemistry, 2007. **48**: p. S1-S31.
121. Adamo, C. and V. Barone, *Toward reliable density functional methods without adjustable parameters: The PBE0 model.* The Journal of Chemical Physics, 1999. **110**(13): p. 6158-6170.
122. Lafond, F., *Hybrid functionals approach for the study of the properties of complex materials for photovoltaic applications*. 2019, Université de Lorraine.
123. Stephens, P.J., et al., *Ab Initio Calculation of Vibrational Absorption and Circular Dichroism Spectra Using Density Functional Force Fields.* The Journal of Physical Chemistry, 1994. **98**(45): p. 11623-11627.
124. Piela, L., *Chapter 3 - Chasing the Correlation Dragon: Density Functional Theory (DFT)*, in *Ideas of Quantum Chemistry (Third Edition)*, L. Piela, Editor. 2020, Elsevier. p. 191-252.
125. Zhao, Y. and D.G. Truhlar, *A density functional that accounts for medium-range correlation energies in organic chemistry.* Organic Letters, 2006. **8**(25): p. 5753-5755.
126. Tao, J., et al., *Climbing the density functional ladder: Nonempirical meta–generalized gradient approximation designed for molecules and solids.* Physical review letters, 2003. **91**(14): p. 146401.
127. Staroverov, V., et al., *Deviations of calculated properties from experiment for species of the G3/99, T-96R, and T-82F test sets. Properties of hydrogen-bonded complexes.* J Chem Phys, 2003. **119**: p. 12129-12137.
128. Zhang, Y., A. Vela, and D.R. Salahub, *Reparameterization of a meta-generalized gradient approximation functional by combining TPSS exchange with τ1 correlation.* Theoretical Chemistry Accounts, 2007. **118**: p. 693-707.
129. Allouti, F., L. Manceron, and M.E. Alikhani, *On the performance of the hybrid TPSS meta-GGA functional to study the singlet open-shell structures: A combined theoretical and experimental investigations of the Ni2O2 molecule.* Journal of Molecular Structure: THEOCHEM, 2009. **903**(1): p. 4-10.
130. Williamson, B.A., *Understanding the Electronic and Thermodynamic Properties of Wide Band Gap Materials*. 2018, UCL (University College London).
131. Thetford, A., *DFT modelling of methane oxidation with H2O2 over heterogeneous catalysts*. 2012, Cardiff University.
132. Tolba, S.A., et al., *The DFT+ U: Approaches, accuracy, and applications.* 2018. **1**: p. 5772.
133. Dudarev, S.L., et al., *Electron-energy-loss spectra and the structural stability of nickel oxide: An LSDA+ U study.* 1998. **57**(3): p. 1505.
134. Hubbard, J., *Electron correlations in narrow energy bands.* Proceedings of the Royal Society of London. Series A. Mathematical and Physical Sciences, 1963. **276**(1365): p. 238-257.

135. Hubbard, J., *Electron correlations in narrow energy bands. II. The degenerate band case.* Proceedings of the Royal Society of London. Series A. Mathematical and Physical Sciences, 1964. **277**(1369): p. 237-259.
136. Hubbard, J., *Electron correlations in narrow energy bands III. An improved solution.* Proceedings of the Royal Society of London. Series A. Mathematical and Physical Sciences, 1964. **281**(1386): p. 401-419.
137. Hubbard, J., *Electron correlations in narrow energy bands-IV. The atomic representation.* Proceedings of the Royal Society of London. Series A. Mathematical and Physical Sciences, 1965. **285**(1403): p. 542-560.
138. Hubbard, J., *Electron correlations in narrow energy bands V. A perturbation expansion about the atomic limit.* Proceedings of the Royal Society of London. Series A. Mathematical and Physical Sciences, 1967. **296**(1444): p. 82-99.
139. Hubbard, J., *Electron correlations in narrow energy bands VI. The connexion with many-body perturbation theory.* Proceedings of the Royal Society of London. Series A. Mathematical and Physical Sciences, 1967. **296**(1444): p. 100-112.
140. Grimme, S., *Density functional theory with London dispersion corrections.* WIREs Computational Molecular Science, 2011. **1**(2): p. 211-228.
141. Kristyán, S. and P. Pulay, *Can (semi) local density functional theory account for the London dispersion forces?* Chemical physics letters, 1994. **229**(3): p. 175-180.
142. Pérez-Jordá, J. and A.D. Becke, *A density-functional study of van der Waals forces: rare gas diatomics.* Chemical physics letters, 1995. **233**(1-2): p. 134-137.
143. Grimme, S., *Semiempirical GGA-type density functional constructed with a long-range dispersion correction.* Journal of Computational Chemistry, 2006. **27**(15): p. 1787-1799.
144. Goerigk, L., *Chapter 6 - A Comprehensive Overview of the DFT-D3 London-Dispersion Correction*, in *Non-Covalent Interactions in Quantum Chemistry and Physics*, A. Otero de la Roza and G.A. DiLabio, Editors. 2017, Elsevier. p. 195-219.
145. Grimme, S., *Semiempirical GGA-type density functional constructed with a long-range dispersion correction.* Journal of computational chemistry, 2006. **27**(15): p. 1787-1799.
146. Grimme, S., et al., *A consistent and accurate ab initio parametrization of density functional dispersion correction (DFT-D) for the 94 elements H-Pu.* The Journal of chemical physics, 2010. **132**(15).
147. Huang, H., *A density functional theory study into the mechanism and reactivity in heterogeneous system*. 2021, Queen's University Belfast.
148. Grimme, S., S. Ehrlich, and L. Goerigk, *Effect of the damping function in dispersion corrected density functional theory.* Journal of computational chemistry, 2011. **32**(7): p. 1456-1465.
149. Smith, D.G., et al., *Revised damping parameters for the D3 dispersion correction to density functional theory.* The journal of physical chemistry letters, 2016. **7**(12): p. 2197-2203.
150. Engel, E. and R.M. Dreizler, *Foundations of density functional theory: Existence theorems*, in *Density Functional Theory*. 2011, Springer. p. 11-56.
151. Parr, R.G., *Density functional theory.* Annual Review of Physical Chemistry, 1983. **34**(1): p. 631-656.
152. Slater, J.C., *A simplification of the Hartree-Fock method.* Physical review, 1951. **81**(3): p. 385.
153. Togo, A. and I. Tanaka, *$\texttt {Spglib} $: a software library for crystal symmetry search.* arXiv preprint arXiv:1808.01590, 2018.
154. Bernstein, F.C., et al., *The Protein Data Bank: a computer-based archival file for macromolecular structures.* Journal of molecular biology, 1977. **112**(3): p. 535-542.
155. Hall, S.R., F.H. Allen, and I.D. Brown, *The crystallographic information file (CIF): a new standard archive file for crystallography.* Acta Crystallographica Section A: Foundations of Crystallography, 1991. **47**(6): p. 655-685.
156. Kresse, G. and D. Joubert, *From ultrasoft pseudopotentials to the projector augmented-wave method.* Physical review b, 1999. **59**(3): p. 1758.

157. Blöchl, P.E., *Projector augmented-wave method.* Physical review B, 1994. **50**(24): p. 17953.
158. Johnson, D.D., *Modified Broyden's method for accelerating convergence in self-consistent calculations.* Physical Review B, 1988. **38**(18): p. 12807.
159. Kress, G. and J. Furthmüller, *Efficient iterative schemes for ab initio total-energy calculations using a plane-wave basis set.* Phys. Rev. B, 1996. **54**(16): p. 11169-11186.
160. Teter, M.P., M.C. Payne, and D.C. Allan, *Solution of Schrödinger's equation for large systems.* Physical Review B, 1989. **40**(18): p. 12255.
161. Bylander, D., L. Kleinman, and S. Lee, *Self-consistent calculations of the energy bands and bonding properties of B 12 C 3.* Physical Review B, 1990. **42**(2): p. 1394.
162. Monkhorst, H.J. and J.D. Pack, *Special points for Brillouin-zone integrations.* Physical review B, 1976. **13**(12): p. 5188.
163. Yeh, J. and I. Lindau, *Atomic subshell photoionization cross sections and asymmetry parameters: 1⩽Z⩽103.* Atomic data and nuclear data tables, 1985. **32**(1): p. 1-155.
164. Pack, J.D. and H.J. Monkhorst, *" Special points for Brillouin-zone integrations"—a reply.* Physical Review B, 1977. **16**(4): p. 1748.
165. Morgan, B.J. and G.W. Watson, *A DFT+ U description of oxygen vacancies at the TiO2 rutile (1 1 0) surface.* Surface Science, 2007. **601**(21): p. 5034-5041.
166. Morgan, B.J. and G.W. Watson, *A density functional theory+ U study of oxygen vacancy formation at the (110),(100),(101), and (001) surfaces of rutile TiO2.* The Journal of Physical Chemistry C, 2009. **113**(17): p. 7322-7328.
167. Morgan, B.J. and G.W. Watson, *Intrinsic n-type defect formation in TiO2: a comparison of rutile and anatase from GGA+ U calculations.* The Journal of Physical Chemistry C, 2010. **114**(5): p. 2321-2328.
168. Cronemeyer, D.C., *Electrical and optical properties of rutile single crystals.* Physical Review, 1952. **87**(5): p. 876.
169. Schuchardt, K.L., et al., *Basis set exchange: a community database for computational sciences.* Journal of chemical information and modeling, 2007. **47**(3): p. 1045-1052.
170. Lehtola, S., *A review on non-relativistic, fully numerical electronic structure calculations on atoms and diatomic molecules.* International Journal of Quantum Chemistry, 2019. **119**(19): p. e25968.
171. Orlando, R., et al., *Ab initio Hartree-Fock calculations for periodic compounds: application to semiconductors.* Journal of Physics: Condensed Matter, 1990. **2**(38): p. 7769.
172. Soler, J.M., et al., *The SIESTA method for ab initio order-N materials simulation.* Journal of Physics: Condensed Matter, 2002. **14**(11): p. 2745.
173. Foresman, J. and E. Frish, *Exploring chemistry.* Gaussian Inc., Pittsburg, USA, 1996. **21**.
174. Lee, K., J. Yu, and Y. Morikawa, *Comparison of localized basis and plane-wave basis for density-functional calculations of organic molecules on metals.* Physical Review B, 2007. **75**(4): p. 045402.
175. Vanderbilt, D., *Soft self-consistent pseudopotentials in a generalized eigenvalue formalism.* Physical review B, 1990. **41**(11): p. 7892.
176. King-Smith, R. and D. Vanderbilt, *Theory of polarization of crystalline solids.* Physical Review B, 1993. **47**(3): p. 1651.
177. Payne, M.C., et al., *Iterative minimization techniques for ab initio total-energy calculations: molecular dynamics and conjugate gradients.* Reviews of modern physics, 1992. **64**(4): p. 1045.
178. Wimmer, E., et al., *Cesiation of W (001): Work function lowering by multiple dipole formation.* Physical Review Letters, 1982. **48**(16): p. 1128.
179. Kleinman, L. and D. Bylander, *Efficacious form for model pseudopotentials.* Physical Review Letters, 1982. **48**(20): p. 1425.
180. Scofield, J.H., *Theoretical Photoionization Cross Section from 1 to 1500 keV,.* Lawrence Livermore Laboratory, 1973.

181. Holzwarth, N.A.W., et al., *Comparison of the projector augmented-wave, pseudopotential, and linearized augmented-plane-wave formalisms for density-functional calculations of solids.* Physical Review B, 1997. **55**(4): p. 2005-2017.
182. Blöchl, P.E., *Projector augmented-wave method.* Physical Review B, 1994. **50**(24): p. 17953-17979.
183. Bader, R.F., *A quantum theory of molecular structure and its applications.* Chemical Reviews, 1991. **91**(5): p. 893-928.
184. Sanville, E., et al., *Improved grid-based algorithm for Bader charge allocation.* Journal of computational chemistry, 2007. **28**(5): p. 899-908.
185. Tang, W., E. Sanville, and G. Henkelman, *A grid-based Bader analysis algorithm without lattice bias.* Journal of Physics: Condensed Matter, 2009. **21**(8): p. 084204.
186. Chai, W.R. *Bader Charge Analysis*. Available from: https://theory.cm.utexas.edu/henkelman/research/bader/.
187. Zheng, S., et al., *FeP 3 monolayer as a high-efficiency catalyst for hydrogen evolution reaction.* Journal of Materials Chemistry A, 2019. **7**(44): p. 25665-25671.
188. Zoidis, E., et al., *Spectroscopic studies of vibrational relaxation and chemical exchange broadening in hydrogen-bonded systems. III. Equilibrium processes in the pyridine/water system.* Molecular Physics, 1995. **85**(2): p. 373-383.
189. Heyd, G., *Scuseria, and M. Ernzerhof.* J. Chem. Phys, 2003. **118**(18): p. 8207.
190. Körber, C., et al., *Electronic structure of In 2 O 3 and Sn-doped In 2 O 3 by hard x-ray photoemission spectroscopy.* Physical Review B, 2010. **81**(16): p. 165207.
191. Williamson, B.A., et al., *Engineering valence band dispersion for high mobility p-type semiconductors.* Chemistry of Materials, 2017. **29**(6): p. 2402-2413.
192. Bhachu, D.S., et al., *Bismuth oxyhalides: synthesis, structure and photoelectrochemical activity.* Chemical Science, 2016. **7**(8): p. 4832-4841.
193. Sathasivam, S., et al., *Computational and experimental study of Ta2O5 thin films.* The Journal of Physical Chemistry C, 2017. **121**(1): p. 202-210.
194. Sathasivam, S., et al., *Single Step Solution Processed GaAs Thin Films from GaMe3 and T BuAsH2 under Ambient Pressure.* The Journal of Physical Chemistry C, 2016. **120**(13): p. 7013-7019.
195. Liu, L. and C. Liu, *Origin of the overpotentials for HCOO− and CO formation in the electroreduction of CO 2 on Cu (211): the reductive desorption processes decide.* Physical Chemistry Chemical Physics, 2018. **20**(8): p. 5756-5765.
196. Pao, H.-T. and C.-M. Tsai, *CO2 emissions, energy consumption and economic growth in BRIC countries.* Energy policy, 2010. **38**(12): p. 7850-7860.
197. Baykara, S.Z., *Hydrogen: A brief overview on its sources, production and environmental impact.* International Journal of Hydrogen Energy, 2018. **43**(23): p. 10605-10614.
198. Staffell, I., et al., *The role of hydrogen and fuel cells in the global energy system.* Energy & Environmental Science, 2019. **12**(2): p. 463-491.
199. Zhu, B., R. Zou, and Q. Xu, *Metal–organic framework based catalysts for hydrogen evolution.* Advanced Energy Materials, 2018. **8**(24): p. 1801193.
200. Mazheika, A.S., et al., *Theoretical study of adsorption of Ag clusters on the anatase TiO2 (100) surface.* The Journal of Physical Chemistry C, 2011. **115**(35): p. 17368-17377.
201. Hong, S.-P., et al., *Comprehensive study on the morphology control of TiO2 nanorods on foreign substrates by the hydrothermal method.* Crystal Growth & Design, 2018. **18**(11): p. 6504-6512.
202. Neaţu, S.t., et al., *Gold–copper nanoalloys supported on TiO2 as photocatalysts for CO2 reduction by water.* Journal of the American Chemical Society, 2014. **136**(45): p. 15969-15976.
203. Asahi, R., et al., *Visible-light photocatalysis in nitrogen-doped titanium oxides.* science, 2001. **293**(5528): p. 269-271.

204. Zhu, W., et al., *Band gap narrowing of titanium oxide semiconductors by noncompensated anion-cation codoping for enhanced visible-light photoactivity.* Physical review letters, 2009. **103**(22): p. 226401.
205. McManamon, C., et al., *A facile route to synthesis of S-doped TiO2 nanoparticles for photocatalytic activity.* Journal of Molecular Catalysis A: Chemical, 2015. **406**: p. 51-57.
206. Xu, L., et al., *Hybrid density functional study on band structure engineering of ZnS (110) surface by anion–cation codoping for overall water splitting.* New Journal of Chemistry, 2022. **46**(17): p. 8079-8087.
207. Majeed, I., et al., *Titania supported MOF-199 derived Cu–Cu 2 O nanoparticles: highly efficient non-noble metal photocatalysts for hydrogen production from alcohol–water mixtures.* Catalysis Science & Technology, 2017. **7**(3): p. 677-686.
208. Sclafani, A. and J.-M. Herrmann, *Influence of metallic silver and of platinum-silver bimetallic deposits on the photocatalytic activity of titania (anatase and rutile) in organic and aqueous media.* Journal of Photochemistry and Photobiology A: Chemistry, 1998. **113**(2): p. 181-188.
209. Wu, Q., et al., *Tuning the surface states of TiO2 using Cu5 atomic clusters.* Applied Surface Science, 2022. **594**: p. 153455.
210. Buceta, D., et al., *Stability and Reversible Oxidation of Sub-Nanometric Cu5 Metal Clusters: Integrated Experimental Study and Theoretical Modeling.* Chemistry–A European Journal, 2023: p. e202301517.
211. de Lara-Castells, M.P., et al., *Increasing the optical response of TiO 2 and extending it into the visible region through surface activation with highly stable Cu 5 clusters.* Journal of Materials Chemistry A, 2019. **7**(13): p. 7489-7500.
212. López-Caballero, P., A.W. Hauser, and M. Pilar de Lara-Castells, *Exploring the catalytic properties of unsupported and TiO2-supported Cu5 clusters: CO2 Decomposition to CO and CO2 photoactivation.* The Journal of Physical Chemistry C, 2019. **123**(37): p. 23064-23074.
213. Huseyinova, S., et al., *Synthesis of highly stable surfactant-free Cu5 clusters in water.* The Journal of Physical Chemistry C, 2016. **120**(29): p. 15902-15908.
214. M.A. López Quintela, D.B., *Process for producing Atomic Quantum Clusters Derivatives.* EU Patent Application PCT/EP2023/075494, 15/09/2022.

.
215. Lee, J. and E. Chung, *Lithium recovery from a simulated geothermal fluid by a combined selective precipitation and solvent extraction method.* Geothermics, 2022. **102**: p. 102388.
216. Ali, I.M., Y.H. Kotp, and I.M. El-Naggar, *Thermal stability, structural modifications and ion exchange properties of magnesium silicate.* Desalination, 2010. **259**(1-3): p. 228-234.
217. Johnston, J.H., et al., *Nano-structured composite calcium silicate and some novel applications.* Current Applied Physics, 2008. **8**(3-4): p. 504-507.
218. Cao, Z.-f., et al., *Transforming structure of dolomite to enhance its ion-exchange capacity for copper (II).* Colloids and Surfaces A: Physicochemical and Engineering Aspects, 2018. **539**: p. 201-208.
219. Kresse, G. and J. Furthmüller, *Efficiency of ab-initio total energy calculations for metals and semiconductors using a plane-wave basis set.* Computational materials science, 1996. **6**(1): p. 15-50.
220. Kresse, G. and J. Hafner, *Ab initio molecular dynamics for liquid metals.* Physical review B, 1993. **47**(1): p. 558.
221. Kresse, G. and J. Hafner, *Ab initio molecular-dynamics simulation of the liquid-metal–amorphous-semiconductor transition in germanium.* Physical Review B, 1994. **49**(20): p. 14251.
222. Blöchl, P.E., O. Jepsen, and O.K. Andersen, *Improved tetrahedron method for Brillouin-zone integrations.* Physical Review B, 1994. **49**(23): p. 16223.
223. Janotti, A. and C.G. Van de Walle, *LDA+ U and hybrid functional calculations for defects in ZnO, SnO2, and TiO2.* physica status solidi (b), 2011. **248**(4): p. 799-804.

224. Wan, Q., et al., *Single atom detachment from Cu clusters, and diffusion and trapping on CeO 2 (111): Implications in Ostwald ripening and atomic redispersion.* Nanoscale, 2018. **10**(37): p. 17893-17901.
225. Singha, R.K., et al., *Methane activation at the metal–support interface of Ni4–CeO2 (111) catalyst: a theoretical study.* The Journal of Physical Chemistry C, 2019. **123**(15): p. 9788-9798.
226. Janotti, A., et al., *Hybrid functional studies of the oxygen vacancy in TiO 2.* Physical Review B, 2010. **81**(8): p. 085212.
227. Bader, R.F., *Atoms in molecules.* Accounts of Chemical Research, 1985. **18**(1): p. 9-15.
228. Krukau, A.V., et al., *Influence of the exchange screening parameter on the performance of screened hybrid functionals.* The Journal of chemical physics, 2006. **125**(22): p. 224106.
229. Perron, H., et al., *Optimisation of accurate rutile TiO 2 (110),(100),(101) and (001) surface models from periodic DFT calculations.* Theoretical Chemistry Accounts, 2007. **117**: p. 565-574.
230. Momma, K. and F. Izumi, *VESTA 3 for three-dimensional visualization of crystal, volumetric and morphology data.* Journal of applied crystallography, 2011. **44**(6): p. 1272-1276.
231. López-Caballero, P., et al., *Ag5-induced stabilization of multiple surface polarons on perfect and reduced TiO2 rutile (110).* The Journal of Chemical Physics, 2020. **153**(16): p. 164702.
232. De Angelis, F., et al., *Theoretical studies on anatase and less common TiO2 phases: bulk, surfaces, and nanomaterials.* Chemical reviews, 2014. **114**(19): p. 9708-9753.
233. Yu, X., et al., *Effects of oxygen defects on electronic band structures and dopant migration in Sn-doped TiO2 by density functional studies.* Chemical Physics Letters, 2020. **754**: p. 137732.
234. Henderson, M.A., et al., *Insights into photoexcited electron scavenging processes on TiO2 obtained from studies of the reaction of O2 with OH groups adsorbed at electronic defects on TiO2 (110).* The Journal of Physical Chemistry B, 2003. **107**(2): p. 534-545.
235. Mackrodt, W., E.-A. Simson, and N. Harrison, *An ab initio Hartree-Fock study of the electron-excess gap states in oxygen-deficient rutile TiO2.* Surface science, 1997. **384**(1-3): p. 192-200.
236. Ramamoorthy, M., R. King-Smith, and D. Vanderbilt, *Defects on TiO 2 (110) surfaces.* Physical Review B, 1994. **49**(11): p. 7709.
237. Lindan, P., et al., *First-principles spin-polarized calculations on the reduced and reconstructed TiO 2 (110) surface.* Physical Review B, 1997. **55**(23): p. 15919.
238. Olivier, J.G., K. Schure, and J. Peters, *Trends in global CO2 and total greenhouse gas emissions.* PBL Netherlands Environmental Assessment Agency, 2017. **5**: p. 1-11.
239. Chu, S., *Carbon capture and sequestration*. 2009, American Association for the Advancement of Science. p. 1599-1599.
240. D'Alessandro, D.M., B. Smit, and J.R. Long, *Carbon dioxide capture: prospects for new materials.* Angewandte Chemie International Edition, 2010. **49**(35): p. 6058-6082.
241. Cheng, D., et al., *Computational approaches to the chemical conversion of carbon dioxide.* ChemSusChem, 2013. **6**(6): p. 944-965.
242. Haszeldine, R.S., *Carbon capture and storage: how green can black be?* Science, 2009. **325**(5948): p. 1647-1652.
243. Lastoskie, C., *Caging carbon dioxide.* Science, 2010. **330**(6004): p. 595-596.
244. Olah, G.A., *Beyond oil and gas: the methanol economy.* Angewandte Chemie International Edition, 2005. **44**(18): p. 2636-2639.
245. Markewitz, P., et al., *Worldwide innovations in the development of carbon capture technologies and the utilization of CO 2.* Energy & environmental science, 2012. **5**(6): p. 7281-7305.
246. Yang, Z.-Z., et al., *Carbon dioxide utilization with C–N bond formation: carbon dioxide capture and subsequent conversion.* Energy & Environmental Science, 2012. **5**(5): p. 6602-6639.
247. Chang, K.S., et al., *Conversion of carbon dioxide to oxaloacetate using integrated carbonic anhydrase and phosphoenolpyruvate carboxylase.* Bioprocess and biosystems engineering, 2013. **36**: p. 1923-1928.

248. Lee, J., et al., *Electrochemical CO2 reduction using alkaline membrane electrode assembly on various metal electrodes.* Journal of CO2 Utilization, 2019. **31**: p. 244-250.
249. Rosen, J., et al., *Electrodeposited Zn dendrites with enhanced CO selectivity for electrocatalytic CO2 reduction.* Acs Catalysis, 2015. **5**(8): p. 4586-4591.
250. Ma, M., K. Djanashvili, and W.A. Smith, *Controllable hydrocarbon formation from the electrochemical reduction of CO2 over Cu nanowire arrays.* Angewandte chemie international edition, 2016. **55**(23): p. 6680-6684.
251. Lee, S., D. Kim, and J. Lee, *Electrocatalytic production of C3-C4 compounds by conversion of CO2 on a chloride-induced bi-phasic Cu2O-Cu catalyst.* Angewandte Chemie, 2015. **127**(49): p. 14914-14918.
252. Feng, X., et al., *A direct grain-boundary-activity correlation for CO electroreduction on Cu nanoparticles.* ACS central science, 2016. **2**(3): p. 169-174.
253. Ma, S., et al., *Electroreduction of carbon dioxide to hydrocarbons using bimetallic Cu–Pd catalysts with different mixing patterns.* Journal of the American Chemical Society, 2017. **139**(1): p. 47-50.
254. Kim, D., et al., *Electrochemical activation of CO2 through atomic ordering transformations of AuCu nanoparticles.* Journal of the American Chemical Society, 2017. **139**(24): p. 8329-8336.
255. Liu, S., et al., *Shape-dependent electrocatalytic reduction of CO2 to CO on triangular silver nanoplates.* Journal of the American chemical society, 2017. **139**(6): p. 2160-2163.
256. Li, C.W. and M.W. Kanan, *CO2 reduction at low overpotential on Cu electrodes resulting from the reduction of thick Cu2O films.* Journal of the American Chemical Society, 2012. **134**(17): p. 7231-7234.
257. Motokura, K., et al., *Copper-catalyzed formic acid synthesis from CO2 with hydrosilanes and H2O.* Organic letters, 2012. **14**(10): p. 2642-2645.
258. Kattel, S., et al., *Active sites for CO2 hydrogenation to methanol on Cu/ZnO catalysts.* Science, 2017. **355**(6331): p. 1296-1299.
259. Lee, J. and Y. Tak, *Electrocatalytic activity of Cu electrode in electroreduction of CO2.* Electrochimica acta, 2001. **46**(19): p. 3015-3022.
260. Kim, J., D. Summers, and K. Frese Jr, *Reduction of CO2 and CO to methane on Cu foil electrodes.* Journal of electroanalytical chemistry and interfacial electrochemistry, 1988. **245**(1-2): p. 223-244.
261. Hori, Y., et al., *Electrocatalytic process of CO selectivity in electrochemical reduction of CO2 at metal electrodes in aqueous media.* Electrochimica Acta, 1994. **39**(11-12): p. 1833-1839.
262. Hori, Y.i., *Electrochemical CO2 reduction on metal electrodes.* Modern aspects of electrochemistry, 2008: p. 89-189.
263. Benson, E.E., et al., *Electrocatalytic and homogeneous approaches to conversion of CO 2 to liquid fuels.* Chemical Society Reviews, 2009. **38**(1): p. 89-99.
264. Roy, S.C., et al., *Toward solar fuels: photocatalytic conversion of carbon dioxide to hydrocarbons.* ACS nano, 2010. **4**(3): p. 1259-1278.
265. Darensbourg, D.J., *Chemistry of carbon dioxide relevant to its utilization: a personal perspective.* Inorganic chemistry, 2010. **49**(23): p. 10765-10780.
266. Delacourt, C., et al., *Design of an electrochemical cell making syngas (CO+ H2) from CO2 and H2O reduction at room temperature.* Journal of The Electrochemical Society, 2007. **155**(1): p. B42.
267. Peterson, A.A., et al., *How copper catalyzes the electroreduction of carbon dioxide into hydrocarbon fuels.* Energy & Environmental Science, 2010. **3**(9): p. 1311-1315.
268. Kuhl, K.P., et al., *New insights into the electrochemical reduction of carbon dioxide on metallic copper surfaces.* Energy & Environmental Science, 2012. **5**(5): p. 7050-7059.
269. Chen, Z., et al., *Cu (ii)/Cu (0) electrocatalyzed CO 2 and H2O splitting.* Energy & Environmental Science, 2013. **6**(3): p. 813-817.

270. Kuhl, K.P., et al., *Electrocatalytic Conversion of Carbon Dioxide to Methane and Methanol on Transition Metal Surfaces.* Journal of the American Chemical Society, 2014. **136**(40): p. 14107-14113.
271. Kong, X., et al., *Understanding the Effect of *CO Coverage on C–C Coupling toward CO2 Electroreduction.* Nano Letters, 2022. **22**(9): p. 3801-3808.
272. Jia, Y., et al., *Cu-based bimetallic electrocatalysts for CO2 reduction.* Advanced Powder Materials, 2022. **1**(1).
273. Xiao, C. and J. Zhang, *Architectural Design for Enhanced C2 Product Selectivity in Electrochemical CO2 Reduction Using Cu-Based Catalysts: A Review.* ACS Nano, 2021. **15**(5): p. 7975-8000.
274. Verga, L.G., et al., *A DFT Investigation on the Adsorption Site Coordination Effect for CO2 Reduction on Cu Surfaces.*
275. Durand, W.J., et al., *Structure effects on the energetics of the electrochemical reduction of CO2 by copper surfaces.* Surface Science, 2011. **605**(15-16): p. 1354-1359.
276. Nie, X., et al., *Selectivity of CO2 reduction on copper electrodes: the role of the kinetics of elementary steps.* Angewandte Chemie, 2013. **125**(9): p. 2519-2522.
277. Nie, X., et al., *Reaction mechanisms of CO2 electrochemical reduction on Cu (1 1 1) determined with density functional theory.* Journal of catalysis, 2014. **312**: p. 108-122.
278. Ou, L., *Chemical and electrochemical hydrogenation of CO_2 to hydrocarbons on Cu single crystal surfaces: insights into the mechanism and selectivity from DFT calculations.* 2015.
279. Cheng, T., H. Xiao, and W.A. Goddard III, *Reaction mechanisms for the electrochemical reduction of CO2 to CO and formate on the Cu (100) surface at 298 K from quantum mechanics free energy calculations with explicit water.* Journal of the American Chemical Society, 2016. **138**(42): p. 13802-13805.
280. Sheng, T. and S.-G. Sun, *Electrochemical reduction of CO 2 into CO on Cu (100): a new insight into the C–O bond breaking mechanism.* Chemical Communications, 2017. **53**(17): p. 2594-2597.
281. Liu, S.P., et al., *Mechanistic insights into the unique role of copper in CO2 electroreduction reactions.* ChemSusChem, 2017. **10**(2): p. 387-393.
282. Peterson, A.A. and J.K. Nørskov, *Activity descriptors for CO2 electroreduction to methane on transition-metal catalysts.* The Journal of Physical Chemistry Letters, 2012. **3**(2): p. 251-258.
283. Dong, H., Y. Li, and D.-e. Jiang, *First-principles insight into electrocatalytic reduction of CO2 to CH4 on a copper nanoparticle.* The Journal of Physical Chemistry C, 2018. **122**(21): p. 11392-11398.
284. Jo, D.Y., et al., *Role of the Zn atomic arrangements in enhancing the activity and stability of the kinked Cu (2 1 1) site in CH3OH production by CO2 hydrogenation and dissociation: First-principles microkinetic modeling study.* Journal of catalysis, 2019. **373**: p. 336-350.
285. Jo, D.Y., et al., *Interplay of ligand and strain effects in CO adsorption on bimetallic Cu/M (M= Ni, Ir, Pd, and Pt) catalysts from first-principles: effect of different facets on catalysis.* Catalysis Today, 2021. **359**: p. 57-64.
286. Kittel, C., *Introduction to Solid State Physics,(pp. 1–704)*. 2004, Wiley ISBN.
287. LaGraff, J.R. and A.A. Gewirth, *In-situ observation of oxygen adlayer formation on Cu (110) electrode surfaces.* Surface science, 1995. **326**(3): p. L461-L466.
288. Hashiba, H., et al., *A broad parameter range for selective methane production with bicarbonate solution in electrochemical CO 2 reduction.* Sustainable Energy & Fuels, 2017. **1**(8): p. 1734-1739.
289. Vasileff, A., et al., *Surface and interface engineering in copper-based bimetallic materials for selective CO2 electroreduction.* Chem, 2018. **4**(8): p. 1809-1831.
290. Zheng, Y., et al., *Understanding the roadmap for electrochemical reduction of CO2 to multi-carbon oxygenates and hydrocarbons on copper-based catalysts.* Journal of the American Chemical Society, 2019. **141**(19): p. 7646-7659.

291. Hori, Y., et al., *Adsorption of CO accompanied with simultaneous charge transfer on copper single crystal electrodes related with electrochemical reduction of CO2 to hydrocarbons.* Surface science, 1995. **335**: p. 258-263.
292. Takahashi, I., et al., *Electrochemical reduction of CO2 at copper single crystal Cu (S)-[n (111)×(111)] and Cu (S)-[n (110)×(100)] electrodes.* Journal of Electroanalytical Chemistry, 2002. **533**(1-2): p. 135-143.
293. Hori, Y., et al., *Electrochemical reduction of carbon dioxide at various series of copper single crystal electrodes.* Journal of Molecular Catalysis A: Chemical, 2003. **199**(1-2): p. 39-47.
294. Nie, X., et al., *Selectivity of CO2 Reduction on Copper Electrodes: The Role of the Kinetics of Elementary Steps.* Angewandte Chemie International Edition, 2013. **52**(9): p. 2459-2462.
295. Zhang, H., et al., *Crystal facet-dependent electrocatalytic performance of metallic Cu in CO2 reduction reactions.* Chinese Chemical Letters, 2022. **33**(8): p. 3641-3649.
296. Lim, D.-H., et al., *Carbon dioxide conversion into hydrocarbon fuels on defective graphene-supported Cu nanoparticles from first principles.* Nanoscale, 2014. **6**(10): p. 5087-5092.
297. Shin, D.Y., et al., *Understanding mechanisms of carbon dioxide conversion into methane for designing enhanced catalysts from first-principles.* Computational and Theoretical Chemistry, 2016. **1083**: p. 31-37.
298. Shin, D.Y., et al., *First-principles study of copper nanoclusters for enhanced electrochemical CO2 reduction to CH4.* Computational and Theoretical Chemistry, 2017. **1120**: p. 84-90.
299. Nie, X., et al., *Reaction mechanisms of CO2 electrochemical reduction on Cu(111) determined with density functional theory.* Journal of Catalysis, 2014. **312**: p. 108-122.
300. Pérez Paz, A. and A. Rubio, *Hydrated Alkali Atoms on Copper (111): A Density Functional Theory Study.* The Journal of Physical Chemistry C, 2021. **125**(7): p. 3868-3879.
301. Gao, S.-T., et al., *Theoretical understanding of the electrochemical reaction barrier: a kinetic study of CO 2 reduction reaction on copper electrodes.* Physical Chemistry Chemical Physics, 2020. **22**(17): p. 9607-9615.
302. Wang, V., et al., *VASPKIT: A user-friendly interface facilitating high-throughput computing and analysis using VASP code.* Computer Physics Communications, 2021. **267**: p. 108033.
303. Holtzberg, F.v., B. Post, and I. Fankuchen, *The crystal structure of formic acid.* Acta Crystallographica, 1953. **6**(2): p. 127-130.
304. Glockler, G., *Carbon–Oxygen bond energies and bond distances.* The Journal of Physical Chemistry, 1958. **62**(9): p. 1049-1054.
305. Dietz, L., S. Piccinin, and M. Maestri, *Mechanistic Insights into CO2 activation via reverse water–gas shift on metal surfaces.* The Journal of Physical Chemistry C, 2015. **119**(9): p. 4959-4966.
306. Muttaqien, F., et al., *Dissociative adsorption of CO2 on flat, stepped, and kinked Cu surfaces.* The Journal of Chemical Physics, 2014. **141**(3).
307. Muttaqien, F., et al., *CO2 adsorption on the copper surfaces: van der Waals density functional and TPD studies.* The Journal of Chemical Physics, 2017. **147**(9).
308. Gokhale, A.A., J.A. Dumesic, and M. Mavrikakis, *On the mechanism of low-temperature water gas shift reaction on copper.* Journal of the American Chemical Society, 2008. **130**(4): p. 1402-1414.
309. Padama, A.A.B., et al., *Interaction of CO, O, and CO2 with Cu cluster supported on Cu (1 1 1): a density functional theory study.* Journal of Physics: Condensed Matter, 2019. **31**(41): p. 415201.
310. Freund, H.-J. and M.W. Roberts, *Surface chemistry of carbon dioxide.* Surface Science Reports, 1996. **25**(8): p. 225-273.
311. Neatu, S., et al., *Gold–copper nanoalloys supported on TiO2 as photocatalysts for CO2 reduction by water.* Journal of the American Chemical Society, 2014. **136**(45): p. 15969-15976.

312. Feaster, J.T., et al., *Understanding selectivity for the electrochemical reduction of carbon dioxide to formic acid and carbon monoxide on metal electrodes.* Acs Catalysis, 2017. **7**(7): p. 4822-4827.
313. Ye, K., et al., *Synergy effects on Sn-Cu alloy catalyst for efficient CO2 electroreduction to formate with high mass activity.* Science Bulletin, 2020. **65**(9): p. 711-719.
314. Mosali, V.S.S., et al., *Electrocatalytic CO2 reduction to formate on Cu based surface alloys with enhanced selectivity.* ACS Sustainable Chemistry & Engineering, 2019. **7**(24): p. 19453-19462.
315. Velasco-Vélez, J.-J., et al., *The role of the copper oxidation state in the electrocatalytic reduction of CO2 into valuable hydrocarbons.* ACS Sustainable Chemistry & Engineering, 2018. **7**(1): p. 1485-1492.